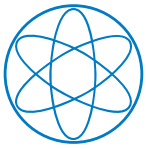

Interacting Photons in a Strongly Coupled Atom-Cavity System

Christoph Hamsen

Dissertation

Max-Planck-Institut für Quantenoptik, Garching
and Physik Department, Technische Universität München

January 4, 2018

Max-Planck-Institut für Quantenoptik

Technische Universität München

Interacting Photons in a Strongly Coupled Atom-Cavity System

Christoph Hamsen

Vollständiger Abdruck der von der Fakultät für Physik der Technischen Universität München zur Erlangung des akademischen Grades eines

Doktors der Naturwissenschaften (Dr. rer. nat.)

genehmigten Dissertation.

Vorsitzender :		Prof. Dr. Frank Pollmann
Prüfer der Dissertation :	1.	Hon.-Prof. Dr. Gerhard Rempe
	2.	Prof. Jonathan J. Finley, Ph. D.
	3.	Prof. Dr. Tracy Northup (nur schriftliche Beurteilung)

Die Dissertation wurde am 24. 07. 2017 bei der Technischen Universität München eingereicht und durch die Fakultät für Physik am 27. 11. 2017 angenommen.

Abstract

Photons do not interact in vacuum, as they carry neither mass nor charge. However, controlled interactions can be mediated by optically nonlinear media. A paradigm studied in the course of this thesis is a single atom trapped at the center of a high-finesse optical cavity. In the first part, it is shown that photons of one light field experience strong interactions when resonantly driving an atomic transition that couples strongly to a single cavity mode. The coupled system exhibits an anharmonic energy level structure that is employed to excite a two-photon resonance and demonstrate a two-photon blockade whereby the absorption of two photons blocks further excitation. In the second part, such strong interactions are realized between individual photons of two different light fields which drive separate cavity modes each strongly coupled to a different transition of the atom. An additional control laser induces a tunable coupling between these modes which manifests in an energy level structure that is anharmonic in both photon numbers. This coupling is demonstrated in two regimes by either mutual blocking or conjunct transit of photons in different modes, while photons in the same mode do not interact.

Zusammenfassung

Photonen wechselwirken nicht im Vakuum, da sie weder Masse noch Ladung besitzen. Kontrollierte Wechselwirkungen können jedoch durch optisch nichtlineare Medien realisiert werden. Ein Beispiel eines solchen Mediums ist ein einzelnes Atom, das im Zentrum eines optischen Resonators hoher Güte gehalten wird, wie es im Rahmen dieser Arbeit untersucht wurde. Im ersten Teil wird gezeigt, dass starke Wechselwirkungen zwischen Photonen eines Lichtfeldes auftreten, wenn dieses resonant einen atomaren Übergang treibt, welcher stark an eine einzelne Resonatormode koppelt. Das gekoppelte System besitzt eine anharmonische Energieniveaustruktur, die verwendet wird, um einen Zwei-Photonen-Übergang anzuregen und so eine Zwei-Photon-Blockade zu realisieren, wobei die Absorption von zwei Photonen weitere Anregungen blockiert. Im zweiten Teil werden solche starken Wechselwirkungen zwischen einzelnen Photonen verschiedener Lichtfelder realisiert, die zwei separate Resonatormoden anregen, welche jeweils stark an unterschiedliche Übergänge eines Atoms koppeln. Ein weiterer Kontrolllaser induziert eine durchstimmbare Kopplung zwischen diesen Moden, was sich in einer Energieniveaustruktur manifestiert, die in beiden Photonenzahlen anharmonisch ist. Diese Kopplung wird in zwei Regimen durch entweder wechselseitiges Blockieren oder gemeinsames Passieren von Photonen unterschiedlicher Moden nachgewiesen, während Photon derselben Mode nicht wechselwirken.

Contents

1. Introduction

The central ideas of quantum mechanics were formulated in the early days of the 20th century. It was Max Planck who first abandoned the concept of energy as a continuous quantity in 1900 and required instead that it manifests in multiples of a smallest quantum in order to deduce a complete description of the black-body spectrum [Pla00]. In 1905, Albert Einstein applied this new concept of quantization to electromagnetic radiation to explain the photoelectric effect [Ein05] which constitutes the discovery of an elementary quantum of light, the photon. Employing the nascent quantum theory, Niels Bohr was able to understand the stable orbits of electrons around the nucleus in Rutherford's atom model which represents the birth of today's concept of atomic orbitals [Boh13]. These initial steps have lead to the development of a relativistic quantum field theory that unifies quantum mechanics, electromagnetism and special relativity and gives full account of light-matter interaction. It is referred to as quantum electrodynamics (QED) [Fey85]. Central momentum for QED's fast evolution derives from its controversial nature being the most precisely tested theory while conflicting with our everyday experience.

Quantization on the microscopic level was initially introduced to explain effects of macroscopic ensembles with averaged outcomes devoid of a classical description such as black-body radiation or the photoelectric effect. The microscopic consequences, on the other hand, were considered counterintuitive and even "ridiculous" [Sch52]. As it was assumed that "we *never* experiment with just *one* electron or atom", thought experiments such as Schrödinger's cat that is dead and alive at the same time [Sch35a] were devised to demonstrate the impossibility of such a theory that defies determinism or local realism. Albert Einstein, Boris Podolsky and Nathan Rosen proposed the EPR paradox that displayed a "spooky action at a distance" whereby correlations between two distant particles seemingly violate the theory of relativity [Ein35]. This correlation was later termed entanglement and recognized not as "*one* but rather *the* characteristic trait of quantum mechanics, the one that enforces its entire departure from classical lines of thought" [Sch35b]. Today, it is entanglement that yields the advantage of prospective quantum devices over classical systems in metrology, communication, information processing and simulation. Both, curiosity for quantum physics and potential quantum improvements for some of today's biggest challenges, drive modern research in quantum optics and are central incentives for the work described in the following.

Despite the early skepticism, systems aspiring to experiment with individual

quanta developed in the second half of the 20th century. The advent of the laser in the 1960s [Mai60] and consecutive progress in trapping and cooling of atoms [Phi98] lead to the prospering field of quantum optics where isolated atoms interacting with electromagnetic radiation became a testbed for quantum theory. An example is the quantum Zeno effect that was theoretically predicted to inhibit the system's evolution to a final state by continuous observation [Mis77]. It was demonstrated experimentally with ions in a Penning trap that were treated with short light pulses while driving ground state transitions with a radio frequency field [Ita90]. The first measurements of the emission from single atoms that defies classical description were performed with dilute atomic beams [Car76, Kim77]. Soon after in 1980, an ion in a dynamic electric trap was the first system to realize trapping of a single particle in free space for continuous observation [Neu80] which finally opened the route to testing microscopic predictions of QED like quantum jumps [Ber86, Sau86].

However, the interaction of single photons with these single emitters in free space remains in the perturbative regime as the coupling to each single optical mode of the vast environment is negligible. To observe the reversible dynamics of the fundamental interaction between single quanta of light and matter [Rem87], as described by the Jaynes-Cummings model [Jay63], requires engineering of the environment of the atom. Two mirrors that form a cavity may enhance the vacuum fluctuations of a single optical mode such that the coupling to an atom exceeds their interaction with all other modes which we refer to as strong coupling regime. Thus, birth and death of a microwave photon in a cavity could be recorded by transiting atoms in 2007 [Gle07], an experiment considered as "ridiculous" 70 years ago. While in parallel systems with artificial atoms like quantum dots in semiconductor microcavities [Rei04] and superconducting qubits in transmission line resonators [Wal04] were developed, advances in experiments with optical photons and neutral atoms required trapping [Hoo00, Pin00], cooling [Mau05, Nuß05b, Kub09], and positioning [Nuß05a, Rei13, Neu16] of the atom to a well-defined location within an optical cavity of high finesse and small mode volume. The resulting increase in observation time and larger coupling have enabled repeated interaction with the system required for quantum information processing [Rit12, Rei14] and more precise spectroscopy of its unique energy structure [Boc04, Mau05] to resolve features like the $\sqrt{n}$-nonlinearity [Sch08b] or an atomic antiresonance [Sam14]. Therefore, to advance the work on mechanical control over the atom, we realized 3D atom microscopy of a stationary atom by resolving its position in all three dimensions. Feeding this information back to adjust the position, we achieve a record 97 % of the theoretical maximum coupling strength of our apparatus.

After the advances in harnessing external and internal degrees of freedom (DOF), cavity quantum electrodynamics (CQED) in the regime of strong light-matter coupling provides an ideal system for studying quantum phenomena

and, today, two major research fields unfold on this platform: quantum nonlinear optics and linear quantum networking. Quantum nonlinear CQED deals with two or more photons in the same mode [Cha14], while in linear quantum networking the system interacts sequentially with individual photons in separate temporal modes [Rei15].

Motivation for quantum nonlinear CQED has always been curiosity for the fundamental principles of QED and the prospect of building quantum information devices like quantum light sources. The central ingredient is the anharmonic ladder of energy eigenstates characteristic to the Jaynes-Cummings system and a direct consequence of quantization of both, atom and light field [Rem91, Car96, Tho98, Car08]. It consists of a set of doublets for each excitation number n. Since the splitting of this doublet scales with $\sqrt{n}$, this yields a strong nonlinearity on the level of individual photons [Sch08b, Fin08]. When driving the cavity at the frequency of the first manifold, all higher states are tuned out of resonance by the nonlinear splitting and consequently the absorption of one photon blocks further excitation. Photons are then emitted one by one from the system. In a seminal paper, Birnbaum et al. [Bir05a] were able to demonstrate that no two photons are detected at the same time in the emission of the cavity which truncates the Hilbert space at $n = 1$. This so-called single-photon blockade holds great promise for single-photon sources, a central ingredient to quantum technology [Cha14].

Going beyond a single excitation, has lead to the realization of photon-induced tunneling [Far08], two-photon gateway [Kub08] and squeezing [Our11]. However, truncation at $n = 2$ and thus a two-photon blockade with prospects for two-photon sources was only achieved throughout the course of this thesis [Ham17]. We introduce the general theory and observables of n-photon blockade. We show how bosonic bunching, which hindered previous realizations by favoring excitation to higher manifolds, can be avoided by exciting the atom instead of the cavity. Such atom driving better resolves the inherent nonlinearity, as we demonstrate by an improved single-photon blockade. Finally, by application of this technique, we demonstrate a two-photon blockade for the first time. This approach enables realization of higher n-photon blockades and opens the route towards quantum nonlinear optics with $n > 1$ photons.

In the second research direction of linear quantum networking, the cavity is mostly used as an efficient interface for photons. These serve as carriers of information, so-called flying quantum bits (qubits), as they hardly interact with the environment carrying neither mass nor charge [Kim08]. As such, each qubit occupies its own spatio-temporal mode. The atom in the cavity is required to store, interrogate or process these qubits [Rit12]. For example, interaction with a photon leaves a trace in the atom that is read out in a second step [Nog99, Dua04] which enables non-destructive detection of the photon [Gue07, Rei13, Tie14a], or an atom-photon gate [Rau99, Rei14]. A photon-photon gate is realized by consecutive interaction of two photons with

the atom-cavity system [Hac16]. Compared to nonlinear CQED, quantum networking mostly relies on linear interactions between photons in separate modes.

We go beyond both approaches and engineer a system that mediates nonlinear interaction between photons of two distinct modes which opens the route towards quantum nonlinear all-optical sensing. In that case, photons of one field directly influence, modify or measure photons in the other field while the system merely catalyzes the interaction, but remains inactive in the actual sensing process. Such all-optical quantum nonlinear sensing holds potential for non-destructive counting of photons with photons [Imo85] or heralded n-photon sources [Muñ14].

The physical system comprises a four-level atom with two transitions strongly coupled to two cavity modes. The coupling between these modes is induced by a control beam that causes electromagnetically induced transparency (EIT). We demonstrate that the resulting energy level structure consists of a landscape of quadruplets whose splitting depends nonlinearly on the number of photons in both modes. The system, thus, catalyzes direct nonlinear interactions between photons of two fields driving the cavity modes. We show that this enables either a photon-photon switch in a regime of mutual blocking or conjunct transit of photons in different fields when working on resonance to the new eigenstates of the system. While studied extensively in theory [Wer99, Reb99, Ber06, Le 16], realization of this so-called N-type system constitutes a breakthrough in CQED and holds great potential for future investigation of all-optical quantum nonlinear sensing.

The thesis is organized as follows: In **Chapter 2**, we introduce the theory of strong light-matter coupling including dissipation to the environment. Furthermore, we describe the experimental apparatus, 3D positioning of atoms, and experimental techniques to investigate and manipulate their energy level structure and eigenstate. The work on two-photon blockade that extents truncation of the Hilbert space to $n > 1$ photons is discussed in **Chapter 3**. Major topics are the theoretical definition and experimental detection of n-photon blockade, transition strengths between eigenstates in dependence of the driving scheme and the experimental realization of single- and two-photon blockade. We cover the work on strong coupling between photons of two light fields in an N-type CQED system in **Chapter 4**. We discuss the novel theory and energy level structure, address quantum simulation of the system, outline techniques used to overcome the challenge of resonant strong coupling between two atomic transitions and two cavity modes and finally demonstrate the first features of this novel system reflecting the interactions between photons of two different fields in spectroscopy and cross-correlation measurements. We conclude the manuscript with a brief summary of the main results and an outlook on future perspectives in **Chapter 5**.

2. Theory, Techniques & Tools for Atoms in Cavities

This chapter gives a general introduction to the theory of atom-light interaction, the apparatus, atom trapping, and spectroscopic characterization of the system. For brevity and clarity, we skip all parameters and formulas that are irrelevant for the physical understanding. A collection of all useful numbers and equations is given in Appendix A. A full technical description and characterization of the apparatus can be found in the primal work of Markus Koch [Koc11a].

As the theory (Section 2.1) has been described numerous times before in textbooks and theses, I will present my own short tale of cavity QED and remain descriptive rather than mathematically rigorous in deriving or scarce in summarizing. Thus, we will touch on some topics and physical concepts that influenced and motivated me for this field of research.

3D atom microscopy (Section 2.2) has been a central effort for many years and remained a vital topic throughout my whole PhD project. On the one hand, it refers to the localization of single atoms in all spatial dimensions that we use to prepare one atom at a well-defined position in space which serves as a workhorse for all later experiments and shows a formidable level of control achieved in recent years. On the other hand, well-localized atoms are used as a precise spatial sensor to probe their electromagnetic environment.

After demonstrating full control over the external DOF, we turn to the internal ones via atom spectroscopy (Section 2.3). This is a second ingredient to a solid foundation of quantum optical experiments. Most relevant is the detection of the state of the atom, as well as the characterization of changes to the atomic energy level structure when exposed to external fields. In the end, knowledge and control of these internal DOF establishes the backbone for experiments of much greater complexity.

2.1. Theory of Light-Matter Interaction

In this section, we introduce the fundamental idea of a two-level system (TLS) interacting with a single optical mode. Its theoretical description is based on the Hamiltonian $\hat{\mathcal{H}}$ which yields to the total energy of the system from which any observable quantity is derived. The temporal evolution of the quantum

system is described by the Schrödinger equation where $\psi(t)$ is a wave function that reflects the state of the system [Sch26]:

$$i\hbar\partial_t |\psi(t)\rangle = \hat{\mathcal{H}} |\psi(t)\rangle \tag{2.1}$$

The specific Hamiltonian for a TLS coupled to an optical mode takes the form:

$$\hat{\mathcal{H}} = \hat{\mathcal{H}}_f + \hat{\mathcal{H}}_a + \hat{\mathcal{H}}_i \tag{2.2}$$

Its first two terms correspond to the eigenenergies of the optical field $\hat{\mathcal{H}}_f$ and two-level system $\hat{\mathcal{H}}_a$. The third term $\hat{\mathcal{H}}_i$ yields the energy stored in the interaction between the two.

This Hamiltonian will describe the dipole interaction between the polarization of the TLS and the electric field of the optical mode. It constitutes the central ingredient to the physical effects described within this thesis. Furthermore, it serves as the fundamental building block of various, more complex physical systems that exhibit a wealth of novel physics. Two very different realizations will be encountered in Chapters 3 and 4.

Due to the central role of this Hamiltonian, we will take the time to deduce its general form. In Section 2.1.1, we derive a description of the optical field in second quantization that can be identified with the quantum mechanical harmonic oscillator and express the TLS in terms of the spin-$\frac{1}{2}$ raising and lowering operators. We construct the interaction Hamiltonian and end by bringing the now complete Hamiltonian of the full system into a practically useful form via the rotating wave approximation. To describe realistic systems, we introduce the master equation approach in Section 2.1.2 that allows modeling of mixed states and coupling to the environment. The latter is not only an imperfection but also a prerequisite for the observation of quantum systems in the laboratory or serves as inputs and outputs for aspired quantum information devices. In Section 2.1.3, we show how this yields quantitative results for experimental observables at the example of a two-level atom strongly coupled to a single mode of an optical cavity which lays the groundwork for the following sections and Chapter 3. The concepts discussed here are described in greater detail in several textbooks on CQED, e.g. [Har06].

2.1.1. Hamiltonian

In the classical description, light is an electromagnetic wave that arises as a solution of a special set of linear partial differential equations known as Maxwell's equations who formulated them already in 1865 [Max65]. In vacuum, i.e. without currents or charges, these are given by:

$$\begin{aligned} &\textbf{I.} \quad \nabla \cdot \mathbf{E} = 0 && \textbf{III.} \quad \nabla \times \mathbf{E} = -\partial_t \mathbf{B} \\ &\textbf{II.} \quad \nabla \cdot \mathbf{B} = 0 && \textbf{IV.} \quad \nabla \times \mathbf{B} = c^{-2}\partial_t \mathbf{E} \end{aligned} \tag{2.3}$$

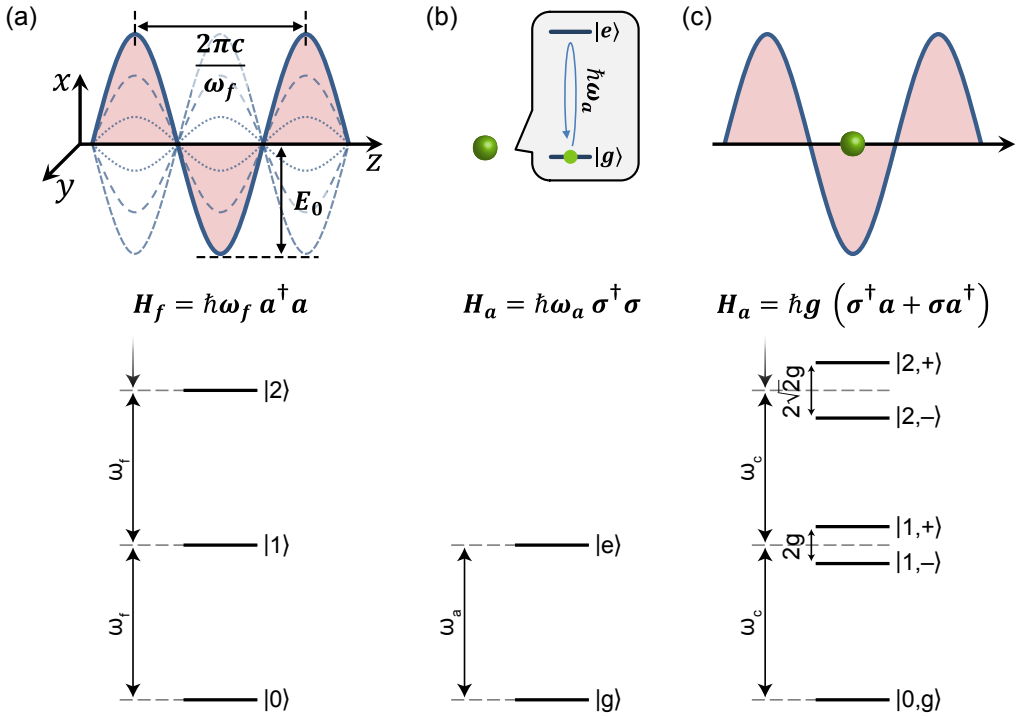

Figure 2.1.: Atom-field coupling. (a) An electromagnetic field exhibits a harmonic energy ladder where the steps count its number of excitations. Its wavevector lies along z, while its electric field is polarized in x. Dashed lines illustrate its oscillation in time. (b) An atom is described as a two-level system with ground and excited states $|g\rangle$ and $|e\rangle$. (c) The atom is coupled to the field being localized to an antinode which results in the anharmonic Jaynes-Cummings ladder.

Here, $\mathbf{E}$ and $\mathbf{B}$ are the electric and magnetic field and $c = (\mu_0\epsilon_0)^{-1/2}$ is the speed of light, with μ_0 (ϵ_0) being the free-space permeability (permittivity). Any particular solution to these differential equations strongly depends on the specific boundary conditions. For the quantization, we will consider a light mode confined to a finite volume V by two perfectly conducting parallel plates with distance L along the z-direction. A solution is the standing wave for the electric field parallel to the x-axis depicted in Figure 2.1 and described by:

$$E_x(z,t) = \sqrt{\frac{2\omega_f^2}{V\epsilon_0}} \cdot q(t) \sin(k_f \cdot z) \tag{2.4}$$

Here, $q = q(t)$ and $\dot{q} = \dot{q}(t)$ describe the temporal modulation of the amplitudes. The wavelength λ_f is defined by the boundary conditions whereby the electric field must vanish on the conducting plate surfaces: $l \cdot \frac{\lambda_f}{2} = L$ and $l \in \mathbb{N}$ is the number of antinodes between the plates. From this the (angular)

frequency ν_f (ω_f) and wavevector k_f follow as:

$$\omega_f = 2\pi\nu_f = ck_f = \frac{2\pi c}{\lambda_f} = l \cdot \frac{c\pi}{L} \tag{2.5}$$

Each l refers to a specific longitudinal mode of the field.

From Equation (2.4), we can directly find the corresponding magnetic field that is oriented along y via the fourth of Maxwell's equations:

$$B_y(z,t) = \left(\frac{\mu_0\epsilon_0}{k_f}\right)\sqrt{\frac{2\omega_f^2}{V\epsilon_0}} \cdot \dot{q}(t)\cos(k_f \cdot z) \tag{2.6}$$

If we define $p := \dot{q}$ and consider that the total energy is given by the sum of the electric and magnetic energy within the volume, we find:

$$\mathcal{H}_f = \frac{1}{2}\int dV \left(\epsilon_0 E_x^2(z,t) + \mu_0^{-1} B_y^2(z,t)\right) = \frac{1}{2}\left(p^2 + \omega_f^2 q^2\right) \tag{2.7}$$

The latter part is formally identical to the energy relation of the classical harmonic oscillator where q and p are known as position and momentum. In order to find a quantum description of light, we apply canonical quantization whereby the classical quantities q and p become the quantum mechanical operators $\hat{q}$ and $\hat{p}$ which fulfill the commutation relation for canonical conjugate variables that directly imply the Heisenberg uncertainty principle [Hei27]:

$$[\hat{q}, \hat{p}] = i\hbar \tag{2.8}$$

In reverse, this also transforms the Hamiltonian, electric and magnetic field into operators $\hat{\mathcal{H}}_f$, $\hat{E}_x$, and $\hat{B}_y$, respectively. These operators now act on the quantum states $|\psi\rangle$ that reflect the state of the quantum system within its Hilbert space that is spanned by all potential eigenstates.

A formal solution to $\hat{\mathcal{H}}_f$ is found by introducing the bosonic creation and annihilation operators, the name of which will become clear later:

$$\hat{a}^\dagger = \frac{1}{\sqrt{2\hbar\omega_f}}\left(\omega_f\hat{q} - i\hat{p}\right) \tag{2.9a}$$

$$\hat{a} = \frac{1}{\sqrt{2\hbar\omega_f}}\left(\omega_f\hat{q} + i\hat{p}\right) \tag{2.9b}$$

These operators fulfill the commutation relation $\left[\hat{a}, \hat{a}^\dagger\right] = 1$ and build the photon number operator $\hat{n} = \hat{a}^\dagger\hat{a}$. The fields now take the form:

$$\hat{E}_x(z,t) = E_0\left(\hat{a} + \hat{a}^\dagger\right)\sin(k_f \cdot z) \quad , E_0 = \sqrt{\frac{\hbar\omega_f}{V\epsilon_0}} \tag{2.10a}$$

$$\hat{B}_y(z,t) = -iB_0\left(\hat{a} - \hat{a}^\dagger\right)\cos(k_f \cdot z) \quad , B_0 = \sqrt{\frac{\hbar\omega_f c^3\mu_0}{V}} \tag{2.10b}$$

Here, $\hat{a}$ and $\hat{a}^\dagger$ play the role of field amplitudes. In fact, if we consider the field classical and replace $\hat{a}$ and $\hat{a}^\dagger$ by the complex amplitude α and its complex conjugate α^*, we recover the classical amplitudes where $\hat{E}_x = E_0 \mathrm{Re}(\alpha) \sin(k_f \cdot z)$ and $\hat{B}_y = B_0 \mathrm{Im}(\alpha) \cos(k_f \cdot z)$ are proportional to the real and imaginary part of α, respectively.

Substituting $\hat{E}_x$ and $\hat{B}_y$, we find the field Hamiltonian to be:

$$\hat{\mathcal{H}}_f = \left(\hat{a}^\dagger \hat{a} + \frac{1}{2}\right) \hbar\omega_f \tag{2.11}$$

Its energy eigenstates $|n\rangle$ fulfill the eigenvalue equation:

$$\hat{\mathcal{H}}_f |n\rangle = \mathcal{E}_n |n\rangle \tag{2.12}$$

This together with previous relations is sufficient to show the following properties of the introduced operators:

$$\hat{a} |n\rangle = \sqrt{n} |n-1\rangle \tag{2.13a}$$
$$\hat{a}^\dagger |n\rangle = \sqrt{n+1} |n+1\rangle \tag{2.13b}$$
$$\hat{n} |n\rangle = n |n\rangle \tag{2.13c}$$
$$\hat{\mathcal{H}}_f |n\rangle = \left(n + \tfrac{1}{2}\right) \hbar\omega_f |n\rangle \tag{2.13d}$$

Consequently, the eigenenergies of the field $\mathcal{E}_n = (n+\frac{1}{2})\hbar\omega_f$ form the expected equidistant energy ladder of the quantum harmonic oscillator (Figure 2.1(a)). In other words, energy appears in quanta of $\hbar\omega_f$ which we refer to as photons. As a result, $n = 0, 1, 2, ...$ corresponds to the photon number, and we call the corresponding eigenstates $|n\rangle$ the photon number states. The operator $\hat{a} = \sqrt{n} |n-1\rangle \langle n|$ ($\hat{a}^\dagger = \sqrt{n+1} |n+1\rangle \langle n|$) then annihilates (creates) a photon in the mode l of the field[1].

The TLS, as depicted in Figure 2.1(b), consists of ground state $|g\rangle$ and excited state $|e\rangle$ split by energy $\hbar\omega_a$. It is formally equivalent to a spin-$\frac{1}{2}$ system with a magnetic field, i.e. the quantization axis, along the z-direction. Transitions are described by the fermionic raising and lowering operators $\hat{\sigma} = |g\rangle \langle e|$ and $\hat{\sigma}^\dagger = |e\rangle \langle g|$. These fulfill the anticommutator relation $\left\{\hat{\sigma}, \hat{\sigma}^\dagger\right\} = 1$. If we choose the ground state as the point of zero energy, then the eigenenergy of the TLS is solely determined by the population in the excited stated as measured by $\hat{\sigma}^\dagger\hat{\sigma}$ in units of $\hbar\omega_a$. This results in the Hamiltonian for the TLS:

$$\mathcal{H}_a = \hbar\omega_a \hat{\sigma}^\dagger \hat{\sigma} \tag{2.14}$$

The remaining Hamiltonian $\mathcal{H}_i$ reflects the interaction between the dipole of the TLS and the electric field of the optical mode. In its general form, it is given by:

$$\mathcal{H}_i = \hat{\mathbf{d}} \cdot \hat{\mathbf{E}} \tag{2.15}$$

[1] In general, the operators $\hat{a}$ and $\hat{a}^\dagger$ therefore carry an index l. Since we typically only work with a single optical mode, we drop the index for simplicity of notation.

The dipole operator $\hat{\mathbf{d}} = q \cdot \mathbf{l}$ measures the electric dipole moment of a system which classically corresponds to the separation $\mathbf{l}$ between two charges q of opposite sign. As before, we choose the optical mode and atomic quantization axis along z and place the atom at an antinode of the field[2]:

$$\mathcal{H}_i = \hat{d} \cdot \hat{E}_x(t) = \hat{d} \cdot E_0 \left(\hat{a} + \hat{a}^\dagger\right) \tag{2.16}$$

We take a brief detour to understand the form of the dipole operator. It acts onto the states of the TLS. Atomic energy eigenstates, however, exhibit a well defined parity and, therefore, possess no dipole moment. As a result the diagonal terms vanish:

$$\begin{aligned} \langle g| \hat{d} |g\rangle &= 0 \\ \langle g| \hat{d} |e\rangle &= d \\ \langle e| \hat{d} |g\rangle &= d^* \\ \langle e| \hat{d} |e\rangle &= 0 \end{aligned} \tag{2.17}$$

In consequence, we may write the dipole operator as:

$$\hat{d} = d \left(\hat{\sigma} + \hat{\sigma}^\dagger\right) \tag{2.18}$$

Here, d is a complex prefactor that describes the dipole strength. Defining the single-photon coupling strength $g = \sqrt{\frac{\omega_f d^2}{2\hbar V \epsilon_0}}$, the interaction Hamiltonian becomes:

$$\mathcal{H}_i = \hbar g \left(\hat{\sigma} + \hat{\sigma}^\dagger\right) \left(\hat{a} + \hat{a}^\dagger\right) \tag{2.19}$$

Together with the previous results, we arrive at the so-called Rabi Hamiltonian[3]:

$$\mathcal{H} = \hbar\omega_f \hat{a}^\dagger \hat{a} + \hbar\omega_a \hat{\sigma}^\dagger \hat{\sigma} + \hbar g \left(\hat{\sigma} + \hat{\sigma}^\dagger\right) \left(\hat{a} + \hat{a}^\dagger\right) \tag{2.20}$$

The analytical solution to this Hamiltonian has only been found recently [Bra11]. This is surprising considering its importance. As a major obstacle, it lacks a second conserved quantity besides energy since the interaction Hamiltonian strikingly violates conservation of particle number:

$$\hat{\mathcal{H}}_i = \hbar g \left(\hat{\sigma}\hat{a}^\dagger + \hat{\sigma}^\dagger \hat{a} + \hat{\sigma}\hat{a} + \hat{\sigma}^\dagger \hat{a}^\dagger\right) \tag{2.21}$$

The first two terms describe processes that conserve particle number: deexcitation of the TLS creates a photon in the optical mode or annihilation of a photon is accompanied by excitation of the TLS. In contrast, the last two terms display simultaneous deexcitation and annihilation or excitation and creation. An early way out of this dilemma was proposed by Jaynes and Cummings

[2] We assume the dipole approximation holds, i.e. the atomic dimensions are much smaller than the optical wavelength and an atom experiences a spatially constant electric field.

[3] Note that we have dropped a $\frac{1}{2}\hbar\omega_f$ since it only causes an overall energy offset.

[Jay63]. The creation and annihilation operators were initially introduced as time varying amplitudes which now become $\hat{a} = \hat{\tilde{a}} \cdot e^{-i\omega_f t}$ and $\hat{a}^\dagger = \hat{\tilde{a}}^\dagger \cdot e^{+i\omega_f t}$, respectively[4]. Likewise, the raising and lowering operator oscillate at the transition frequency of the TLS, $\hat{\sigma} = \hat{\tilde{\sigma}} \cdot e^{-i\omega_a t}$ and $\hat{\sigma}^\dagger = \hat{\tilde{\sigma}}^\dagger \cdot e^{+i\omega_a t}$. Formally this corresponds to a change from the Schrödinger to the interaction picture:

$$\hat{\mathcal{H}}_i = \hbar g \left(\hat{\tilde{\sigma}} \hat{\tilde{a}}^\dagger e^{i(\omega_f - \omega_a)t} + \hat{\tilde{\sigma}}^\dagger \hat{\tilde{a}} e^{i(\omega_a - \omega_f)t} + \hat{\tilde{\sigma}} \hat{\tilde{a}} e^{-i(\omega_f + \omega_a)t} + \hat{\tilde{\sigma}}^\dagger \hat{\tilde{a}}^\dagger e^{i(\omega_f + \omega_a)t} \right) \quad (2.22)$$

The last two terms oscillate rapidly at the sum frequency $(\omega_f + \omega_a)$, while the particle number conserving terms are only evolving slowly at $(\omega_f - \omega_a)$. If the TLS is near resonant to the optical mode ($|\omega_f - \omega_a| \ll \omega_f + \omega_a$), then the quickly oscillating terms average out in the temporal mean. With this so-called rotating wave approximation, we arrive at the famous Jaynes-Cummings Hamiltonian after transformation back to the Schrödinger picture:

$$\mathcal{H} = \hbar\omega_f \hat{a}^\dagger \hat{a} + \hbar\omega_a \hat{\sigma}^\dagger \hat{\sigma} + \hbar g \left(\hat{\sigma} \hat{a}^\dagger + \hat{\sigma}^\dagger \hat{a} \right) \quad (2.23)$$

The corresponding eigenvalue equation is solved by the dressed-states with ground state $|0, g\rangle$ and the excited states $|n, \pm\rangle$:

$$|n, +\rangle = \sin\theta \, |n, g\rangle + \cos\theta \, |n-1, e\rangle \quad (2.24a)$$

$$|n, -\rangle = \cos\theta \, |n, g\rangle - \sin\theta \, |n-1, e\rangle \quad (2.24b)$$

Here, n becomes the number of excitations in the system and θ is the mixing angle with detuning $\delta = \omega_a - \omega_f$:

$$\tan\theta = \frac{2\sqrt{n}g}{\delta + \sqrt{(2\sqrt{n}g)^2 + \delta^2}} \quad (2.25)$$

The corresponding eigenenergies are found to be:

$$\mathcal{E}_{(n),\pm} = \hbar\omega_f n + \frac{1}{2}\hbar \left((\omega_a + \omega_f) \pm \sqrt{(2\sqrt{n}g)^2 + \delta^2} \right) \quad (2.26)$$

In case of positive detunings ($\delta > 0$), the $|n, +\rangle$ have a stronger contribution from the TLS while the $|n, -\rangle$ are more photon-like[5]. The situation reverses for negative δ. At resonance ($\delta = 0$), TLS and field contribute equally to both states, however, a finite energy splitting persists. This situation is referred to as avoided crossing. The dressed-states at resonance simplify to $|n, \pm\rangle = (|n, g\rangle \pm |n-1, e\rangle) / \sqrt{2}$ and form an anharmonic ladder of doublets that are split by $2\sqrt{n}g$ (Figure 2.1(c)). In the time domain, this manifests as an oscillatory energy exchange between the optical mode and the TLS at rate

[4] To keep things short, we have omitted the derivation of the explicit time dependence via the Schrödinger equation.

[5] In the limit of very far detunings, we recover the undisturbed TLS and field.

$2\sqrt{n}g$. As reflected by the dressed states, only the superposition of the states of the optical mode and TLS yields proper stationary eigenstates of the joint system. This is very similar to the classical analogue of two pendula coupled via a spring where two new modes arise from the in-phase and out-of-phase oscillation. In stark contrast however, the latter exhibits no notion of excitation quanta and the new modes form two separate harmonic ladders as expected for two independent oscillators of eigenfrequencies $\omega_c + g$ and $\omega_c - g$ [Har06].

The huge interest to realize the Jaynes-Cummings Hamiltonian derives from that last result: A TLS coupled to an optical mode responds nonlinear already at the level of a single excitation [Cha14]. The distinct photon number dependent response constitutes an effective photon-photon interaction which is a key element for our realization of single- and two-photon blockade in Chapter 3.

2.1.2. Master Equation and Open Quantum Systems

Equation (2.23) describes an isolated quantum system. Any realistic system, however, will be coupled to the environment, which is modeled as a thermal bath, via dissipative processes. Examples for dissipation are photons that leak out of the considered optical mode or spontaneous emission of the two-level system into free space. The reverse processes, i.e. spontaneous excitation of the TLS or field mode from the thermal bath, are negligible at room temperature, since optical contributions of black-body radiation only become significant above 1000 K. As dissipative processes due to the environment cause decoherence, great experimental effort is focused on reducing their influence and restricting the irreversible coupling to very specific input and output channels to extract useful information, as discussed in the next section [Har89, Wal92]. In this section, we want to explore how such an open quantum system can be described quantitatively. We follow the approaches of References [Car93] and [Mey07].

Dissipation or excitation resulting from coupling to the environment will cause the quantum system that is prepared in an eigenstate to decohere into a mixture of states. Therefore, we will now describe its state by a density matrix $\rho = \sum_i p_i \left|\psi_i\right\rangle \left\langle\psi_i\right|$ that is a statistical ensemble of several quantum states ψ_i with probability p_i. In addition to the system Hamiltonian $\hat{\mathcal{H}}_S$, we also have to include the Hamiltonian of the environment $\hat{\mathcal{H}}_R = \sum_j \hbar\omega_j \hat{a}_j^\dagger \hat{a}_j$ that we model as a reservoir of harmonic oscillators, i.e. in our case the continuum of modes of the quantized electromagnetic field in free space. Interaction between the two is described by $\hat{\mathcal{H}}_{RS}$ that is assumed to be linear in system and bath operators, $\hat{\mathcal{H}}_{RS} = \hbar \sum_{i,j} g_{i,j}(\hat{O}_i^\dagger \hat{a}_j + \hat{O}_i \hat{a}_j^\dagger)$. Here, $\hat{O}_i$ is a system operator. This follows the same language, we introduced before: Energy exchange between system and reservoir consists of simultaneous annihilation of a system excitation and creation of a quantum in mode j of the bath or the reverse process. We assume the reservoir to be large such that its state remains practically unchanged and

that correlations within the bath decay much faster than the time scale of interest that in turn must be small compared to the system's evolution. The latter is referred to as Markoff approximation.

The joint system is now described by the density matrix $\rho_{RS}(t)$ and its temporal evolution is governed by the von Neumann equation:

$$\dot{\rho}_{RS}(t) = \frac{1}{i\hbar}\left[\hat{\mathcal{H}}_S + \hat{\mathcal{H}}_R + \hat{\mathcal{H}}_{RS}, \rho_{RS}(t)\right] \tag{2.27}$$

The system's density matrix can be recovered by tracing out the reservoir:

$$\rho(t) = \mathrm{tr}_R\left(\rho_{RS}(t)\right) \tag{2.28}$$

If we do the Born approximation, i.e. only taking terms linear in $\hat{\mathcal{H}}_{RS}$ into account, we find the Lindblad master equation for the density matrix:

$$\dot{\rho}(t) = -\frac{i}{\hbar}\left[\hat{\mathcal{H}}_S, \rho(t)\right] + \sum_i \left(2\hat{C}_i\rho(t)\hat{C}_i^\dagger - \rho(t)\hat{C}_i^\dagger C_i - \hat{C}_i^\dagger\hat{C}_i\rho(t)\right) \tag{2.29}$$

Here, the first term describes the coherent evolution of the isolated system and the second term models the non-unitary coupling to the environment. The newly introduced generalized dissipation operators $\hat{C}_i = \sqrt{\gamma_i}\hat{O}_i$ contain the dissipation rates γ_i that result from integration over the coupling to all reservoir modes and thus quantify the interaction strength with the environment. This interaction is irreversible since we imposed an environment "without memory" in the Markoff approximation. The equation of motion can be expressed in terms of the Lindblad superoperator $\mathcal{L}$:

$$\dot{\rho}(t) = \mathcal{L}\rho(t) \tag{2.30}$$

We find a formal solution by:

$$\rho(t) = e^{\mathcal{L}t}\rho(0) \tag{2.31}$$

At timescales long compared to the dissipative processes, the system will relax to a steady state $\mathcal{L}\rho_{ss} = 0$. Thus, we find the time dependent as well as the steady state expectation values for an arbitrary experimental observable $\hat{O}$:

$$\langle\hat{O}(t)\rangle = \mathrm{tr}\left(\hat{O}e^{\mathcal{L}t}\rho(0)\right) \tag{2.32}$$

$$\langle\hat{O}\rangle_{ss} = \mathrm{tr}\left(\hat{O}\rho_{ss}\right) \tag{2.33}$$

As a third measure, we use correlations between observables. These grant insight into the dynamics of the system. The quantum regression theorem [Lax63] introduces an efficient way to calculate correlations between different observables at time delay τ:

$$\langle\hat{O}_i^\dagger\hat{O}_j^\dagger(\tau)\hat{O}_j(\tau)\hat{O}_i\rangle = \mathrm{tr}\left(\hat{O}_j^\dagger\hat{O}_j e^{\mathcal{L}\tau}\left[\hat{O}_i\rho_{ss}\hat{O}_i^\dagger\right]\right) \tag{2.34}$$

This can be interpreted as following: The first observation projects the system out of the steady state into the new state $\hat{O}_i\rho_{ss}\hat{O}_i^\dagger$ whose subsequent evolution back to the steady state is then described by the Lindblad operator interrupted after a time delay τ by a second observation.

2.1.3. Example: Strongly Coupled Two-Level Atom

Observation of the fundamental building block of light-matter interaction described by the Jaynes-Cummings Hamiltonian in Equation (2.23) has been at the center of great experimental efforts in various different systems [Vah03, Boc04, Wal04, Mau05, Wal06, Kat15, Chi16b]. A major difficulty is posed by the continuum of free-space modes that surround any emitter, as we discussed in Section 2.1.2. For the derivation of the Jaynes-Cummings Hamiltonian, we only considered a single mode. But what distinguishes this one mode from the plethora of available modes that we identified as the origin of dissipation? The answer lies in the coupling strength g we introduced earlier as:

$$g = \sqrt{\frac{\omega_f d^2}{2\hbar V \epsilon_0}} \tag{2.35}$$

It quantifies the interaction strength between the electric field and the TLS. While eigenfrequency ω_f ($= \omega_a$ at resonance) and dipole moment d are characteristics of the emitter and cannot easily be tuned, the mode volume V plays a central role. In free space, the spatial extend of the mode is not restricted and as a consequence the mode volume diverges[6]. The strength of interaction remains weak and any coherent coupling to the TLS will be obscured by the dissipation to all other modes. However, if we restrict the spatial extend of that one specific mode via two mirrors that form a cavity, we can reduce the mode volume considerably which strongly enhances the vacuum fluctuations (due to the Heisenberg uncertainty) and electric field per photon[7]. The coherent energy exchange between TLS and optical field can then be observed if the rate of interaction, as described by the coupling strength, exceeds the dissipation rates of the system due to the coupling to all other modes, $g \gg \gamma_i$. This is often referred to as the strong coupling condition. Practically, it requires a sufficiently small mode volume to achieve a large coupling per photon. As the mode volume strongly depends on the mirror separation, the cavity length L plays a key role in reaching strong coupling.

Another route is engineering the environment by reducing the number of accessible modes which in turn will decrease the dissipation rates [Har89]. This is achieved by enforcing boundary conditions on the free-space modes thus cutting down the continuum to discrete solutions. If for example the confining length scale orthogonal to the mode of interest is chosen below half a wavelength, it cannot support any mode at the frequency of interest and consequently the spontaneous emission in this direction is suppressed. The

[6] For this reason, a free-space mode is not well-defined since it cannot be normalized.

[7] Note that this also causes an excited atom to predominantly emit into the cavity mode as the mode with the strongest contribution to the dissipation rate, an effect known as Purcell effect [Pur46]. This picture, however, partly breaks down as the coupling becomes reversible and new eigenstates emerge.

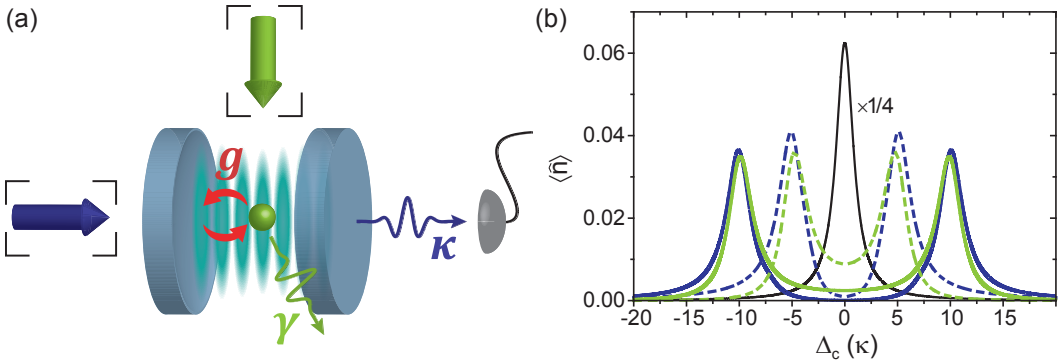

Figure 2.2.: Atom-cavity system. (a) An atom-cavity system is excited either via the cavity (blue arrow) or atom (green arrow). The emission from the cavity is monitored on a detector. (b) Tuning the frequency of the probe field yields the spectrum for the uncoupled (black) and coupled cavity driven (blue) as well as atom driven (green) system. Solid (dashed) lines show the steady state expectation value of the photon number for $g = 10\kappa$ ($g = 5\kappa$), $\Delta_{ac} = 0$, $\gamma = 3/2\kappa$, $\eta_c = \eta_a = \kappa/2$.

resulting dissipation rate is smaller than the one in free space since the number of integrated modes is reduced. Though great progress has been made [Nod07], we abandon this topic as it remains unimportant for our specific realization.

Here, we want to consider an optical cavity QED system that consists of a single two-level atom with eigenfrequency ω_a and polarization decay rate γ coupled with coupling strength g to an optical cavity of eigenfrequency ω_c and field decay rate κ, i.e. leakage of the light field out of the cavity, as depicted in Figure 2.2(a). The strong coupling condition becomes $g \gg (\kappa, \gamma)$. We apply an additional drive $\hat{\mathcal{H}}_d$ at frequency ω_d to probe the system by displacing it from the ground state and detecting emission from the cavity. This drive is either incident on the cavity in which case it adds photons to the light field and takes the form $\hat{\mathcal{H}}_d = \hbar\eta_c\,(\hat{a}+\hat{a}^\dagger)$ or it excites the atom and is described via $\hat{\mathcal{H}}_d = \hbar\eta_a\,(\hat{\sigma}+\hat{\sigma}^\dagger)$ where η_c and η_a are the respective driving strengths. The latter shows how weakly interacting fields couple to the atom. Inserting the electric field described by classical amplitudes into the interaction Hamiltonian in Equation (2.15) directly yields the above result.

If we transform Equation (2.23) into a frame rotating at ω_d, then the full Hamiltonian for the driven CQED system becomes:

$$\hat{\mathcal{H}} = \hbar\Delta_a\,\hat{\sigma}^\dagger\hat{\sigma} + \hbar\Delta_c\,\hat{a}^\dagger\hat{a} + \hbar g\,(\hat{a}^\dagger\hat{\sigma} + \hat{\sigma}^\dagger\hat{a}) + \hat{\mathcal{H}}_d \tag{2.36}$$

Here, $\Delta_a = \omega_d - \omega_a$ ($\Delta_c = \omega_d - \omega_c$) is the atom (cavity) detuning with respect to the driving frequency. The atom-cavity detuning is then defined as $\Delta_{ac} = \omega_a - \omega_c$. We identify the associated generalized dissipation operators as $\hat{C}_a = \sqrt{\gamma}\hat{\sigma}$ and $\hat{C}_c = \sqrt{\kappa}\hat{a}$ and construct the Lindblad superoperator according to Equation (2.29). Numerical solutions for different measures and observables,

as described in Section 2.1.2, can then be found via e.g. the Quantum Optics Toolbox for Matlab [Tan99] or the Quantum Toolbox in Python (QuTiP) [Joh13]. In Figure 2.2(b), we show the spectrum versus cavity-probe detuning by calculating the steady state expectation value for the photon number $\langle\hat{n}\rangle_{ss} = \left\langle\hat{a}^\dagger\hat{a}\right\rangle_{ss}$. Without coupling ($g = 0$), we observe the Lorentzian of the empty cavity with a linewidth of 2κ. This splits into two new modes for the coupled system at frequencies $\pm g$ with linewidths of $\frac{\kappa+\gamma}{2}$ referred to as normal modes. These reflect the first doublet of the Jaynes-Cummings ladder $|1,\pm\rangle$ (Figure 2.1(c)) and agree with the classical expectation for two coupled pendula. Both spectra for atom and cavity excitation seem very similar, but disagree around $\Delta_c = 0$. This is the consequence of an antiresonance in case of cavity probing due to destructive interference between the coherent drive and the field radiated by the atom that keeps the cavity unexcited [Sam14].

2.2. Apparatus & Atom Position Control: A 3D Atom Microscope

The term 3D atom microscopy can be interpreted in two different ways. On one hand, it may refer to the localization of single atoms (in cavities) in all dimensions which has been a central topic for many years [Hoo98, Hoo00, Rei13]. Besides the obvious curiosity on how the atom moves about in its potential landscape, it serves the very practical purpose of maximizing the coupling strength by enabling position control of the atom to the very maximum of the cavity field [Pin00, Nuß05a]. This is of central importance due to the limited atom-cavity coupling strength that has so far been obtained in the optical regime [Dev07]. A major limitation is posed by the direct dependence of the coupling constant on the atomic dipole moment that in turn causes large polarization decay rates. Therefore, the best tuning knob is the mode volume that depends on the waist of the optical mode and the cavity length. The latter, however, affects the resonance frequency and we will see that we are not always free to choose here. Alternatively minimizing the waist is a very challenging technical topic. Only recently developed, novel fiber cavities display significant improvements on the waist and a corresponding increase of the coupling strength [Col07, Mul10]. For now, we need to be as close as possible to the coupling strength achievable in our system to work in the strong coupling regime of CQED. This is taken one step further in Chapter 4, when the relative position with respect to two spatially differing modes has to be precisely adjusted.

Such atom positioning requires a proper cooling technique, sub-wavelength trapping potentials and knowledge about the absolute position in three-dimensional space. Mastering all of these, we achieve a record atom-cavity coupling strength of 97 % of the theory value.

On the other hand, 3D atom microscopy may also refer to the atom playing the role of the probe. In fact, a well-localized atom in free space can be employed as a very sensitive spatial sensor to probe its electromagnetic environment. Atomic ions that exhibit strong coulomb interaction have, thus, been used to measure light-induced charging effects on dielectrics [Har10] or to sense sub-attonewton forces in three dimensions [Blu17]. A single ion [Gut01] and a beam of neutral atoms [Lee14], on the other hand, have been used to probe the cavity vacuum field, a quest we will also embark on with our stationary atom.

We start by introducing the apparatus and atom trapping in Section 2.2.1 to get an understanding of the experimental system and general working principle. In Section 2.2.2, we describe the imaging and positioning of atoms. We demonstrate how we count their number and localize them in three dimensions. The latter allows us to employ them as a probe for the cavity vacuum field. Finally, we use that newly available information to stabilize the atom's position to the region of maximum coupling strength.

2.2.1. Apparatus and Atom Trapping

Our system consists of single ^{87}Rb atoms coupled to a high-finesse ($\mathcal{F} = 195\,000$) Fabry-Pérot resonator of variable length L (150 µm to 5 mm) adjusted to 202 µm (Chapters 2 and 3) or 295 µm (Chapter 4). Figure 2.3(a) shows a sketch of the complete system.

Cavity Mode. The resonator is formed by two spherical mirrors with high-reflectivity dielectric coatings of curvatures 1 cm and 20 cm. Most of the technical details are given in Reference [Koc11a] and summarized in Appendix A. In short, the cavity supports a TEM_{00} mode that is of Gaussian shape in the radial direction and has a standing wave pattern modulated at half the wavelength axially. The frequency spacing between two neighboring longitudinal modes that fulfill the boundary conditions of the mirrors follows Equation (2.5), $\nu_{\mathrm{FSR}} = c/2L$, and is referred to as free spectral range (FSR). In our case for cavity lengths of 202 µm or 295 µm , it amounts to 750 GHz or 500 GHz. The cavity field decay rates $\kappa/2\pi$ are calculated to be 1.9 MHz and 1.3 MHz at 780 nm excluding birefringence (≈ 180 kHz) which causes measured rates of 2.0 MHz and 1.5 MHz. The mode waist w_0 at which the field strength (intensity) falls to $1/e$ ($1/e^2$) of its amplitude in the radial direction is found to be 18.6 µm or 20.4 µm, respectively. The small spacing of the mirrors compared to their curvatures yields a large Rayleigh range, z_R, of 1.4 mm or 1.7 mm which gives the distance from focus at which the area of the cross section is doubled. Since z_R is much larger than the cavity lengths, we approximate the mode as a cylinder. The spatial mode function of the field for the cavity along the z-axis

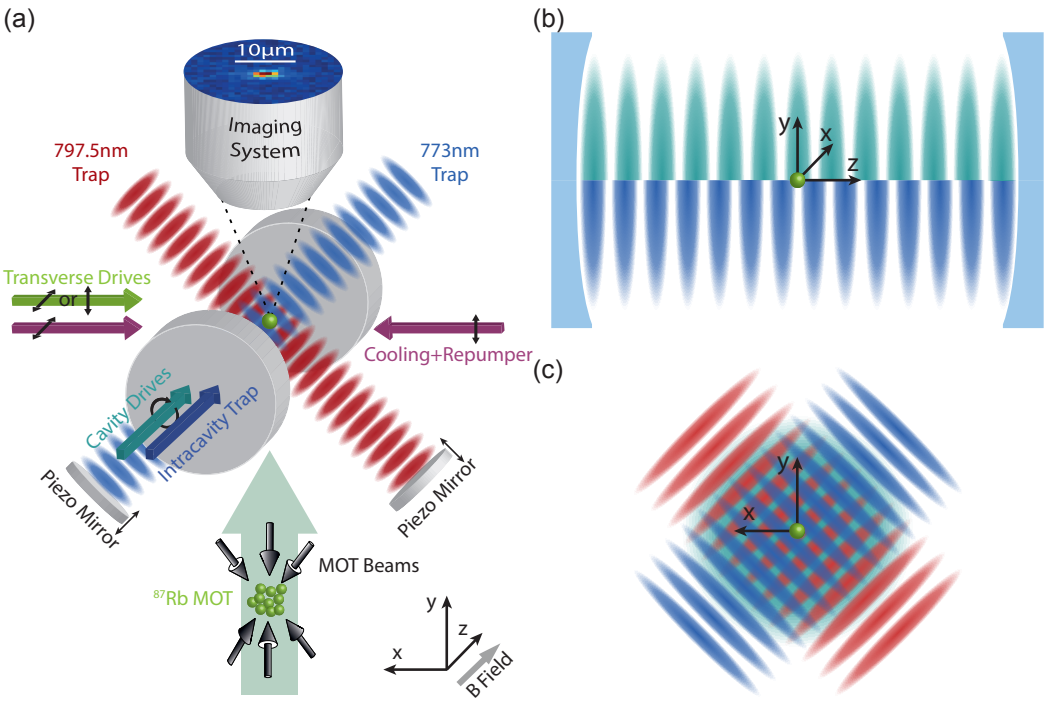

Figure 2.3.: Apparatus and trap geometry. (a) The sketch shows the apparatus used for the experiments in this thesis. (b) The intracavity probe (cyan) and trap (blue), omitted in (a) for clarity, are shown exemplary for neighboring longitudinal ($\Delta l = 1$) modes. (c) The orthogonal transverse traps cross at angles of 45° to the horizontal plane.

is then given by:

$$f_m(\mathbf{r}) = \cos\left(\frac{2\pi}{\lambda}z\right) e^{-\frac{x^2+y^2}{w_0^2}} \tag{2.37}$$

This function describes the spatial variation of the cavity field and consequently also the change of coupling strength $g(\mathbf{r}) = g \cdot f_m(\mathbf{r})$ when displacing atoms from the mode center at $(x, y, z) = (0, 0, 0)$. We will directly observe the Gaussian envelope in Section 2.2.2 via 3D atom microscopy. The axial modulation plays an important role in the motional dynamics observed in correlations in Chapter 3.

Dipole Traps. To ensure good localization and maximum coupling, atoms are confined to an antinode of the cavity field via a three-dimensional lattice of detuned, standing-wave optical dipole traps [Gri00, Rei13, Neu15b]. These exert a dipole force onto the atom that leads to a conservative trapping potential.

In brief, the electric field of the trapping light induces a dipole moment $\mathbf{p} = \alpha\mathbf{E}$ in the atom that, as we have seen before (Section 2.1.1), exhibits no permanent dipole moment in its ground state. Here, α is the polarizability

of the ground state. The interaction of the induced dipole with the inducing electric field yields a dipole potential that is, therefore, quadratic in the applied field: $U_t = -\frac{1}{2}\alpha|\mathbf{E}|^2 = -(c\epsilon_0)^{-1}\alpha I$. Here, $I = \frac{\epsilon_0 c}{2}|\mathbf{E}|^2$ is the light intensity. For a TLS in rotating wave approximation, one finds a simple solution for the trapping potential U_t when approximating the atom as a classical oscillator which allows us to get a qualitative understanding [Gri00][8]:

$$U_t = -\frac{3\pi c^2}{2\omega_a^3}\frac{2\gamma}{\Delta}I(\mathbf{r}) \tag{2.38}$$

Here, $\Delta = \omega_t - \omega_a$ is the detuning of the trap with frequency ω_t with respect to the atomic transition. We find that depending on the detuning the polarizability can be either positive or negative resulting in attractive or repulsive potentials. Dipole traps blue-detuned ($\omega_t > \omega_a$) to the nearest atomic transition tend to exhibit negative polarizabilities and a repelling potential while red-detuned ($\omega_t < \omega_a$) traps yield positive polarizabilities and attract atoms to regions of high intensity [Neu15a]. As the dipole moment is induced by off-resonant coupling to an atomic transition, it manifests itself as an energy shift of the atomic energy levels ΔS referred to as light shift or ac Stark shift. Consequently, red-detuned traps that localize atoms at antinodes of the field will cause a permanent light shift. The strength of this light shift is proportional to Δ^{-1} and closer resonances will therefore experience a larger shift than those that are farther detuned. We will use this to achieve differential shifting of two different transitions in ^{87}Rb in Section 4.3.

As seen before, the shape of the trapping potential is described by the square of the wave function of the laser beam which is given by $f_m^2(\mathbf{r})$ in the focus of a Gaussian beam. Consequently, it causes strong confinement in the axial direction ($\sim \lambda/2$) and weak confinement in the radial direction ($\sim w_0$). The overlap of three orthogonal standing-wave dipole traps in a three-dimensional lattice can then localize atoms to far below $\lambda/2$ in all directions [Rei13].

In our case, the lattice is formed by two blue- and one red-detuned traps [Tie14b]. One blue-detuned trap at 773.1 nm is an intracavity field detuned by $\Delta l = 5$ ($\Delta l = 7$ at 295 µm cavity length) FSRs to the resonant mode at 780.2 nm. As a result, it exhibits a spatial beating with the resonant mode as shown exemplary for $\Delta l = 1$ in Figure 2.3(b). It is easy to convince oneself that this leads to Δl regions where both fields are completely out of phase. Only atoms in those regions couple maximally to the resonant cavity mode, as the blue-detuned trap localizes them to its nodes. With a power of 1 µW measured behind the cavity, it causes a trapping potential of $U_t \approx h \cdot 24\,\mathrm{MHz} = k_B \cdot 1.1\,\mathrm{mK}$. In addition, this trap is used for length stabilization of the cavity via a Pound-Drever-Hall technique that feeds back onto a piezo tube separating the

[8]The full theory of ac Stark shifts to calculate quantitative results for real multi-level atoms is described in great detail and clarity in Reference [Neu15a].

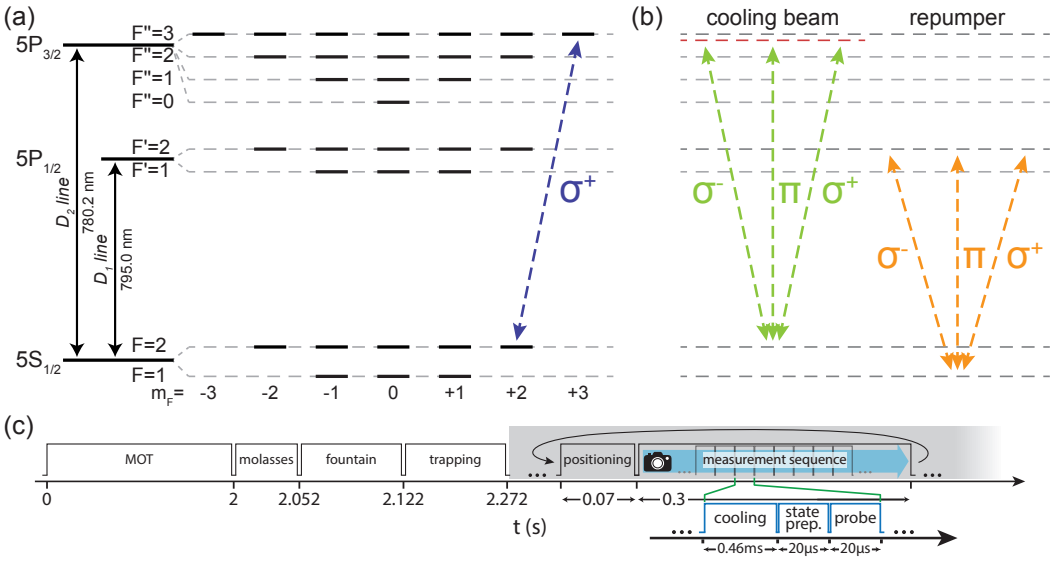

Figure 2.4.: Level scheme, cooling and sequence. (a) ^{87}Rb exhibits a complex level structure. Nevertheless, e.g. $|2,+2\rangle \leftrightarrow |3'',+3\rangle$ forms a cycling transition that serves as a TLS (blue). (b) Cooling applies a red-detuned beam that realizes a Sisyphus-type scheme with a repumper on the D_1 line. (c) The main part of the sequence consists of the measurement part during which also atom images are recorded.

mirrors [Dre83]. The red-detuned trap with a wavelength of 797.5 nm and the other blue-detuned trap (772.8 nm) are incident at 45° and −45° with respect to the y-axis in the x-y-plane orthogonal to the cavity z-axis (Figure 2.3(c)). Both beams have a waist of approximately 40 µm and, with powers levels of 500 mW and 180 mW, we estimate their depths to $U_t \approx -h \cdot 70\,\mathrm{MHz} = k_B \cdot 3.3\,\mathrm{mK}$ and $U_t \approx h \cdot 18\,\mathrm{MHz} = k_B \cdot 0.8\,\mathrm{mK}$, respectively.

Atomic Level Structure. The atomic energy level structure of ^{87}Rb is depicted in Figure 2.4(a). The alkali atom exhibits two stable hyperfine ground states, the $5S_{1/2}, F = 1$ and $F = 2$ detuned by 6.8 GHz. The first excited states are the $5P_{1/2}$ doublet at 795 nm referred to as D_1 line with polarization decay rate $\gamma_{D_1}/2\pi = 2.9\,\mathrm{MHz}$ and the $5P_{3/2}$ quadruplet at 780 nm known as D_2 line with $\gamma_{D_2}/2\pi = 3.0\,\mathrm{MHz}$. The hyperfine splitting within these manifolds varies between 70 MHz to 800 MHz. Both, the splittings of ground and excited states exceed the transition linewidths by more than one order of magnitude and are, therefore, well-resolved. The complete level scheme for the D lines of ^{87}Rb including the eigenfrequencies of the hyperfine states is given in Appendix A in Figure A.1. We will use the notation $|F, m_F\rangle$ or $|F', m_F\rangle$ and $|F'', m_F\rangle$ for the $5S_{1/2}$ ground states or $5P_{1/2}$ and $5P_{3/2}$ excited states, respectively. F is the quantum number of the total angular momentum of the hyperfine structure consisting of spin-orbit coupling and interaction with the non-zero nuclear spin

of 3/2. m_F corresponds to the z-component of the total angular momentum, also referred to as magnetic quantum number that denotes the Zeeman states.

Given the high finesse and small waist of our cavity and the atomic dipole strength of ^{87}Rb , we expect to be strongly coupled on any transition in the range from 150 µm to 500 µm where the lower limit is a technical constraint. The strongest atom-cavity coupling, however, is found on the cycling transition $|2, +2\rangle \leftrightarrow |3'', +3\rangle$. A cavity length of 202 µm in Chapters 2 and 3 results in $g/2\pi = 19.6\,\mathrm{MHz}$ and 295 µm in Chapter 4 yields $g/2\pi = 14.8\,\mathrm{MHz}$. Even though ^{87}Rb is a multi-level atom, this transition is closed and forms a real TLS. Due to the dipole selection rules $\Delta F = 0, \pm 1, \Delta m_F = 0, \pm 1$, and $\Delta F = 0, \Delta m_F \neq 0$, an atom in $|3'', \pm 3\rangle$ can only decay into $|2, \pm 2\rangle$ via a $\sigma^{\pm}$-transition (Figure 2.4(a)). While this two-level nature is pivotal for realizing the Jaynes-Cummings Hamiltonian in Chapter 3 and serves as a central ingredient to state detection in Section 2.3.1, we will go beyond such two-state systems and exploit the level structure, symmetries and selection rules in Chapter 4. In fact, the more complex but inherent energy level structure and long-lived ground states are one of the central advantages of real over artificial atoms [Bul11].

Sequence. Atoms are loaded into the cavity via an atomic fountain from a magneto-optical trap (MOT) 25 cm below (Figure 2.3) [Raa87]. The MOT resides in a separate vacuum chamber that is connected to the main chamber via a narrow tube. At the beginning of each sequence (Figure 2.4(c)), atoms evaporated from a rubidium dispenser are loaded into the MOT. After 2 s, we ramp down the MOT beam powers and increase their detunings within 50 ms, then switch off the magnetic field and cool the cloud of atoms to an optical molasses of about 5 µK [Dal89]. We let the system equilibrate for 2 ms, before we detune the upper cooling beams with respect to the lower in order to cool the atoms into a moving frame, thus, launching them towards the cavity. The cloud takes about 170 ms to overcome the distance of 25 cm to the cavity in the upper chamber. During this time, the atoms have to work against the gravitational force and fully convert their kinetic energy into potential energy such that they have on average zero velocity at the altitude of the resonator. This marks the turning point of the fountain after which the atoms will accelerate back downwards. Atoms passing between the two mirrors are attracted to and captured in the red-detuned dipole trap focused to the center of the cavity while the intracavity trap confines them on-axis. Since the cloud has spread due to its finite temperature of the atoms, the full transit takes about 30 ms.

After the loading, we ramp up the other transverse trap which encloses the atoms in three dimensions and start the actual experimental sequence. The latter consists of 370 ms long modules that are repeated until the atom is lost from the trap and we restart the sequence after a typical trapping time of 8 s. The first 70 ms of each module are used for atom positioning and during

the residual 300 ms we run the desired measurement sequence at a kHz rate preserving about 90 % of the time for cooling. A common sample sequence featuring cooling, state preparation and probing is depicted in Figure 2.4(c).

The required friction force to capture and cool atoms stems from cooling beams counterpropagating along the x-direction with orthogonal linear polarizations. This light is red-detuned by about 30 MHz with respect to the $F = 2 \leftrightarrow F'' = 3$ transition (Figure 2.4(b)) and leads to intracavity Sisyphus cooling in all directions [Nuß05b]. A weak transverse beam resonant to the $F = 1 \leftrightarrow F' = 2$ transition repumps atoms that end up in the $F = 1$ ground state due to off-resonant scattering.

The cooling light scattered by the atoms is collected with a high numerical aperture objective and detected using a sensitive EMCCD camera with an integration time of 300 ms matched to the measurement sequence. A sample image is shown in the upper part of Figure 2.3(a). The detection of the presence of atoms, their number and position in real-time will be described in detail in the next section. For each captured image, we calculate the deviation of the atom position from the cavity mode center along the x- and y-direction which is then fed back onto piezo motors that shift the standing waves of the transverse traps to realign atoms. During the data analysis, we postselect on single atoms well confined to the center of the cavity along x, y, and z.

The quantization axis is defined parallel to the cavity axis by an offset magnetic field along the z-direction of typically 0.4 G to 0.6 G.

Experimental Control. Technically, the slow experimental sequence including the cloud preparation, fountain, atom trapping and storing is handled by a CPU running a real-time (RT) operating system employing two field-programmable gate arrays (FPGA) for in- and output of digital and analog signals at a rate of 100 kHz [BS15]. In fact, neglecting the huge differences in architecture, the filling of the FPGAs' data buffers with simultaneous output and sequence control including triggers exhibits great similarities to the implementation of the display output of the original Super Mario game on the Nintendo Game Boy® [Ste16]. Furthermore, the RT system is synchronized to another CPU with a standard operating system that provides the user interface, handling of devices not capable of real-time and database connection for bookkeeping of the experimental settings. For the fast measurement sequence, the RT system temporary hands the control over to an external FPGA running at a clock rate of 50 MHz to compile sequences with time steps down to 20 ns.

2.2.2. Atom Imaging and Positioning

Once the cloud has passed the optical resonator, we need to continuously detect the atoms' presence and count their number, localize them in three dimensions and feed that information back to stabilize their position at the

cavity mode center. This has to be performed within the 70 ms time slot between the exposure times of the images and includes the downstreaming of the data from the camera. For the latter, we use another field-programmable gate array (FPGA) that directly reads the digital camera data consisting of pixel values with a resolution of 16 bit on a parallel bus transmitting with a clock rate of 10 MHz. Then, transfer of a typical 100×200 pixel image takes about 2 ms. The data is then copied to the computer for further processing via direct memory access (DMA), thus bypassing the CPU.

For data processing, we pursue two different strategies. In the first approach, we integrate the intensity in the region of interest (ROI) of the image and compare the calculated brightness values. This is mostly used for atom detection and counting but yields no spatial information. In the second approach, we detect and fit each atom which provides additional information on position. In a first step, we detect the rough position of a potential atom. We set a threshold of a few standard deviations above the mean count rate and identify an atom as a spot, i.e. a group of pixels, that exceeds this threshold. To ensure rapid processing in the second step, we select a region of typically 10×10 pixel around that spot and fit a two-dimensional Gaussian function to that data which yields amplitude, x- and z-position as well as the corresponding widths σ_x and σ_z. Finally, we cut out a region of 3 times the width in each direction around the center position from the original image and move to the next point that exceeds the threshold until no point fulfills the condition anymore which gives us the number of atoms. The second approach requires considerably more processor time that, in addition, fluctuates since it depends on the number of fitting iterations to achieve the predefined accuracy and, moreover, scales with the number of atoms. After some optimization, we achieved routines as fast as 5 ms per atom and, consequently, remain reliably below 30 ms overall processing time. The remaining 40 ms are then used for positioning.

The image quality depends crucially on the design and proper alignment of the optics. Our self-designed and -built objective with a high numerical aperture of $\mathrm{NA} = 0.47$ is matched to the specific geometry of the vacuum chamber and the variable length cavity. It consists of 5 spherical lenses to compensate aberrations plus a focusing lens [Eck13]. It provides a magnification of 16.5 which in conjunction with the 16 µm pixel size of the EMCCD yields a conversion of 0.97 µm/pxl and is found to be diffraction limited at a resolution of 1.07(1) µm. In addition, the camera objective exhibits a longitudinal resolution (along the optical axis) of 4.7 µm.

Detection and Counting. The foremost task is to detect the presence and number of atoms in order to decide whether to continue or restart the sequence. Figure 2.5(a)-(c) show three images with discernible atom numbers of 1 to 3 identified as bright spots on a comparably even background. However, in

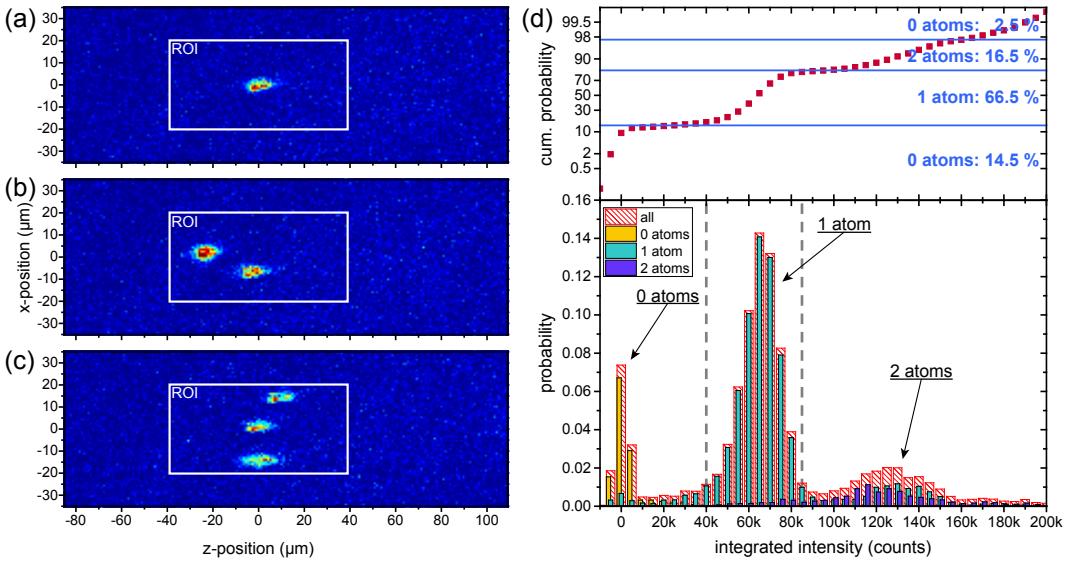

Figure 2.5.: Counting atoms. (a) One, (b) two, and (c) three atoms are identified in camera images as bright spots on a low-noise background. The integrated intensity in a given region of interest allows the detection of atoms even if these overlap spatially or jump. (d) The probability versus the integrated intensity in the ROI (white rectangles in (a)-(c)) corrected by the background mean exhibits clear peaks at integer multiples that are identified as number of atoms with a brightness of 65 kcts each. Yellow, cyan and purple bars correspond to data postselected on the atom number as determined from the Gaussian fit. The cumulative probability confirms that we work with a single atom in about 66.5 % of the time.

other cases atoms may spatially overlap, or jump during the image and show up as two spots of half brightness. The brightness per atom, i.e. the overall number photons scattered by one atom from the cooling beam and collected with the objective, remains constant for a given cooling power and detuning. As a result (lower part of Figure 2.5(d)), we find that the probability of the integrated intensity peaks at integer multiples of about 65 kcts. These are identified with number of atoms in the ROI. However, as indicated above, when comparing the fitted atom number to the integrated intensity, we find that the fit result for single atoms also displays a peak at 130 kcts, double the brightness per atom. Likewise, data postselected on two atoms from the fit also exhibits structure at the single atom intensity. The former stems from atoms that are too close to be separated by the fit and the latter from an atom that moved during the exposure time. In consequence, we use the integrated intensity during evaluation of the data to determine the proper number of atoms as indicated by the gray dashed lines.

The cumulative probability allows us to determine the fraction of modules with 0, 1 and 2 atoms. Note that this does not correspond to the probability

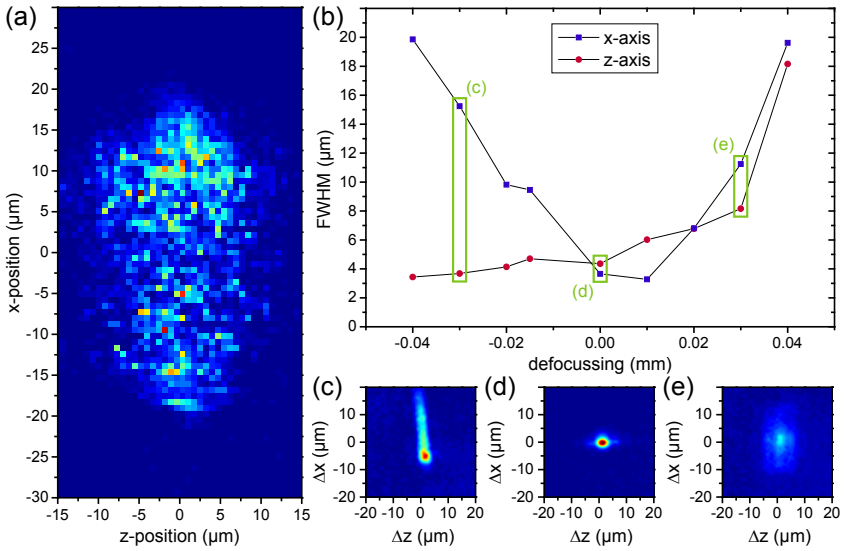

Figure 2.6.: Atom position distribution and objective focus. (a) The atom position distribution in the x-z-plane is found by recording the atoms' positions in over 12 000 images. (b) Defocusing from the focal plane causes an increase in the width of the atom images that is asymmetric in the z-direction. Figure (c)-(e) show the averaged images at defocusing of $-30\,\mu m$, $0\,\mu m$ and $30\,\mu m$ in (b). The asymmetry again reflected in (c) is not fully understood. For better display, (c) and (e) have been scaled in intensity by a factor of 2.

of atoms arriving at the cavity which we expect to be Poissonian, but takes into account all modules. By adjusting the dispenser current, we change the size of the ^{87}Rb cloud during MOT phase which in turn will change the mean number of atoms arriving at the cavity. This initial atom number will then decrease over time due to losses from the trap. With typical parameters, we find a single atom trapped in the cavity for about two thirds of the time.

3D Atom Microscopy. After detecting the presence and number of atoms, their localization is of central importance. While confinement to below half a wavelength in optical lattices and cooling close to the mechanical ground state have been addressed before [Nuß05b, Mur06, Kau12, Rei13, Les14], the absolute localization in space in all three dimensions remains an outstanding problem. However, it is prerequisite in order to position the atom at the point of maximum coupling.

The localization in the x-z-plane, orthogonal to the objective axis, is directly accessible via the images and has been shown to be measurable below $\lambda/2$ [Neu16]. The two-dimensional Gaussian fit directly yields the x- and z-coordinate. Figure 2.6(a) shows the position distribution for many repetitions of the experiment. Due to the red-detuned, transverse trap, we find the dis-

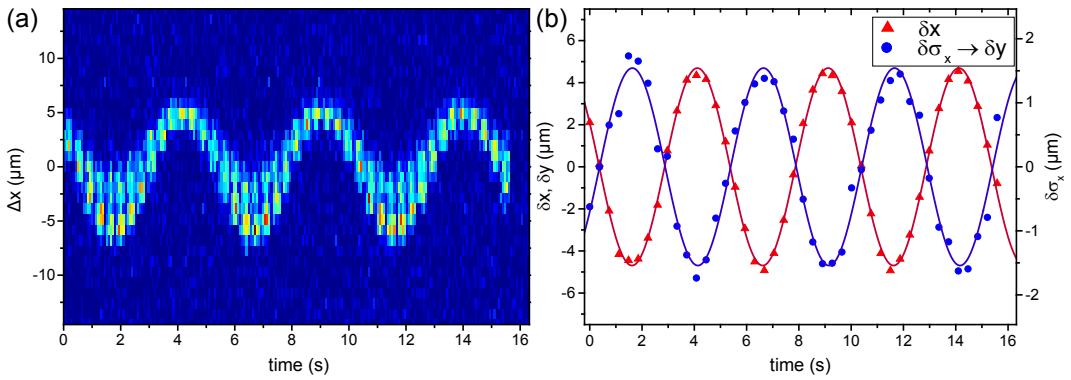

Figure 2.7.: Vertical position gauging via an oscillating atom. (a) Slices of 5 pxl width along z versus the x-axis deviation Δx are merged over time for a single atom trapped for 15 s. The atom is shifted in a sine wave along a 45° axis to the objective. (b) Fitting yields the relative position δx which, when compared to the relative width $\delta\sigma_x$ and considering that the change in position must be the same for both due to the angle of 45°, allows us to deduce the conversion from width to vertical position of $3.04\,\mu\text{m}_{[\delta y]}/\mu\text{m}_{[\delta\sigma_x]}$.

tribution to be elongated along the x-direction and narrow on the cavity axis. The vertical position along y is more complicated. However, the limited depth of field of our objective allows us to get information on the longitudinal position with respect to its focus. When shifting a point source or pinhole away from the focal plane one observes an increase of the image width and reduced peak intensity. In other words, the resolution decreases and an imaged object appears less sharp. Figure 2.6(b) shows the atom image width versus defocusing of the objective from the main trapping plane. We find an almost tenfold increase in width for a shift of the focal point by only 40 µm. While the behavior in x-direction is rather symmetric, the image broadening in z-direction is less pronounced and only present for positive defocussing. This is believed to result from clipping of fluorescent light on the cavity mirrors that may introduce an asymmetry. A quantitative understanding is complicated since we are not imaging a fixed pinhole but multiple atoms that are trapped at various heights and in-plane positions. In addition, these may move during the image or experience varying trapping potentials when far from the cavity center.

In order to achieve a good vertical resolution, we therefore choose the width along the x-axis as a measure. However, for atoms trapped in the focus of our objective, a broadening indicates their displacement, but does not yield the direction since the width increases for both, inside- and outside-focus. The solution is similar to the side-of-fringe locking method for laser stabilization to a reference cavity [Bar73]: A decrease of transmitted intensity of a laser tuned to the center of the Lorentzian resonance of the reference cavity does not yield

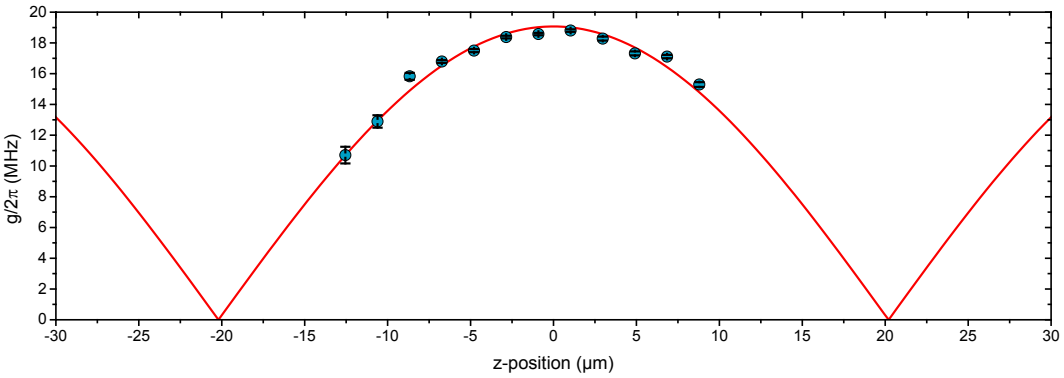

Figure 2.8.: Coupling strength along the cavity axis. The dephasing between the intracavity trap and the resonant mode due to a detuning of $\Delta l = 5$ FSRs causes atoms to experience a decreasing coupling strength along the cavity axis away from its center with a periodicity of $L/\Delta l = 40.4\,\mu\text{m}$. Data is taken the same way as for Figure 2.9 and the red line shows a theory for atoms localized at the nodes of the blue-detuned trap with the vertical scaling as the only free parameter.

information whether the laser frequency has increased or decreased. This is circumvented by shifting the laser to the side of the fringe where the intensity is a monotonous function of the laser frequency. In our case, we slightly defocus the objective from the cavity mode center such that the atom's width becomes a monotonous function of the vertical position. In order to demonstrate the working principle and gauge the image width to a vertical position, we put a sinusoidal voltage modulation with a frequency of 0.2 Hz and an amplitude of 0.6 V onto the piezo mirror of the 797.5 nm trapping arm (Figure 2.3(a)). This causes a corresponding oscillation of the standing wave pattern along the axial direction of the trap which will in turn shift an atom localized to an antinode with it. The trap exhibits an angle of 45° (−45°) to the x-axis (y-axis). The resulting images for one trapped atom over time are depicted in Figure 2.7(a). We observe a clear oscillation in both, position and width along x, until the atom is lost after 15 s. We plot the fit values in Figure 2.7(b) for a quantitative analysis. Both follow a clear sinusoidal behavior with a frequency of 0.2 Hz and are exactly π out-of-phase. The piezo shift is given in the datasheet as 10 μm/V and considering the projection onto the x-axis, we find an expected modulation amplitude of 4.2 μm in good agreement with the fitted oscillation amplitude of 4.7(1) μm. Due to the 45° angle, the projection onto the horizontal and vertical axis must be the same which allows us to calculate the conversion from image width to vertical position change.

Knowing the conversion from vertical shift to change in width, we can now find our absolute position in space. The intracavity trap inherently localizes atoms along the cavity axis. We only observe the increasing dephasing to the resonant probe mode due to the detuning by 5 FSRs, as depicted in Figure 2.8.

Since it cannot be shifted, we drop the corresponding z-axis for now and get back to it in Section 4.3.3 to observe the different beatings for two probe fields. Nevertheless, it is crucial to postselect atoms in a region where the intracavity trap and probe field are exactly out-of-phase to ensure maximum coupling.

We run a sequence to measure the normal modes on the cycling transition. During the state preparation of the measurement sequence, we optically pump the atom to the $|2,+2\rangle$ state by driving the cavity with a right-circularly-polarized probe as described in more detail in Section 3.3. In the probing interval, we then switch the probe beam to a different detuning that is scanned from $\Delta_c = -30\,\mathrm{MHz}$ to $+30\,\mathrm{MHz}$ throughout the 300 ms of each measurement module and record the transmission. Consequently, we take a full normal mode spectrum per measurement module, and thus many spectra per atom. After many repetitions, we can then investigate this spectrum as a function of position during the modules.

Figure 2.9(a) shows three sample spectra taken at different positions (x, y) relative to the cavity mode center that show good agreement with our simulation in Section 2.1.3. The fits with a semiclassical theory according to Appendix B yield coupling strengths of $g/2\pi = 18.5\,\mathrm{MHz}$, 12.3 MHz and 6.9 MHz that decrease with increasing displacement $|r| = \sqrt{x^2 + y^2}$ of 2.6 µm, 12.4 µm and 20.9 µm. This change in coupling is expected to follow the spatial mode function of Equation (2.37) and in fact, when plotting $g/2\pi$ along both axes in Figure 2.9(b), we recover the expected Gaussian envelope with cavity mode waists of $w_0 = 19.1(4)\,\mu\mathrm{m}$ along the x-axis and $w_0 = 21.9(6)\,\mu\mathrm{m}$ along the y-axis which is in reasonable agreement with our expected value of $w_0 = 18.6\,\mu\mathrm{m}$. The full two-dimensional map of the coupling constant is depicted in Figure 2.9(c). This essentially images the vacuum field enhanced via the cavity [Gut01, Lee14].

In addition, the fit also yields the detuning Δ_{ac} of the atomic transition to the cavity resonance that varies since atoms trapped at different sites experience varying light shifts due to their displacement with respect to the red-detuned dipole trap[9]. The two-dimensional map is depicted in Figure 2.9(d). Atoms trapped close to the center of the trap experience a larger light shift than those farther away. The corresponding transition frequency, remains almost constant along the diagonal axis from lower left to upper right that coincides with the 797.5 nm trap. On the other hand, it goes down away from the center in the anti-diagonal direction which is expected to follow the radial Gaussian shape of the trap. The spectra in Figure 2.9(a) were chosen along the axis of the red-detuned trap and, therefore, display an equal light shift that is set

[9]Remember that the red-detuned trap only confines atoms along its strong axial direction to its antinodes while localization along the other axes is provided by the blue-detuned traps. As a result, we do not observe light shifts due to the atom's position along the red-detuned trap which only shows up as a temperature-dependent shift and broadening of the atomic transition as described in Appendix B.

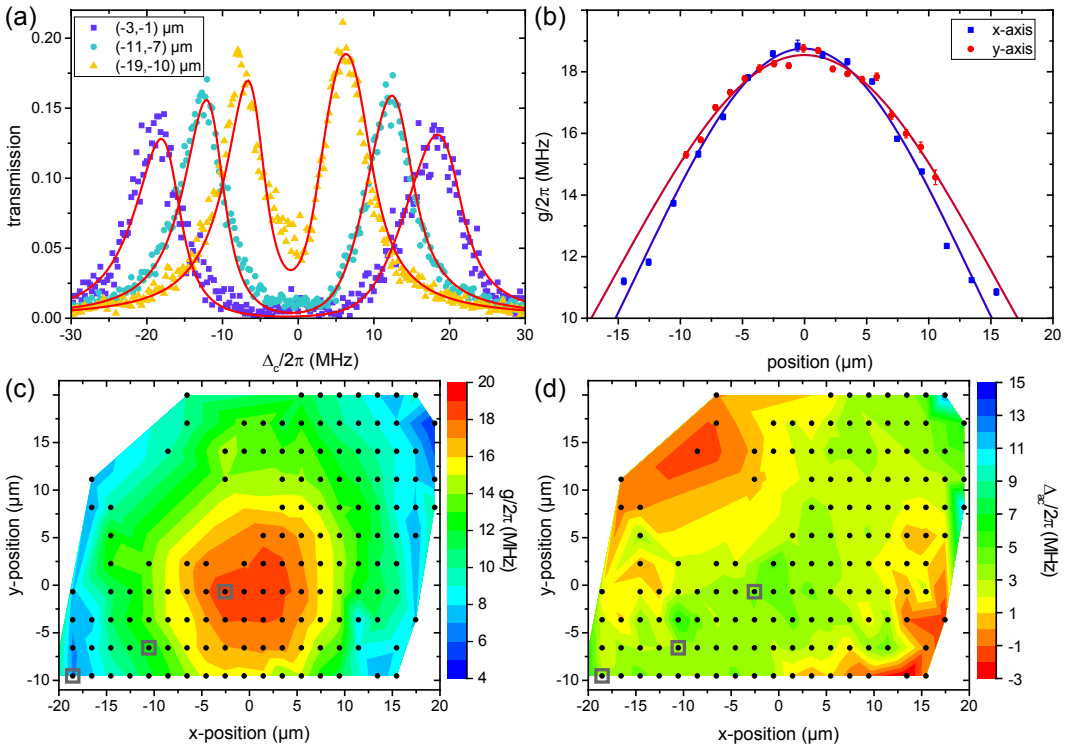

Figure 2.9.: Microscopy of the vacuum field with an atom probe. (a) Spectra at varying positions within the cavity are fitted by a semiclassical theory considering a finite temperature of the atoms (Appendix B) which yields coupling strengths of $g/2\pi = 18.5\,\mathrm{MHz}$, 12.3 MHz and 6.9 MHz that decrease away from the cavity center. (b) Atoms displaced along the radial axes show the expected Gaussian shape of the cavity field mode with waists of $w_0 = 19.1(4)\,\mu\mathrm{m}$ along x and $w_0 = 21.9(6)\,\mu\mathrm{m}$ in the y-direction. Interpolation of binned data (black dots) yields a two-dimensional reconstruction of the cavity mode via the coupling strength in (c) and of the profile of the red-detuned dipole trap via the atomic light shift in (d).

to compensate the bare atom-cavity detuning to $\Delta_{ac} \approx 0$ causing symmetric normal modes.

Positioning. Knowledge of the exact position relative to the cavity mode and trap allows us to only select those atoms which are well-localized to the center. However, a strict postselection causes a poor efficiency since most traces have to be disregarded. In fact, only about 1.0 % of the data fall within a region of at least 97 % of the maximum field amplitude. To improve the data rate it is better to not only detect the atoms' positions but also shift them to the point of maximum coupling. A natural solution is to employ the piezo mirror used for the modulation along the axis of the red-detuned trap in the previous section. Applying the same voltage to the piezo motors of both

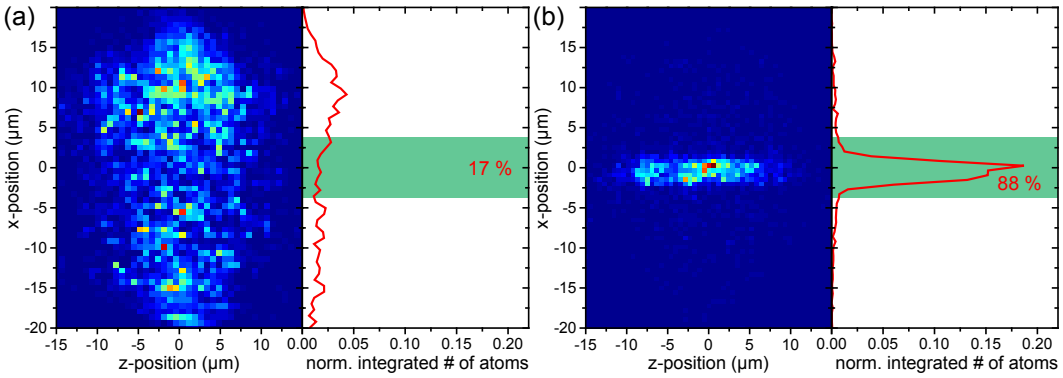

Figure 2.10.: Stabilization of the atom position in x-direction. (a) The initially broad atom distribution along x can be condensed to (b) a narrow strip of only few µm in width via position stabilization which greatly increases the postselection efficiency from 17 % to 88 %.

transverse traps leads to a change of the vertical position only, whereas opposite voltages vary the horizontal. Results for horizontal stabilization employing a simple proportional feedback loop are depicted in Figure 2.10. The initially broad distribution spanning more than 30 µm along x condenses to a small region of only 5 µm. Atoms postselected to a maximum displacement Δx of ± 3 µm from the mode center still experience 97 % of the maximum coupling strength. The corresponding efficiency, i.e. number of atoms that fall within the bounds relative to all atoms, increases drastically from 17 % to 88 % due to the stabilization.

We follow the same strategy for the vertical axis to control the height with respect to the cavity center. We stabilize to an atomic width of roughly 4 µm and again observe a significant narrowing of the position distribution as shown in Figure 2.11(a). The efficiency for a width interval corresponding to ± 3 µm displacement increases from 22 % to 82 %. The peak around a width of 2 µm for the data without position stabilization is expected to result from atoms right at the focal point where the vertical resolution deviates from our linear approximation and worsens considerably as the gradient approaches zero. Furthermore, if we postselect the z-axis and stabilize the x- and y-axes, we measure a normal mode spectrum with a prominent splitting corresponding to a coupling strength of 19.0 MHz which amounts to 97 % of the theoretical maximum and is in great agreement with our stabilization limits. This also demonstrates that atoms are cooled close to the ground state and may at most have small residual thermal excitation. When applying stabilization along x and y, we find an atom in the postselected region in 28 % of the cases, which is a more than 20-fold increase to before. The remaining limitation is the z-axis that cannot be actively stabilized. However, mechanical refocusing, i.e. (i) ramping down the intracavity trap, (ii) cooling atoms to the center of the

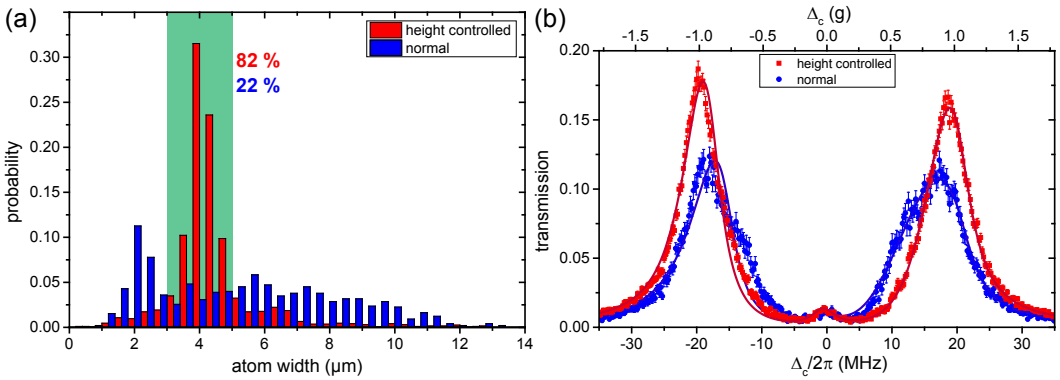

Figure 2.11.: Stabilization of the atom position in y-direction. Applying the same feedback used for the stabilization along x to the y-axis, also reduces the vertical distribution to a narrow region, as inferred from the atom width. Here, the postselection efficiency increases from 22 % to 82 %. In fact, with position control along x and postselection along z, the feedback causes an increase of the coupling strength from $g/2\pi = 17.8\,\mathrm{MHz}$ to 19.0 MHz.

transverse, red-detuned trap, and (iii) ramping the intracavity trap back up, has shown promising results and may be used in future experiments. Moreover, an optical tweezer, i.e. a tightly focused red-detuned dipole trap, could be implemented via the camera objective which would allow active positioning along z.

2.3. Atom Spectroscopy

Besides mastering the external DOFs, precise control of the atom's internal DOFs is the second mainstay to investigate feeble quantum effects and tame the ever-growing complexity of quantum optical experiments. Atom spectroscopy subsumes a number of techniques used to characterize the atom. While none of these has been newly developed within the context of this thesis, it is their first application to the described apparatus and they are of central importance, especially in Chapter 4. Consequently, we focus on the results meaningful for the later work rather than on a strict theoretical description.

High-fidelity discrimination, whether the atom resides in the $F = 1$ or $F = 2$ ground state, serves as a backbone to all spectroscopic techniques described here. We explore two potential schemes in Section 2.3.1. In Section 2.3.2, we use this hyperfine state detection for measuring the transition frequencies to the excited hyperfine states and, consequently, their light shifts induced by the traps. Finally, Raman spectroscopy induces transitions between Zeeman levels of the two ground states and reveals the atom's initial (prepared) state. It allows us to quantify the magnetic field at the atom's position and yields

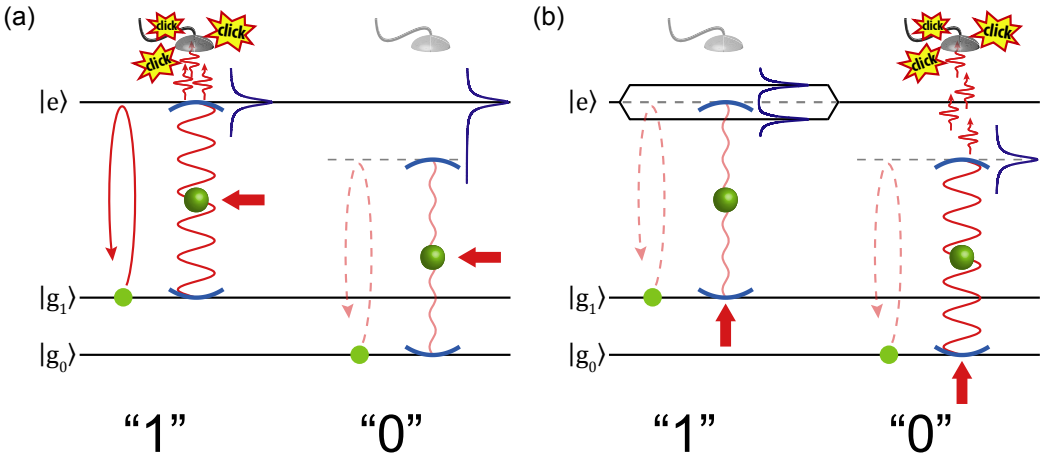

Figure 2.12.: Schemes for state detection. (a) For fluorescence state detection, a beam resonant to the $|g_1\rangle \leftrightarrow |e\rangle$ transition impinges from the side and is scattered onto the detector. Emission into that direction is enhanced by the cavity. (b) In case of state detection by differential transmission, the normal mode splitting switches the transmission of the empty cavity off when the atom resides in state $|g_1\rangle$. Atoms prepared in $|g_0\rangle$ and later detected in $|g_1\rangle$ ($|g_0\rangle$) count as “1” (“0”) to the transfer probability.

information on its temperature or mechanical state (Section 2.3.3). For future experiments, it provides opportunities to coherently prepare an exact Zeeman substate or a superposition of such.

2.3.1. State Detection

We pursue two different strategies to detect the hyperfine ground states. For now, we assume a simplified level scheme of only three states, two ground states $|g_0\rangle$ and $|g_1\rangle$ that we want to discriminate and an excited state $|e\rangle$.

The first scheme is based on detection of fluorescence light scattered by the atom [Fuh11] and was initially developed for free-space ion-trap experiments [Nag86, Ber86, Lei03]. When driving the atom with a beam resonant to the $|g_1\rangle \leftrightarrow |e\rangle$ transition, it scatters many photons at rate Γ_1 if it is in state $|g_1\rangle$ and remains unexcited if it is in state $|g_0\rangle$, since the latter is far detuned (Figure 2.12(a)). If the emission is monitored by a sensitive detector for a probing time T long enough to expect an average photon number $\overline{n}_1 = T \cdot \Gamma_1 \gg 1$, we can unambiguously discriminate state $|g_1\rangle$ from $|g_0\rangle$ within a single shot since $\overline{n}_0 = 0$ (neglecting dark counts and background light). To ensure that the atom scatters sufficiently many photons, $|e\rangle$ should dominantly decay into $|g_1\rangle$ as the atom will turn dark after decay into another ground state, e.g. $|g_0\rangle$ in our case. Since the rate for the latter remains finite in most experimental situations, a high detection efficiency is of utmost importance. The photon collection efficiency, however, typically remains poor since the

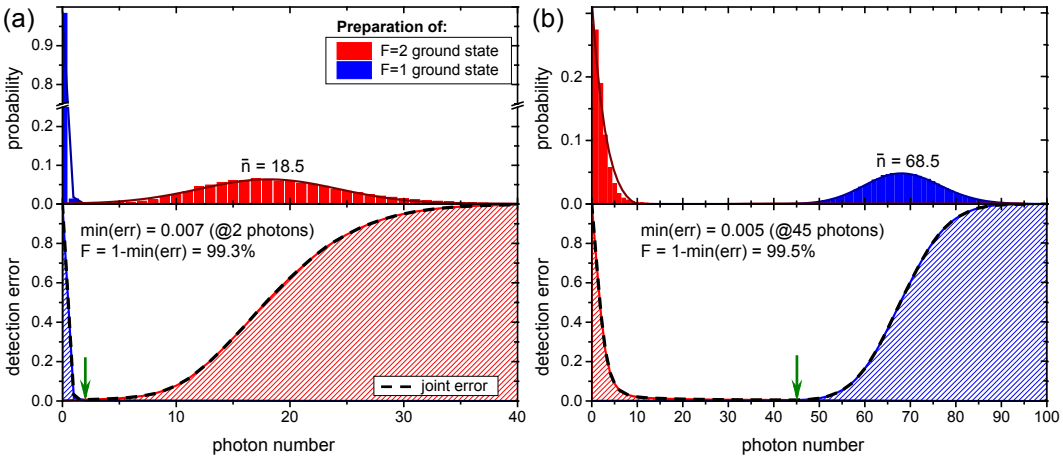

Figure 2.13.: Fidelities of state detection. The experimental distributions of detection events for preparation of either of the two ground states are clearly separated for both, (a) fluorescence detection and (b) differential transmission. The detection error quantifies the relative false detection when using the respective photon number as discrimination threshold. The maximum of both at each point yields the joint error, the minimum of which corresponds to the threshold with maximum detection fidelity, here 99.3 % and 99.5 %.

atom emits into a solid angle of 4π in free space. In our case, the cavity is resonant to the drive and significantly enhances emission into its mode. Scattered light is, thus, efficiently directed towards the detector. In contrast to traditional Purcell enhancement that boosts the irreversible emission into one specific mode, strong coupling causes coherent oscillations between atom and cavity such that excitation is evenly distributed between both and the chance to find the photon at the output of the cavity is naively expected to solely depend on the ratio of the dissipation rates: $\kappa/(\kappa+\gamma)$. Likewise, a fraction of $\gamma/(\kappa+\gamma)$ is emitted by the atom into free space.

The second scheme employs differential transmission of a probe resonantly driving the cavity that is strongly coupled to the $|g_1\rangle \leftrightarrow |e\rangle$ transition [Geh10]. Thus, already a single atom in $|g_1\rangle$ blocks photons from transiting through the system, while an atom in the uncoupled state $|g_0\rangle$ results in full transmission of an empty cavity, as depicted in Figure 2.12(b). The detection efficiency for this scheme is inherently high as we measure the photon number in the mode of the incident beam. The contrast between the bright and the dark state is given by $(1+g^2/(\kappa\gamma))^2$ which depends on the coupling strength [Kub10], as displayed in Figure 2.2(b). As a notable difference to the previous scheme, the atom remains practically unexcited in both cases since the light is either far detuned or cannot enter the cavity and is reflected at the input mirror. A comparison of both techniques is shown in Reference [Boc10].

In the experiment, we use the $F=1$ and $F=2$ hyperfine manifolds of the

ground state as $|g_0\rangle$ and $|g_1\rangle$, respectively. The excited state $|e\rangle$ is best implemented on the $F'' = 3$ manifold, since the coupling strength is maximal and the decay to $F = 1$ is dipole forbidden. The dominant depumping mechanism is expected to be off-resonant excitation of $F'' = 2$ and subsequent decay to $F = 1$. However, when resonantly driving the $|2\rangle \leftrightarrow |3''\rangle$ transition, $|2\rangle \leftrightarrow |2''\rangle$ is detuned by $\delta/2\pi = 267\,\mathrm{MHz}$ and consequently strongly suppressed by a factor of $(\delta/2\gamma_{D_2})^2 \approx 2000$. Another possible source is unwanted scattering from the dipole traps.

After the cooling interval, atoms start in a random ground state. Therefore, during the sequence, we need to first prepare a proper initial state. To this end, we use transverse beams that selectively drive atoms from one of the two hyperfine ground states to an excited state that has a finite probability to decay to the other ground state until all population has been transferred. By careful selection of the beam polarization and consideration of the Clebsch-Gordan coefficients of ^{87}Rb (Appendix A, Figure A.2), one can even prepare specific Zeeman substates with this simple method. We refer to it as incoherent state preparation. The atom is initiated in the $F = 1$ manifold by scattering photons from two pumps resonant to the $|2\rangle \leftrightarrow |1''\rangle$ and $|2\rangle \leftrightarrow |2''\rangle$ transitions until atoms starting in $F = 2$ have been pumped to $F = 1$. The ground state $F = 2$ can be prepared by depopulating $F = 1$ when driving the $|1\rangle \leftrightarrow |2'\rangle$ and $|1\rangle \leftrightarrow |2''\rangle$ transitions. This state preparation is typically followed by a spectroscopy interval during which a beam selectively transfers atoms to the other ground state. This is monitored in the subsequent state detection during which we collect the photons emitted from the cavity for a typical integration time of $T = 80\,\mu\mathrm{s}$ and decide via a preset threshold photon number whether the atom has been transferred ("1") or not ("0"). By averaging over many repetitions, we then find the transfer probability. The fidelity describes the probability to correctly discriminate the ground states, i.e. how well the photon distributions of the bright and dark state are separated.

In Figure 2.13, we show the measured photon distributions for preparing either of the ground states. As anticipated for fluorescence detection, we detect almost zero photons when the system is in the uncoupled $F = 1$ state, while the $F = 2$ yields a Poisson distribution with an average of $\overline{n} = 18.5$. The maximum $\overline{n}$ is limited by excessive heating of the atom due to the scattering of photons. It may be improved by working off-resonantly [Boc10]. However, the distributions are well separated and we find a fidelity for state detection of 99.3 % at a threshold of 2 photons. This includes errors due to imperfect state preparation. In case of differential transmission, the situation is reversed: An atom prepared in $F = 1$ leads to a high transmission at empty cavity resonance, that is suppressed for an atom in $F = 2$. Here, the dark state exhibits a higher count rate as the atom initially starts in a random Zeeman state of the $F = 2$ manifold whose coupling strengths vary from 5.1 MHz to 19.6 MHz causing relative transmissions as high as 3.5 %. As will be shown in Chapter 3, the

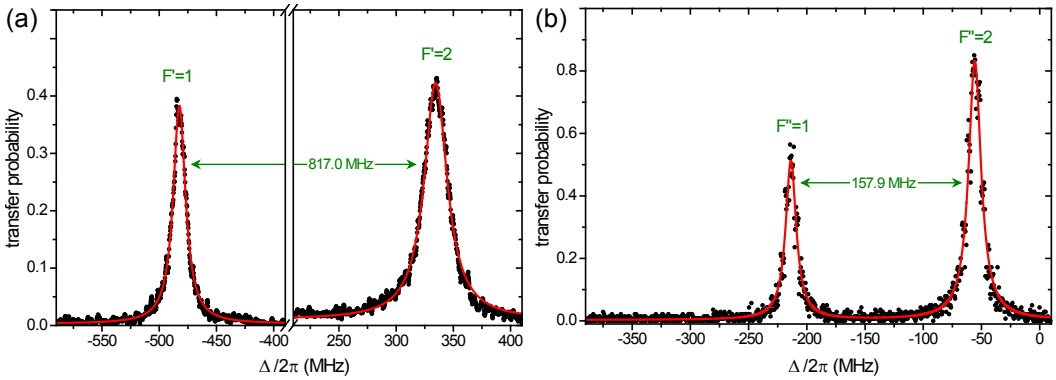

Figure 2.14.: Light shift spectroscopy. Spectroscopy of (a) D_1 transitions $|2\rangle \leftrightarrow |1'\rangle$ and $|2\rangle \leftrightarrow |2'\rangle$, and (b) D_2 transitions $|1\rangle \leftrightarrow |1''\rangle$ and $|1\rangle \leftrightarrow |2''\rangle$ reveals light shifts. Detunings correspond to the hyperfine splitting as in Appendix A, Figure A.1 and Reference [Ste03]. Red lines are Lorentz fits.

right-circular probe pumps the atom into the cycling transition within a few scattering events upon which the system is dark with a relative transmission of only 0.02 %. Since the atom remains mainly unexcited, we are not limited by heating and can go to much higher count rates for the bright state. In addition, it has a much better detection efficiency than fluorescence detection. Already at a mean photon number of $\overline{n} = 68.5$, this scheme outperforms the previous one with a detection fidelity of 99.5 % at a threshold of 45 photons. The qualitative disagreement to Reference [Boc10], who found fluorescence detection to be the favorable technique, is caused by the roughly fourfold larger coupling strength in our system. In the end, both techniques yield high fidelities and we choose differential transmission due to the lower heating rate.

2.3.2. Light Shift Spectroscopy

Spectroscopy is a technique to measure the transition frequencies from ground to electronically excited states such as the D lines for ^{87}Rb . While these are a priori known, any additional light shifts resulting from the dipole traps can be detected. Thus, one may find the exact frequency of a transition or monitor the induced Stark shift. The idea follows the concept of incoherent state preparation: starting in one of the ground states, the spectroscopy laser is ramped across the transition to an excited state that has a finite probability to decay to the other ground state. Only when the laser is resonant to the transition, atoms are transfered which is discerned during state detection.

In Figure 2.14(a) and (b), we display two different sample spectra on the D_1 and D_2 line, respectively. The detuning corresponds to the absolute hyperfine splitting [Ste03]. For Figure 2.14(a), the $F = 2$ ground state was prepared and the spectroscopy laser was tuned across both excited states on the D_1 line. We

find detunings of −482.4 MHz and +334.5 MHz and a splitting of 817.0 MHz. As a result, the red-detuned dipole trap shifts both transitions almost equally by about 26.7 MHz and 29.1 MHz[10].

On the D_2 line, the $F = 1$ was chosen as an initial state and the laser was swept almost across the full excited state manifold. Due to dipole selection rules, only the transitions $|1\rangle \leftrightarrow |1''\rangle$ at −213.7(1) MHz and $|1\rangle \leftrightarrow |2''\rangle$ at −55.7(1) MHz are observed. The $F'' = 0$ state expected about 72.2 MHz to the red of $F'' = 1$ is not coupled to the $F = 2$ ground state and therefore absent. When comparing these frequencies to the known detunings of −229.9 MHz and −72.9 MHz, we find an almost equal light shift for both of 16.2 MHz and 17.2 MHz, which is considerably lower than the one for the D_1 line. This is expected for a dipole trap which is closer in frequency to the latter transition.

2.3.3. Raman Spectroscopy

Having measured the light shifts of excited states, we also want to investigate the transitions between ground states. Electronic dipole transitions between these are forbidden. Microwave fields can transfer population between the two. However, their long wavelength results in a large focus and weak coupling to the atom. As a result, high power levels are required and transfer remains slow. In addition, it is difficult to achieve small directed microwave fields and metallic elements surrounding the cavity shield the atom. In a first test, microwaves caused disturbance to the cavity length stabilization. Therefore, we follow a different approach using stimulated Raman transitions via an auxiliary excited state which only requires two phase-stable optical fields. It is, thus, easily integrated into our setup using the existing optical axes and allows for fast coherent transfer between distinct Zeeman states of $F = 1$ and $F = 2$.

Principle. A pump beam impinging on a multilevel system experiences scattering by which photons are deflected from the incident field. In contrast to Rayleigh scattering that denotes elastic scattering where the state of the particle remains unchanged, Raman scattering refers to an inelastic process by which the energy of the scattered photon differs from the incident radiation as the particle transits to another state via spontaneous decay of an intermediate excited energy level [Ram28]. The effect has been observed in a variety of realizations for atoms, molecules, liquids and solid state systems. Another beam, the Stokes beam, coupling the excited state to the new ground state can turn the spontaneous decay into a stimulated emission process, thus preserving coherence. For this stimulated Raman transition both light fields must be coherent, phase-stable to each other and exhibit an energy difference that corresponds to the difference of the initial and final state. Together, they form a

[10]Note that during these measurements the trap was at 800 nm and at a lower power than described previously.

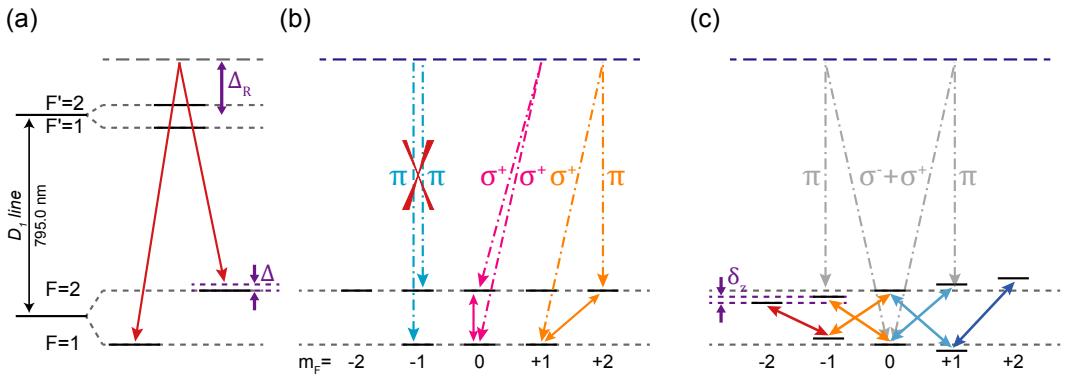

Figure 2.15.: Principles of Raman spectroscopy. (a) For stimulated Raman transfer, an atom absorbs a photon from one beam and emits it into the other beam in a stimulated process. The Raman pair needs to be phase-stable. In our case, it impinges transversally along x with linear orthogonal polarization, is detuned by about 0.2 THz to the D_1 line and derived from the same laser with one beam shifted with an electro-optic modulator by the ground state hyperfine splitting of 6.834 683 GHz. (b) The polarization of both beams yields the possible ground state transitions, some of which destructively interfere and may not be driven. (c) For our pair of π and $\sigma^+ + \sigma^-$, we find four non-degenerate transition frequencies with $\Delta m_F = \pm 1$ in the presence of a finite Zeeman shift δ_z.

so-called Λ-system as depicted in Figure 2.15(a). While we require a vanishing two-photon detuning Δ in order to coherently transfer population between the states, one avoids resonant excitation and subsequent spontaneous emission by choosing a one-photon detuning Δ_R to the excited state much larger than the decay rate γ, $\Delta_R \gg \gamma$. As the coherent transfer also works in reverse, one observes a population oscillation between the states known as Rabi flopping with a Rabi frequency Ω_R:

$$\Omega_R = \frac{\Omega_P \Omega_S}{\Delta_R} \tag{2.39}$$

where Ω_P and Ω_S are the driving strengths (Rabi frequencies) of the pump and Stokes beam. As the excited state remains unpopulated and in absence of dephasing, the transition width is solely given by $2\Omega_R$. Consequently, stimulated Raman transitions can be very narrow limited only by the ground state coherence and finite excitation probability.

Stimulated Raman transfer is a standard technique of the quantum optics toolbox for ultracold atom experiments and has been studied extensively, in theory and experiment [Lei03, Foo05, Boo08, Han13]. It was pioneered with ions in electrical traps [Hei90, Mon95], but has since then spread to a variety of experiments with neutral atoms [Kas91, Hen00, Rei14, Les14]. Its narrow linewidth makes it useful to investigate even small shifts of the ground states due to, e.g., magnetic fields or atomic motion in the trap. In the latter case,

ultracold atoms in deep dipole traps will no longer show classical oscillation but form discrete mechanical eigenstates of a quantized harmonic oscillator, the splitting of which corresponds to the trap frequency. Via stimulated Raman transitions, one can resolve these splittings on the order of hundreds of kHz. Using Raman sideband cooling [Ker00], it is possible to induce transitions between these states and thus step down the harmonic ladder to the lowest mechanical state referred to as motional ground state. Finally, stimulated Raman transfer is used to prepare specific Zeeman states and coherent superpositions of such [Ber98, Rei13].

To understand the state selectivity, we need to consider the polarizations of pump and Stokes beam. Several possible combinations are depicted in Figure 2.15(b). For any combination, one has to sum over all possible transitions, weighted by the Clebsch-Gordan coefficients (Appendix A, Figure A.2). This potentially leads to destructive interference as is the case for both beams in π-polarization. Thus, one can realize transitions between Zeeman states with $\Delta m_F = 0$, -1, $+1$ and ± 1. In the experiment, we choose a combination of two co-propagating transverse beams where one is polarized along the quantization axis driving π transitions and the other orthogonal to the first which causes $\sigma^+ + \sigma^-$ transitions (green arrow in Figure 2.3(a)). The corresponding change of the magnetic quantum number is $\Delta m_F = \pm 1$. All possible transitions are displayed in Figure 2.15(c). Theoretically, all of these transitions are degenerate. In practice, the earth magnetic field and, after compensation of that, our offset magnetic field lift this degeneracy via the linear Zeeman effect that describes the shift of atomic energy levels in a weak **B**-field. Analogously to the coupling of an electric dipole to an **E**-field in Equation (2.15), the interaction energy of a magnetic dipole with a magnetic field is simply given by $H_B = -\overrightarrow{\boldsymbol{\mu}}\mathbf{B}$. The electron orbiting the positive core, its spin and the spin of the nucleus all contribute to the magnetic dipole moment $\overrightarrow{\boldsymbol{\mu}}$ of an atom. In the perturbative regime, the shift of the Zeeman states of a manifold $\delta\mathcal{E}_Z$ is proportional to the magnetic quantum number for a magnetic field along the optical axis z:

$$\delta\mathcal{E}_Z = h\delta_Z = g_F \mu_B m_F B_0 \tag{2.40}$$

where the g-factor g_F relates the magnitude of the magnetic dipole moment for the specific fine- and hyperfine coupling of the state to the Bohr magneton $\mu_B = \frac{e\hbar}{2m_e}$ that serves as the natural unit of the electron magnetic moment. For the two hyperfine ground states $F = 1$ and $F = 2$ of ^{87}Rb , we find $g_F = -1/2$ and $+1/2$ which yields a corresponding Zeeman shift of $\delta_Z/B_0 = -0.7\,\mathrm{MHz/G}$ and $\delta_Z/B_0 = +0.7\,\mathrm{MHz/G}$, respectively.

As a consequence, we expect the transitions depicted in Figure 2.15(c) to separate into four frequencies at $\pm 1\delta_Z$ and $\pm 3\delta_Z$. In fact, the experimental Raman spectrum in Figure 2.16(a) with an offset magnetic field of about 0.6 G, i.e. $\delta_{Z,theo} = 0.42\,\mathrm{MHz}$, displays four prominent peaks with $\delta_Z = 428.6(18)\,\mathrm{kHz}$ and a center shift of $-42.9(41)\,\mathrm{kHz}$. The latter is a differential shift of the cen-

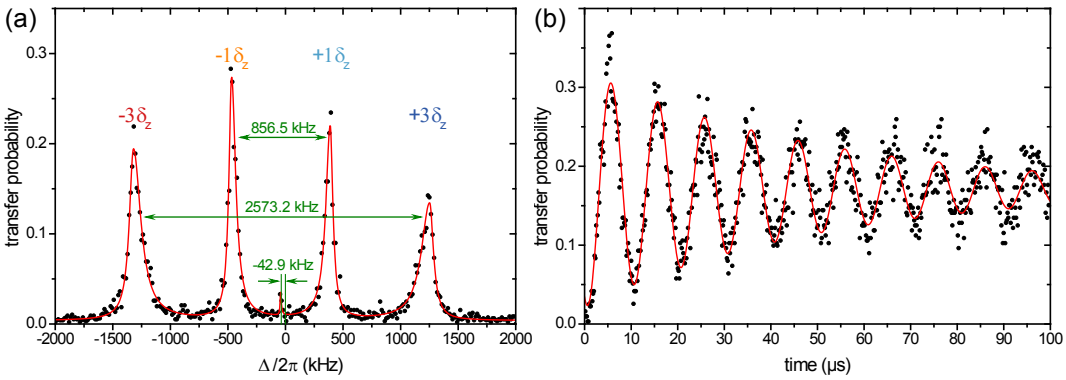

Figure 2.16.: Raman spectrum and Rabi oscillations. (a) The Raman spectrum versus two-photon detuning at an offset magnetic field along z of $+0.6\,\mathrm{G}$ displays the expected four peaks. The red solid line shows asymmetric Lorentz fits with different linewidths in each direction. (b) When $\Delta = -3\delta_Z$ and varying the duration of the Raman pulse, we observe Rabi oscillations between the two ground states with a $1/e$ coherence time of $51.2(21)\,\mu\mathrm{s}$, as found from an exponentially decaying sinusoidal fit (red line).

ter frequencies of the $F = 1$ and $F = 2$ states resulting from the red-detuned dipole trap that is sufficiently close in frequency to the D_1 line to resolve the atomic hyperfine structure of the ground states. The small feature close to zero detuning reflects the transition $|1, 0\rangle \leftrightarrow |2, 0\rangle$ caused by imperfect polarizations of the Raman beams. To demonstrate that the transfer is coherent, we show Rabi oscillations of the population of $|1, -1\rangle \leftrightarrow |2, -2\rangle$ at $-3\delta_Z$ in Figure 2.16(b) with a coherence time of $51.2(21)\,\mu\mathrm{s}$.

Magnetic Field Characterization. Next, we focus on the characterization of magnetic fields. Stray magnetic fields at the position of the atom can be caused by the earth's magnetic field or electronic devices such as transformers. Compensation of these background fields is achieved via three pairs of coils in Helmholtz configuration along the x-, y-, and z-direction. Such a pair induces a uniform axial magnetic field $B_i(I_i)$, $i = x, y, z$, if it carries a current of equal magnitude and direction. The strength of the total magnetic field is then given by:

$$B_0 = \sqrt{(\delta B_x + B_x(I_x))^2 + (\delta B_y + B_y(I_y))^2 + (\delta B_z + B_z(I_z))^2} \tag{2.41}$$

Here, δB_i is the stray magnetic field along $i = x, y, z$. For its characterization, we scan the field along each direction separately to find the zero-field current $I_{i,0}$ where $\delta B_i + B_i(I_{i,0}) = 0$.

The scans of the magnetic field in the radial directions y and x are depicted in Figure 2.17(a) and (b), respectively. Along y, we find a zero-field offset of $I_{y,0} =$

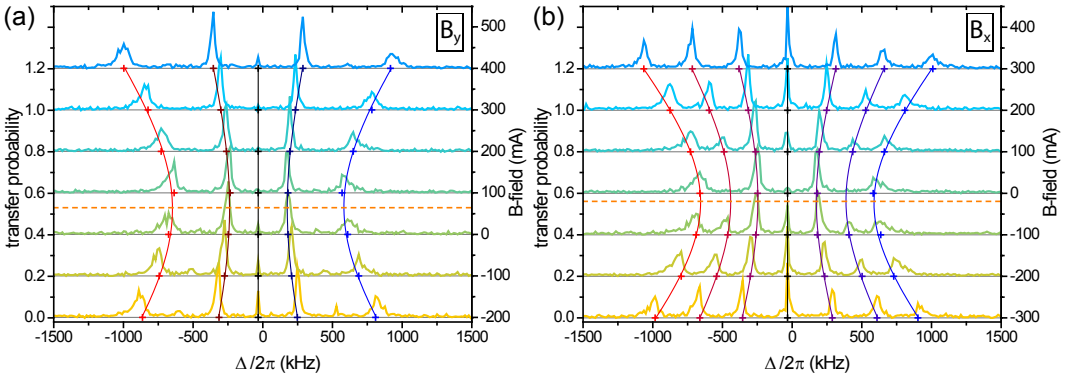

Figure 2.17.: Scans of radial magnetic fields. The Zeeman shift due to magnetic fields along (a) y and (b) x alters the Raman transition frequencies and yields zero-field offset currents of $+64\,\mathrm{mA}$ and $-19\,\mathrm{mA}$.

$+64\,\mathrm{mA}$ and observe the expected quadratic increase of the Zeeman shift for small deviations. From a fit of Equations (2.40) and (2.41), we deduce a shift of $0.73(1)\,\mathrm{MHz/A}$ which results in a gauging for our Helmholtz coils of $B_y(I_y) = 1.04(1)\,\mathrm{G/A}\cdot I_y$. When varying the B_x-field, we observe a similar behavior at an offset of $I_{x,0} = -19\,\mathrm{mA}$, a shift of $0.86(1)\,\mathrm{MHz/A}$ and $B_x(I_x) = 1.22(1)\,\mathrm{G/A}\cdot I_x$. However, in addition to the four original peaks, we get resonances at $0\delta_Z$ and $\pm 2\delta_Z$ when increasing the magnetic field along x. Increasing the magnetic field in a direction other than the cavity axis, will inevitably also rotate the quantization axis alongside. While changing B_y, the quantization axis moves in the y-z-plane spanned by the Raman beam polarizations which increasingly turns the π-polarized arm into $\sigma^+ + \sigma^-$ and the other from $\sigma^+ + \sigma^-$ into π, but will not affect the possible transitions. In contrast, B_x rotates the optical axis onto the direction of propagation in the x-z-plane. Then, $\sigma^+ + \sigma^-$ remains the same, but the π beam gets contributions from $\sigma^+ - \sigma^-$ which leads to transitions with $\Delta m_F = 0$ and consequently peaks at $0\delta_Z$ and $\pm 2\delta_Z$, transitions which are not present at zero offset field.

After compensation of δB_x and δB_y such that $\delta B_x + B_x(I_{x,0}) = 0$ and $\delta B_y + B_y(I_{y,0}) = 0$, we vary the magnetic field along z, as depicted in Figure 2.18(a). B_0 is now a linear function of B_z and all resonances cross at the zero-field offset of $I_{z,0} = +291\,\mathrm{mA}$. The slope yields $0.72\,\mathrm{MHz/A}$ and the gauging is $B_z(I_z) = 1.03\,\mathrm{G/A}\cdot I_z$. In Figure 2.18(b), we show the spectrum when $I_z = I_{z,0}$ and, thus, $B_0 = 0$. Consequently, the Zeeman substates are degenerate and all transitions collapse onto one peak. A Voigt profile yields a full width at half maximum of $123.2\,\mathrm{kHz}$ which shows good compensation and low decoherence. This will be important for the work on electromagnetically induced transparency in Chapter 4 that shares similarities with stimulated Raman transitions. However, considering a stimulated Raman pulse duration of $100\,\mu\mathrm{s}$, this is still above the expected Fourier limit of $10\,\mathrm{kHz}$. The residual

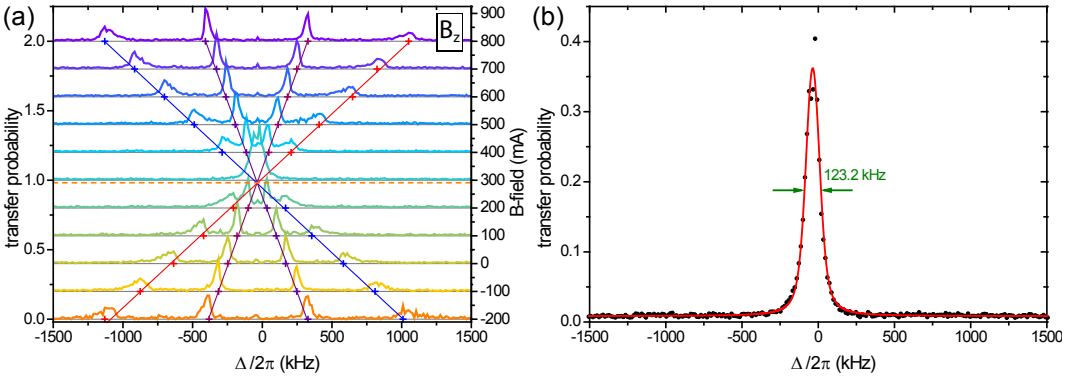

Figure 2.18.: Scan of magnetic field along the quantization axis. When compensating δB_x and δB_y, the Zeeman splitting becomes a linear function of B_z and resonances reach degeneracy at $I_{z,0} = +291\,\mathrm{mA}$.(b) A fit at this point with a Voigt profile yields best agreement to data and a linewidth of 123.2 kHz.

linewidth may be caused by magnetic field fluctuations. Considering that the width is likely limited by the $\pm 3\delta_Z$ transitions that react by three-fold larger shift in opposite directions to any variation of the magnetic field, this indicates a field fluctuation of $123.2\,\mathrm{kHz}/(2 \cdot 3 \cdot 0.7\,\mathrm{MHz/G}) = 29.3\,\mathrm{mG}$.

Altogether, a background magnetic field of about 0.3 G, as calculated via the offset currents, is in good agreement with the earth's magnetic field of 0.24 G to 0.64 G [Fin10]. In addition to compensation of the background field, we apply an offset magnetic field of 0.4 G to 0.6 G along the cavity axis z to define the quantization axis for most of the experiments reported in Chapters 3 and 4.

Trap Polarization and Vector Light Shifts. During these investigations, another effect was observed that can cause a broadening and asymmetry of the Raman resonances and may be used to measure the temperature of the atom. It has recently been described and explained in great detail in Reference [Neu15a], therefore we will keep it short here. Optical dipole traps with circular polarization induce a vector light shift which, similarly to the Zeeman effect, is linear in the magnetic quantum number. As a result, also the trap frequency and thus the splitting between the mechanical states depends on the Zeeman substate. Since we drive $\Delta m_F = \pm 1$ transitions with co-propagating beams that cannot change the mechanical state n_m, an atom will be transferred to another Zeeman state that may have a lower or higher spacing of the motional states and, consequently, experience a reduced or increased transition frequency:

$$\Delta(n_m) = (n_m + 1/2) \cdot (\nu_{t,f} - \nu_{t,i}) + (m_{F_f} g_{F_f} + m_{F_i} g_{F_i}) \cdot \mu_B B_0/h \qquad (2.42)$$

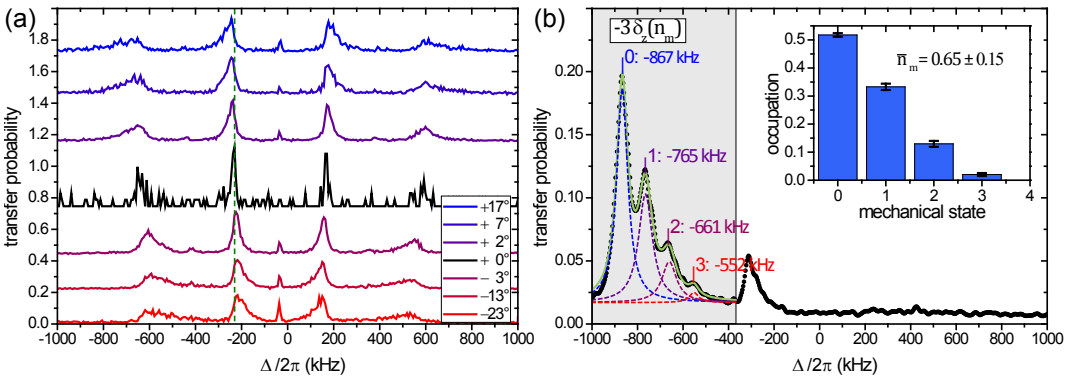

Figure 2.19.: Trap polarization and mechanical states. (a) Rotating a half-wave plate relative to a quarter-wave plate in the path of the intracavity trap yields circular components that cause vector light shifts enhancing or counteracting the Zeeman shift as a function of the mechanical state n_m. (b) These mechanical states are observed as peaks with a fixed splitting of 105.1(11) kHz in the $-3\delta_Z$-resonance when preparing the $|2,-2\rangle$, as described earlier. (Inset) Lorentzian fits yield the occupation of each state and an average mechanical state $\overline{n}_m = 0.65(15)$ close to the ground state.

where $\nu_{t,i}$ ($\nu_{t,f}$) is the trap frequency of the initial (final) state. We define the differential trap frequency $\delta\nu_t = \nu_{t,f} - \nu_{t,i}$. If the trap is σ^+ polarized, $\delta\nu_t$ is positive (negative) for $\Delta m_F = +1$ ($\Delta m_F = -1$) transitions. The resulting shift may then enhance or counteract the Zeeman shift.

In Figure 2.19(a), we show Raman spectra for varying polarization of the intracavity dipole trap that we change by rotating a quarter-wave plate. For a linear trap, the peaks seem symmetric. However, the cooling scheme does not work properly at this point [Neu15a] and data remains noisy. When deviating from the linear trap, we observe an asymmetry that broadens the resonances towards larger or smaller detunings depending on the trap polarization in agreement with our expectation. Figure 2.19(b) displays a spectrum for the peak at $-3\delta_Z$. One can clearly observe equally spaced peaks that correspond to the mechanical states where the low-frequency edge corresponds to the motional ground state $n_m = 0$. We deduce the occupation of each mechanical state and find an average phonon number of $\overline{n}_m = 0.65(15)$. Finally, this confirms that our cooling technique is capable of efficiently cooling atoms almost to the mechanical ground state.

3. One Mode Coupled to a Two-Level Atom: Two-Photon Blockade

This chapter deals with the effect of two-photon blockade in a two-level atom strongly coupled to a single cavity mode. The content has partially been published in [Ham17]:

C. Hamsen, K.N. Tolazzi, T. Wilk, and G. Rempe,
"Two-Photon Blockade in an Atom-Driven Cavity QED System",
Physical Review Letters **118**, 133604 (2017).

3.1. Introduction: Shrinking the Hilbert Space

An open driven quantum system exhibits fluctuations that reflect its walk through Hilbert space. These fluctuations are inherited by the leakage to the environment. More specifically in the case of discrete variables like particle number, the concept of quantum jumps, i.e. the sudden transition from one eigenstate to another by emission or absorption of one energy quantum, yields a direct link between the fluctuations of the system and its output [Ber86, Sau86]. This discontinuous evolution of the system is in stark contrast to the classically expected continuous trajectories and has been observed experimentally [Gle07]. However, by integrating over many repetitions or taking longtime averages, we recover the classically expected quantities, e.g. the mean number of particles or the lifetime of an eigenstate [Gue07]. The mean particle number will then be directly linked to its statistical fluctuation, i.e. the variance, via the Poisson distribution. Blocking parts of the Hilbert space can reduce these fluctuations and stabilize the output, which leads to statistics with a reduced variance that are, therefore, inherently quantum in nature. A blockade that sets an upper limit to the Hilbert space occurs when there is a sufficiently strong interaction between the involved quanta. Examples include the Coulomb force for electrons or the effective interaction between photons in an optically nonlinear medium. The latter has been used to realize single-photon blockade [Ima97] where $n = 1$ photons block further photons so that they are emitted one by one. This has been realized in various systems like a single atom in free space [Kim77], coupled to a macroscopic optical [Bir05a]

or microtoroid cavity [Day08], a transmon qubit in the electric field of a transmission line resonator [Lan11, Hof11] or quantum dots embedded in photonic crystal nanocavities [Far08, Rei12]. The next challenge is to scale the blockade to $n > 1$ photons [Sha10, Mir13, Car15] and produce a stream with at most n quanta. Such quantum scissors that truncate the Hilbert space could lead to novel applications in multi-photon quantum-nonlinear optics like an n-photon source [Cha14].

An ideal platform for the implementation of an optical n-photon blockade is cavity quantum electrodynamics (QED) which strongly couples a single two-level atom, perfectly blockaded at one photon, to a cavity that is completely unblocked. Both subsystems alone fail to show multi-photon blockade: the cavity needs the nonlinearity introduced by the atom, and the atom needs access to the larger Hilbert space provided by the cavity. Only the combined system with its anharmonic energy level structure provides the necessary photon-number dependent nonlinearity. Nevertheless, realization of multi-photon blockade is challenging due to the limited atom-cavity coupling strength that has so far been obtained [Vah03, Dev07, Sch08b]. Although strategies have been proposed to improve the blockade by extension to a three- or four-level atom involving electromagnetically induced transparency [Reb99, Sou13] or Raman scattering [Ros11, Ros15], multi-photon blockade has not been observed in optical systems. Its demonstration in circuit QED seems pending, too, although well-resolved multi-photon transitions have been investigated [Fin08, Dep08, Bis09].

In this chapter, we will explore two-photon blockade in a Jaynes-Cummings system with dissipation. We start with theoretical considerations in Section 3.2. First, we give a formal definition of n-photon blockade and derive practical conditions for experiments which culminate in two inequalities for the photon correlations of nth and $(n+1)$th order. Then, we focus on the physics of the atom-cavity system that allows for implementation of the two-photon blockade. We investigate how the driving of either atom or cavity affects the transition strengths between eigenstates. In Section 3.3, we discuss our experimental implementation of the proposed system. Section 3.4 gives the central experimental results. Firstly, we explore single-photon blockade for cavity and atom driving via second-order photon correlations. Secondly, we demonstrate two-photon blockade in this system via correlations of second- and third-order. Section 3.5 concludes this chapter and outlines future perspectives.

3.2. Theory

3.2.1. *n*-Photon Blockade

A system with one input and one output mode is said to exhibit n-photon blockade if the Hilbert space of its output unlike the input is restricted to

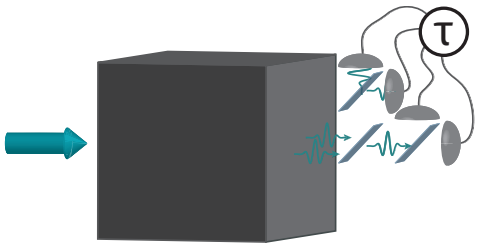

Figure 3.1.: Black box. The system is considered as a 'black box' with a coherent input field and an output channel. It is solely characterized by the photon statistics of the emitted light. These statistics are experimentally accessible via equal-time photon correlations.

states containing at most n quanta.

Within this section, we therefore treat the system as a 'black box' driven by a coherent input field [Bir05b] and characterized solely by the photon statistics of the emitted light (Figure 3.1). For simplicity, any further inputs, outputs or couplings to the environment are contained within that box. In case of an ideal n-photon blockade, the emission with mean photon number $\langle \hat{m} \rangle$ shows the following photon number distribution [Mir13]:

$$(i) \quad P(m) = 0 \text{ for } m > n \tag{3.1a}$$

$$(ii) \quad P(n) \neq 0 \tag{3.1b}$$

Furthermore, $P(m)$ has to still fulfill normalization, $\sum_{m=0}^{\infty} P(m) = 1$, which means that $\langle \hat{m} \rangle \leq n$. For $\langle \hat{m} \rangle = n$, the system even constitutes as an n-photon source. While the first condition (3.1a) reflects the fact that at most n photons are emitted at the same time, the second condition (3.1b) is set to exclude that the system is already $(n-1)$-photon blockaded. These two conditions can be translated into conditions for the normalized equal-time kth-order photon correlation that is better suited for experimental investigations since it does not suffer from e.g. low detection efficiencies. The correlations are linked to the distribution via:

$$g^{(k)}(\tau = \mathbf{0}) = \frac{G^{(k)}(\mathbf{0})}{\langle \hat{m} \rangle^k} = \frac{1}{\langle \hat{m} \rangle^k} \sum_{m=k}^{\infty} \frac{m!}{(m-k)!} P(m) \tag{3.2}$$

In order to verify if a system is n-photon blockaded, the correlations of the emitted light field then have to fulfill the following conditions:

$$(i) \quad g^{(n+1)}(\mathbf{0}) = 0 \tag{3.3a}$$

$$(ii) \quad g^{(n)}(\mathbf{0}) \neq 0 \tag{3.3b}$$

These strict conditions are only fulfilled for a perfectly blockaded system, which is hard to achieve in experiments. If the n-photon blockade does not work perfectly, we expect that $P(m) \neq 0$ even for $m > n$, but that the probability to get more than n photons is suppressed compared to a Poisson distributed light field $\mathcal{P}(m) = \langle \hat{m} \rangle^m e^{-\langle \hat{m} \rangle}/m!$ with the same average photon number $\langle \hat{m} \rangle$

as the emitted field. We use the Poisson distribution as a reference since it describes the probability of recording a given number of clicks in a fixed time interval for a known average photon number in case of perfectly uncorrelated photons. As a result, the two conditions in Equations (3.1a) and (3.1b) when reformulated for an imperfect blockade become:

$$(i) \quad P(m) < \mathcal{P}(m) \text{ for } m > n \tag{3.4a}$$

$$(ii) \quad P(n) \geq \mathcal{P}(n) \tag{3.4b}$$

Again, the first condition ensures that all photon numbers above n are suppressed, and the second condition ensures that this is not yet the case for $(n-1)$ photons. In this case, each kth-order correlation, and consequently the respective condition as well, depends in general on all higher probabilities of the photon distribution since Equation (3.2) contains an infinite sum. It only simplified to Equations (3.3a) and (3.3b) since all elements $m > n$ were 0. However, if we assume a small mean photon number $\langle \hat{m} \rangle \ll 1$, and a distribution that is sufficiently well-behaved fulfilling $P(m) \gg P(m+1)$, then it is sufficient to only consider probabilities up to $(n+1)$th order. In consequence, it suffices to demonstrate that Equation (3.4a) holds for $m = n+1$ and $P(n+1)$ can again be given in terms of the correlation function $g^{(n+1)}(\mathbf{0})$. The condition then reads:

$$\begin{aligned} P(n+1) &= \frac{\langle \hat{m} \rangle^{(n+1)}}{(n+1)!} \cdot g^{(n+1)}(\mathbf{0}) \\ &< \mathcal{P}(n+1) = \frac{\langle \hat{m} \rangle^{(n+1)}}{(n+1)!} \cdot e^{-\langle \hat{m} \rangle}, \end{aligned} \tag{3.5}$$

This can be simplified using the Taylor expansion for $e^{-\langle \hat{m} \rangle}$:

$$g^{(n+1)}(\mathbf{0}) < 1 - \frac{\langle \hat{m} \rangle}{1!} + \frac{\langle \hat{m} \rangle^2}{2!} - \frac{\langle \hat{m} \rangle^3}{3!} + ... \tag{3.6}$$

Since $\langle \hat{m} \rangle \ll 1$, we find a lower bound for which the condition formulated in Equation (3.4a) always holds:

$$g^{(n+1)}(\mathbf{0}) < 1 - \langle \hat{m} \rangle \tag{3.7}$$

For the second condition given in Equation (3.4b), we can also find a reformulation in terms of correlation functions under the same restrictions as Equation (3.7) was derived:

$$\begin{aligned} P(n) = \frac{\langle \hat{m} \rangle^n}{n!} \cdot g^{(n)}(\mathbf{0}) - \frac{\langle \hat{m} \rangle^{(n+1)}}{n!} \cdot g^{(n+1)}(\mathbf{0}) \\ \geq \mathcal{P}(n) = \frac{\langle \hat{m} \rangle^n}{n!} \cdot e^{-\langle \hat{m} \rangle} \end{aligned} \tag{3.8}$$

When inserting the upper limit $g^{(n+1)}(\mathbf{0}) = 1 - \langle \hat{m} \rangle$ from Equation (3.7) into the inequality, this reduces to:

$$g^{(n)}(\mathbf{0}) \geq 1 - \frac{\langle \hat{m} \rangle^2}{2} \tag{3.9}$$

Again, if this stricter condition is met, Equation (3.4b) is fulfilled, too. In summary, we therefore find for an imperfect n-photon blockade:

$$(i) \quad g^{(n+1)}(\mathbf{0}) < 1 - \langle \hat{m} \rangle \approx 1 \tag{3.10a}$$

$$(ii) \quad g^{(n)}(\mathbf{0}) \geq 1 - \frac{\langle \hat{m} \rangle^2}{2} \approx 1 \tag{3.10b}$$

The last approximation often holds in our experiments since the terms of $\langle \hat{m} \rangle$ or $\langle \hat{m} \rangle^2$ remain below the error bars.

Now, we have found two conditions for the photon correlations of nth and $(n+1)$th order that allow us to determine whether a system exhibits n-photon blockade. Typically, the restriction $\langle \hat{m} \rangle \ll 1$ is fulfilled in experiments since the truncation at n photons is only achieved in systems that exhibit a sufficiently strong nonlinearity and are therefore inherently hard to excite. On the other hand, this prolongs measurement time for correlations of high orders that rely on coincidence of multiple photons. Photon correlations up to third order have been demonstrated in systems consisting of atoms and optical cavities [Koc11b], and even up to fourth order with quantum dots in microcavities with three orders of magnitude higher decay and count rates [Run14]. From that point of view, at least single- and two-photon blockade should be within experimental reach in our system.

While showing that $g^{(2)}(0) < 1$ is sufficient for single-photon blockade[1], in order to prove a two-photon blockade, it is necessary to fulfill Equations (3.10a) and (3.10b) for $n = 2$, which yields:

$$(i) \quad g^{(3)}(\mathbf{0}) < 1 \tag{3.11a}$$

$$(ii) \quad g^{(2)}(\mathbf{0}) \geq 1. \tag{3.11b}$$

Note that this derivation was done for a comparison of the output light field with a light field following Poissonian statistics for which all orders of normalized photon correlations are equal to one, which corresponds to the level of uncorrelated photons.

3.2.2. Atom Driven versus Cavity Driven System

In the previous section, we have given a definition of n-photon blockade that is solely based on the statistics of the emitted light and found conditions for the

[1] Condition (3.4b) must be fulfilled if condition (3.4a) is met and $\langle \hat{m} \rangle$ is to remain the same.

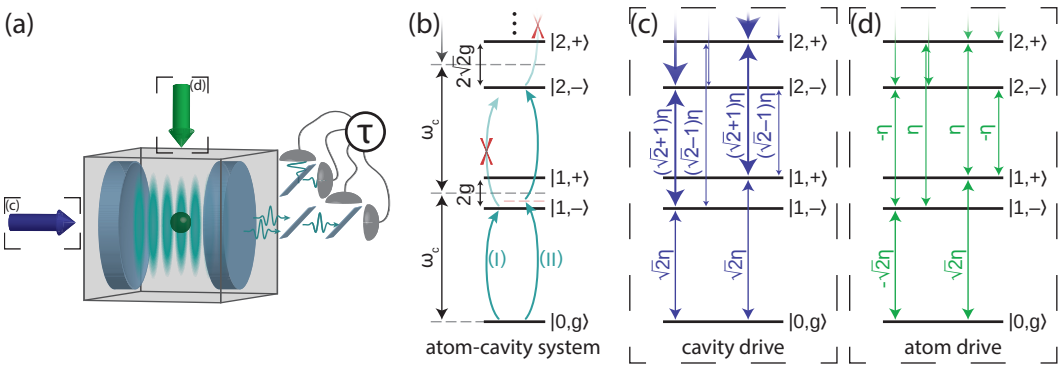

Figure 3.2.: Energy ladder and effective driving strengths. A sketch of the experimental setup and physical system inside the 'black box' is revealed. As depicted in (a), a single atom is trapped at the antinode of an intracavity light field. The anharmonic energy-ladder system (b) can either be excited via a cavity (blue, effective driving strengths see (c)) or atom drive (green, effective driving strengths see (d)). The resulting cavity field is then monitored via an extended Hanbury Brown and Twiss detection setup.

nth- and $(n+1)$th-order photon correlation which can be tested experimentally. The physical system was, however, treated as a 'black box'. The question arises: What kind of system has to be enclosed in that box? Several practical requirements follow naturally from the simple idea of an n-photon blockade as a truncation of the Hilbert space. Firstly, such a system must be able to store at least n excitations at once. Secondly, to access $n > 1$ quanta stored in the system, a decay channel should be capable of releasing multiple excitations inside the system to the outside world simultaneously. Finally, truncation at n excitations requires some kind of n-photon nonlinearity such that further absorption to $(n + 1)$ excitations is suppressed. The two-level atom strongly-coupled to a cavity, as described in Section 2.1, exhibits such an n-photon nonlinearity in form of an anharmonic energy ladder of doublets split by $2\sqrt{n}g$ (Figure 3.2(a) and (b)). For resonant excitation of the first (I) or second (II) manifold, the drive is detuned to higher lying eigenstates and we expect single- or two-photon blockade. However, while it seems unimportant which component, cavity or atom, we use to excite the system, only the cavity can emit multiple photons at once.

The simple argumentation solely focusing on the anharmonicity of the energy ladder is insufficient since we also have to take the transition strengths between the eigenstates into account. These transition strengths depend on whether we drive the atom or cavity and become specifically important if the coupling strength is limited compared to the decay rates of the system such that considerable overlap with higher manifolds is expected.

As derived in Section 2.1, the CQED system is well described by the Hamil-

tonian:

$$\hat{\mathcal{H}} = \hbar\Delta_a\,\hat{\sigma}^\dagger\hat{\sigma} + \hbar\Delta_c\,\hat{a}^\dagger\hat{a} + \hbar g\,(\hat{a}^\dagger\hat{\sigma} + \hat{\sigma}^\dagger\hat{a}) + \hat{\mathcal{H}}_d \tag{3.12}$$

The last term describes the excitation via the driving field. The energy structure remains unaffected as long as the drive strength is much smaller than g and does not exceed the atomic polarization decay rate γ and cavity-field decay rate κ [Als92, Bis09, Koc11b]. However, the corresponding excitation strengths between different manifolds differ whether the cavity is driven, $\hat{\mathcal{H}}_d = \hbar\eta_c\,(\hat{a}+\hat{a}^\dagger)$, or the atom, $\hat{\mathcal{H}}_d = \hbar\eta_a\,(\hat{\sigma}+\hat{\sigma}^\dagger)$ [Als91]. Here, η_c (η_a) is the strength of the cavity (atom) drive. Both strengths are expressed in terms of bare eigenstates of the system without atom-cavity interaction. We can reformulate these in the dressed state basis of the coupled system ($|n,\pm\rangle$). For the case of cavity driving, we find [Car09, Koc11a]:

$$\begin{aligned}
\hat{\mathcal{H}}_d &= \hbar\eta_c\left(\hat{a}+\hat{a}^\dagger\right)\\
&= \hbar\eta_c\sum_{n=0}^{\infty}\left(\sqrt{n+1}\,|n+1\rangle\langle n| + \text{h.c.}\right)\otimes\left(|g\rangle\langle g|\,|e\rangle\langle e|\right)\\
&= \hbar\eta_c\sum_{n=1}^{\infty}\Big(\frac{\sqrt{n+1}+\sqrt{n}}{2}\left(|n+1,+\rangle\langle n,+| + |n+1,-\rangle\langle n,-|\right)\\
&\qquad + \frac{\sqrt{n+1}-\sqrt{n}}{2}\left(|n+1,-\rangle\langle n,+| + |n+1,+\rangle\langle n,-|\right)\\
&\qquad + \frac{\sqrt{2}}{2}\left(|1,-\rangle\langle 0,g| + |1,+\rangle\langle 0,g|\right) + \text{h.c.}\Big)
\end{aligned} \tag{3.13}$$

This reformulation yields effective driving strengths $\widetilde{\eta}_c/2$ that are depicted schematically in Figure 3.2(c). For the transition from the ground state to the first manifold, $|0,g\rangle \rightarrow |1,\pm\rangle$, these are $\widetilde{\eta}_c = \sqrt{2}\eta_c$. For the transition from the nth to the $(n+1)$th manifold, bosonic bunching causes symmetry conserving transitions, ($|n,\pm\rangle \rightarrow |n+1,\pm\rangle$), to be strongly enhanced by $\widetilde{\eta}_c = (\sqrt{n+1}+\sqrt{n})\eta_c$ whereas those that change symmetry, ($|n,\pm\rangle \rightarrow |n+1,\mp\rangle$), are suppressed, $\widetilde{\eta}_c = (\sqrt{n+1}-\sqrt{n})\eta_c$. For small atom decay rates, this can effectively split the energy ladder of doublets into two separate ladders.

Reformulating the driving term for excitation of the atom gives a different result:

$$\begin{aligned}
\hat{\mathcal{H}}_d &= \hbar\eta_a\left(\hat{\sigma}+\hat{\sigma}^\dagger\right) = \hbar\eta_a\left(|g\rangle\langle e| + |e\rangle\langle g|\right)\otimes\sum_{n=0}^{\infty}|n\rangle\langle n|\\
&= \hbar\eta_a\Bigg(\frac{\sqrt{2}}{2}\left(|1,+\rangle\langle 0,g| - |1,-\rangle\langle 0,g|\right)\\
&\qquad + \sum_{n=1}^{\infty}\frac{1}{2}\left(|n+1,+\rangle\langle n,+| + |n+1,+\rangle\langle n,-|\right)\\
&\qquad - \sum_{n=1}^{\infty}\frac{1}{2}\left(|n+1,-\rangle\langle n,+| + |n+1,-\rangle\langle n,-|\right) + \text{h.c.}\Bigg)
\end{aligned} \tag{3.14}$$

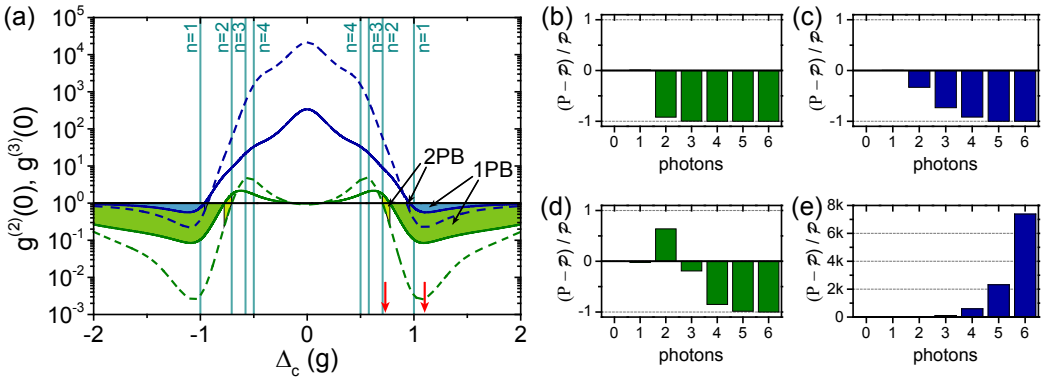

Figure 3.3.: Simulated photon correlations and statistics. (a) Simulated second- (solid) and third-order (dashed) equal-time photon correlations versus probe-cavity detuning Δ_c are depicted in units of coupling strength for atom (green) and cavity driving (blue). Vertical lines indicate the nth manifold and red arrows show the detunings chosen for the distributions. Filled areas indicate regions of single- (1PB) or two-photon blockade (2PB) as described by Equations (3.10a) and (3.10b). The relative deviations of the simulated photon distributions to Poisson distributions of the same mean photon number are shown for atom (b),(d) and cavity (c),(e) excitation at the first (b),(c) and second (d),(e) manifold. The parameters correspond to those used in the experiment (Section 3.4). In (e), the ordinate is scaled by a factor of $k = 1000$.

Again, we find effective strengths $\widetilde{\eta}_a/2$ shown in Figure 3.2(d). While the transition from the ground state to the first manifold remains the same $\widetilde{\eta}_a = \pm\sqrt{2}\eta_a$, all other transitions have equal strengths, with the sign being that of the upper state, $\widetilde{\eta}_a = \pm\eta_a$.

As a consequence, resonant driving of the nth manifold via the cavity diminishes the structural suppression of higher excitations since the corresponding transition strengths increase. In contrast, the transition strengths remain constant when driving the atom instead. To understand the consequences for single- and two-photon blockade, we show simulations of the second- and third-order equal-time photon correlation function in Figure 3.3(a). The stronger suppression of higher rungs for atom excitation manifests itself in a broad range of detunings and an improved purity of single-photon emission on the first manifold [Bir05b]. This is confirmed by simulations of the photon distributions shown in Figure 3.3(b) and (c). We find that the two-photon and higher components are more strongly suppressed for atom than for cavity driving.

Figure 3.3(d) and (e) depict the distributions for excitation close to the second manifold. The bosonic bunching dominates for cavity driving and the population grows with increasing photon number relative to the Poisson distribution. For atom excitation, we observe two-photon blockade as the two-photon component is enhanced while all higher probabilities are suppressed.

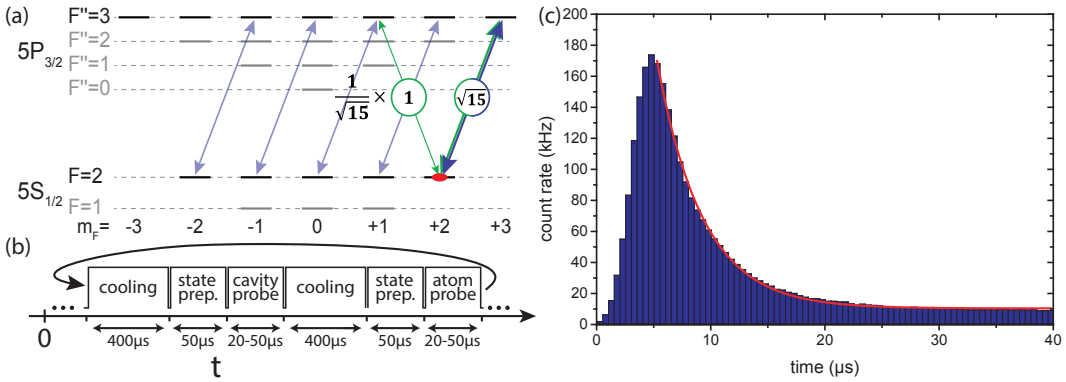

Figure 3.4.: Driving scheme and sequence. (a) The driving scheme is illustrated for atom (green) and cavity drive (blue). The σ^+ pump during state preparation (light blue) populates the $F = 2$, $m_F = +2$ ground state. Due to the large difference in Clebsch-Gordan coefficients, the linear transverse probe experiences an almost two-level-system. (b) Measurement sequence used during the experiment (see Figure 2.4 for full sequence). (c) Transmission during state preparation exhibits a steep increase due to the turn on behavior of the probe and falls off after 5 µs with a decay constant of 4 µs as the atom is prepared in the $|2, +2\rangle$.

The effect, however, remains weak for three photons. It is dependent on the driving strength and limited to a small range in frequency (Figure 3.3(a)).

Altogether, the comparison of photon correlations with distributions complements our previous derivation in Section 3.2.1.

3.3. Experimental Implementation

For this experiment, the high-finesse Fabry-Pérot resonator is adjusted to a cavity length of only 202 µm in order to maximize the coupling strength ($g \propto L^{-\frac{3}{4}}$). This yields a field decay rate of $\kappa/2\pi = 2.0\,\mathrm{MHz}$. We work with ^{87}Rb atoms on the D_2 line at 780 nm that exhibit a polarization decay rate of $\gamma/2\pi = 3.0\,\mathrm{MHz}$. The ac Stark shift, mainly caused by the red-detuned standing-wave dipole trap set to 800 nm, compensates the bare atom-cavity detuning of $-15.2\,\mathrm{MHz}$ to the $F = 2 \leftrightarrow F'' = 3$ transition to only a few MHz. For the largest dipole matrix element between the Zeeman states $|2, +2\rangle \leftrightarrow |3'', +3\rangle$ (Figure 3.4(a)), a theoretical atom-cavity coupling constant of $g/2\pi = 19.6\,\mathrm{MHz}$ puts us well into the strong-coupling regime of CQED, $g \gg (\kappa, \gamma)$. The quantization axis is defined parallel to the cavity axis by an offset magnetic field along the z-direction of about 0.4 G.

By the time of the experiment, the algorithm for the full 3D microscopy of atoms was not yet in place. Only positioning along the x-direction and postselection on the cavity axis were implemented leaving the vertical axis

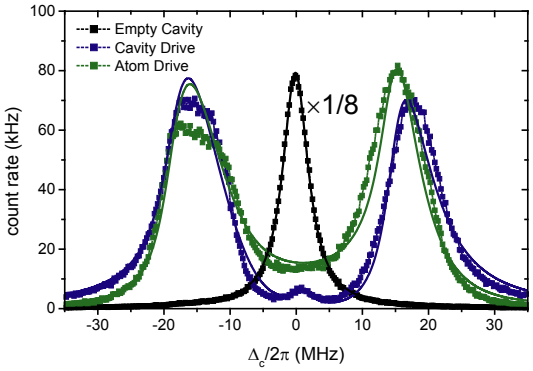

Figure 3.5.: Atom and cavity driven normal mode spectra. Spectra measured for the uncoupled (black, scaled by factor 1/8) and strongly-coupled (blue) cavity driven system in comparison to exciting the atom (green) are depicted. The thick colored lines are fits of a model considering residual thermal excitation and remnants of the empty cavity for the coupled spectra in case of cavity driving as described in Appendix B.

uncontrolled. Fluctuations in width of the atom images, however, indicate a significant distribution along this direction on the order of the cavity waist. This is considered the main experimental imperfection and led to the development of the atomic side-of-fringe lock, as described in Section 2.2.2.

While the atom is trapped, we repeat our measurement sequence as depicted in Figure 3.4(b) with a rate of 2 kHz alternating between cavity and atom driving. We start with a cooling interval of 400 µs followed by 50 µs of state preparation. Here, we pump the atom to the $|2,+2\rangle$ ground state by applying a circularly polarized, resonant cavity probe that drives σ^+ transitions (light blue arrows in Figure 3.4(a)). As the respective Clebsch-Gordan coefficients increase towards the final state, excitation will be increasingly suppressed (Figure 3.4(c)) due to a growing normal mode splitting. This ensures rapid state preparation with a strong drive while at the same time avoiding excessive heating. We finish with the probe interval during which either the cavity or the atom drive excites the system at the desired frequency. We record the transmitted signal on four single-photon detectors in a Hanbury Brown and Twiss-type configuration with a timing resolution of 1 ns. Depumping and heating effects are minimized by keeping this interval short (20 µs to 50 µs), especially in case of higher driving strengths. While the cavity probe drives only σ^+ transitions, we excite the atom with a linearly polarized transverse probe that drives σ^+ and σ^- transitions. Since the dipole matrix element for the σ^- transition is much weaker, we expect a quasi two-level behavior. However, depumping and coherent admixtures of other transitions cannot be fully neglected and may affect the observed coupling strength, especially close to the second manifold where these have their strongest contributions due to the smaller splitting.

Finally, the power is chosen such that we remain in the weak driving regime, $\eta_{a,c} \leq (\kappa, \gamma)$. During the whole time, a weak transverse beam resonant to the $F = 1 \leftrightarrow F' = 2$ transition on the D_1 line at 795 nm repumps atoms that end up in the $F = 1$ ground state due to off-resonant scattering.

Spectra for atom and cavity driving are depicted in Figure 3.5. The distinct splitting of the normal modes reflects the strong coupling of the system in both cases. We deduce an experimental coupling constant of $g/2\pi = 16.38(4)$ MHz. The finite temperature and position distribution of the atoms causes a notable broadening of the red-detuned normal mode that is more strongly affected as its character is more atom-like due to a residual detuning between atom and cavity [Sch08a]. The stronger drop of transmission around zero detuning in case of cavity driving results from the atomic antiresonance caused by destructive interference when exciting the cavity [Sam14]. This also slightly increases the observed normal mode splitting. The small peak at $\Delta_c = 0$ MHz when exciting the resonator is identified as remnants of the empty cavity due to imperfect polarization of the transmitted light resulting from birefringence. The effect amounts to about 1 % and can be suppressed by polarization filtering.

3.4. Results

In this section, we first explore the effect of the drive on the first manifold via single-photon blockade and demonstrate two-photon blockade in a second step. For the latter case, we discuss the complex dynamics of the third-order photon correlations.

3.4.1. Single-Photon Blockade

In order to show single-photon blockade, we have to measure the time-dependent second-order photon correlation $g^{(2)}(\tau) = \langle \hat{n} \cdot \hat{n}(\tau) \rangle / \langle \hat{n} \rangle^2$ (normal and time ordered) and demonstrate that $g^{(2)}(0) < 1$ (Section 3.2.1). As proposed in Section 3.2.2, we excite the system close to the first manifold via the atom or the cavity to confirm its dependence on the driven component. For atom driving, we excite the system with a strength of $\eta_a/2\pi \approx 0.55$ MHz which yields a mean photon number $\langle \hat{m} \rangle \approx 0.01$ inside the cavity. The resulting correlation shown in Figure 3.6(a) is in good qualitative agreement with the corresponding theory that is depicted as an inset. A strong sub-Poissonian antibunching with a $g^{(2)}(0) = 0.16(1)$ and a rising slope indicate emission of single light quanta due to a strong blockade of multiple excitations (compare Figure 3.2(b,I)). We observe a small and rapid oscillation at approximately twice the coupling rate g known as vacuum Rabi oscillation [Rem91]. It originates from the coherent energy exchange between atom and cavity. Since the $g^{(2)}(\tau)$ is conditioned on detection of a photon, and the respective probability is higher when all

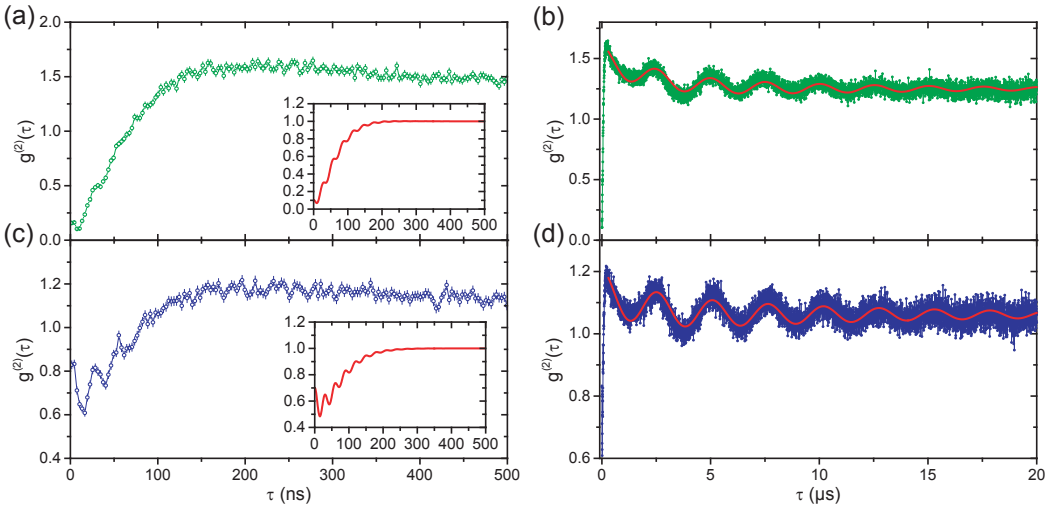

Figure 3.6.: Photon correlations at one-photon resonance. The second-order photon correlation function for atom (a),(b) and cavity (c),(d) excitation of the first manifold at $\Delta_c/2\pi = 18\,\mathrm{MHz}$ is depicted with a binning of 3 ns. The behavior at short time delays between the photons reveals single-photon blockade. The theory (insets) is calculated from numerical solution of the master equation and serves as qualitative comparison. Deviations to experimental results stem from atomic motion and position distribution of atoms within the cavity mode as can be seen in the long time behavior shown in (b) and (d). From the fit of an oscillating function (red solid lines) we deduce a frequency of about 395 kHz in good agreement with the expectation for our axial trap frequency. In addition, we find a finite offset from one even after decay of the trap dynamics for $\tau > 15\,\mu\mathrm{s}$.

excitation is predominantly in the cavity, the oscillation always starts with a local maximum for $\tau = 0\,\mathrm{ns}$. In order to observe this coherent evolution, the system must therefore be at least doubly excited. In other words, the amplitude of the oscillation depends on the amount of population in the second manifold and, thus, decreases with increasing single-photon blockade. We estimate the coupling rate from the second oscillation maximum at 31.5(15) ns to be 15.9(8) MHz which is in good agreement with the fitted value from the spectrum.

Excitation of the cavity ($\eta_c/2\pi \approx 0.55\,\mathrm{MHz}$, $\langle\hat{m}\rangle \approx 0.01$) on the first manifold is depicted in Figure 3.6(c) and yields qualitatively the same behavior. However, the value $g^{(2)}(0) = 0.83(2)$ is much larger, and stronger vacuum Rabi oscillations indicate significant excitation of higher manifolds. In accordance with theory, atom driving does exhibit a far stronger photon blockade effect despite the same energy level structure. For cavity excitation, the second oscillation maximum occurs at 28.5(15) ns which corresponds to a coupling rate of 17.5(9) MHz.

In both cases, the non-classical behavior disappears on a timescale deter-

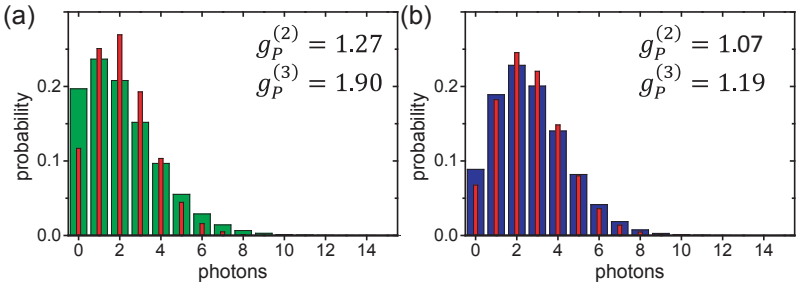

Figure 3.7.: Photon distributions of the probe intervals at one-photon resonance. The photon distribution $P(n)$ per probe interval is shown for (a) atom and (b) cavity excitation. These distributions are used to calculate the expected values for a second- and third-order photon correlation of a given light field. The deviation in average photon number is caused by the different spectral intensities. The red bars show a Poisson distribution of the same mean photon number.

mined by the decay rate of the excited dressed states $(\frac{\kappa+\gamma}{2})^{-1} \approx 64\,\text{ns}$. Beyond this time, the correlations are expected to approach 1, the value expected for independent photons as described by a Poisson distribution. In the experiment, both correlations deviate from 1 due to atomic motion and residual displacement from the cavity-mode center and excitation beam [Rem91]. As described in Section 3.3, the position distribution is caused by the loading and trapping scheme for atoms while motion results from finite temperatures after cooling and heating due to the resonant probe beams. Both effects are observed in correlations. In Figure 3.6(b) and (d) we show the second-order correlations on the first manifold for atom and cavity driving for time delays up to 20 µs. We observe how the pronounced antibunching feature at $\tau = 0$ and the quantum dynamics of the system settle to a peak resulting from technical fluctuations. The major contribution of this bunching peak comes from an oscillation of about 395 kHz that agrees well with twice the atomic trap frequency along the cavity axis determined by the blue-detuned intracavity dipole trap [Die87, Rot08]. The transverse trap frequencies are on the same order, but only excursions along the standing wave of the cavity will cause a significant modulation of the coupling constant which in turn will cause a 'breathing' of the normal modes. Consequently, the shape and amplitude of the resulting intensity modulation strongly depends on the driving frequency. The correlations are taken close to the maximum of the normal modes at the outside slope and are therefore prone to show strong motion artifacts. In addition, motion along all trap axes leads to varying atom-cavity detunings. The motion changes the overlap with the optical dipole traps which in turn affects the corresponding light shift from the dynamical Stark effect. We expect the resulting background to be incoherent as the variations happen at different frequencies and lack phase stability relative to each other.

In total, we model the long-time behavior of the two-photon correlations by the following function:

$$f(\tau) = A_c \cdot e^{-\frac{\tau}{\tau_c}} \cdot \sin(2\pi f_c \tau) + A_i \cdot e^{-\frac{\tau}{\tau_i}} + c \tag{3.15}$$

While the first two terms describe the intensity fluctuation due to coherent variation of the coupling constant along the cavity axis and incoherent background due to light shifts, the third term describes an offset expected to be 1 for a Poissonian light field. We find values of 1.25 and 1.06 for atom and cavity drive at the first manifold, respectively.

We attribute this additional offset after decay of all dynamics of the system to the random vertical position of the atoms with respect to the cavity mode center which varies from run to run. This position distribution causes fluctuations in the coupling constant, light shift, and overlap with the excitation beams. Therefore, it may be thought of as excess intensity noise of the field emitted from the cavity.

To further investigate the deviation from one, we compare the large-delay offsets with the photon number distributions $P(n)$, i.e. the number of photons of the full measurement interval, averaged over many realizations (Figure 3.7). The width of the latter already indicates an increased variance in comparison to a Poissonian light field shown as red bars. Furthermore, values for $g^{(2)}(0)$ and $g^{(3)}(\mathbf{0})$ as expected from the photon distributions can be calculated via Equation (3.2):

$$g_P^{(2)}(0) = \frac{\sum_n n(n-1)P(n)}{\left[\sum_n nP(n)\right]^2} \tag{3.16a}$$

$$g_P^{(3)}(\mathbf{0}) = \frac{\sum_n n(n-1)(n-2)P(n)}{\left[\sum_n nP(n)\right]^3} \tag{3.16b}$$

The resulting values are given as an inset in Figure 3.7 and we find $g_P^{(2)}(0) = 1.27$ for atom and $g_P^{(2)}(0) = 1.07$ for cavity driving are in good agreement with the large delay averages given above. While error bars on these numbers from the fit are below the presented accuracy, we expect a dominant systematic error stemming from the random choice of the averaging interval with respect to residual oscillations due to atomic motion. This may explain the remaining deviation.

3.4.2. Two-Photon Blockade

We want to investigate whether two-photon blockade, as described by the conditions in Equations (3.11a) and (3.11b) and predicted in Section 3.2.2, can be achieved in our system. This requires second- and third-order photon correlation measurements.

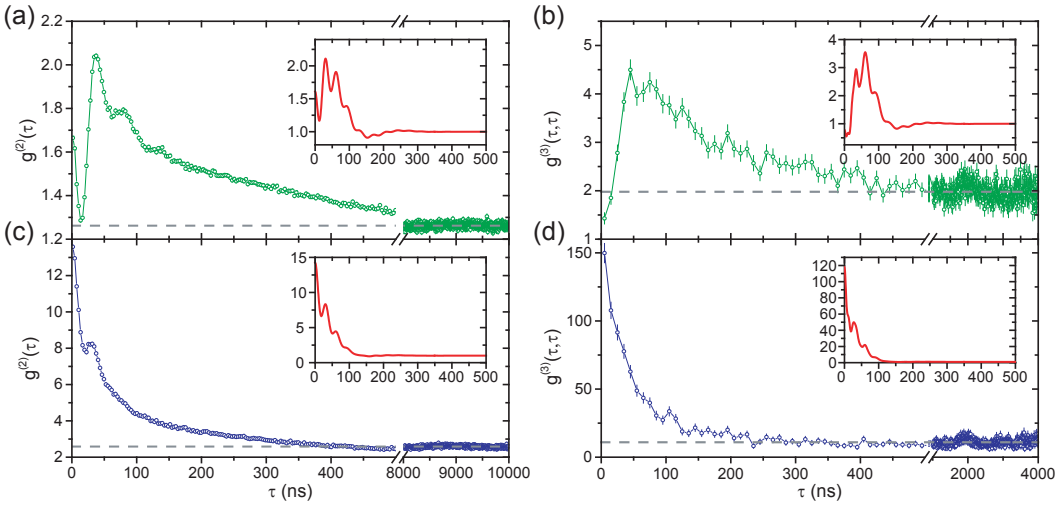

Figure 3.8.: Photon correlations at two-photon resonance. Close to the second manifold at $\Delta_c/2\pi = 9\,\mathrm{MHz}$, second-order photon correlations with 3 ns binning for (a) atom and (c) cavity driving show bunching. In (b) and (d), we show the corresponding third-order photon correlations with antibunching and bunching, respectively. This indicates a two-photon blockade for atom excitation. The increase of the binning to 10 ns in (b) and (d) accounts for the considerably smaller probability of three-photon events. Grey dashed lines indicate the long-time averages and insets depict the corresponding theory, which we add for qualitative comparison.

We tune the drives close to the second manifold (compare Figure 3.2(b,II)) and increase their strengths to $\eta_a/2\pi \approx 1.6\,\mathrm{MHz}$ and $\eta_c/2\pi \approx 1.1\,\mathrm{MHz}$. This allows for significant population of higher states without yet affecting the level structure. Despite the significant driving, the intracavity photon number $\langle\hat{m}\rangle$ remains small at 0.04 for atom and 0.01 for cavity excitation since only a small fraction of the drives is coupled into the joint system. The corresponding correlations are depicted in Figure 3.8.

The second-order photon correlations in Figure 3.8(a) and (c) yield super-Poissonian emission in both cases since $g^{(2)}(0) > 1$ which is indicative of photon numbers higher than one. Cavity excitation shows strong photon bunching with $g^{(2)}(0) = 13.58(8)$ that falls off rapidly and exhibits vacuum-Rabi-oscillations [Kub08]. The observed dynamics for atom driving is more complex. The interplay between conflicting mechanisms, a two-photon resonance on one hand and an emitter that can only absorb one excitation at a time on the other hand, leads to a novel photon-concatenation effect. Since the rate of coherent energy exchange between atom and cavity exceeds the spontaneous decay rate of the system, higher manifolds are populated in stepwise excitation via the emitter. As a consequence, we observe that the second-order correlation function peaks 37.5(15) ns after the trigger photon which indicates that the

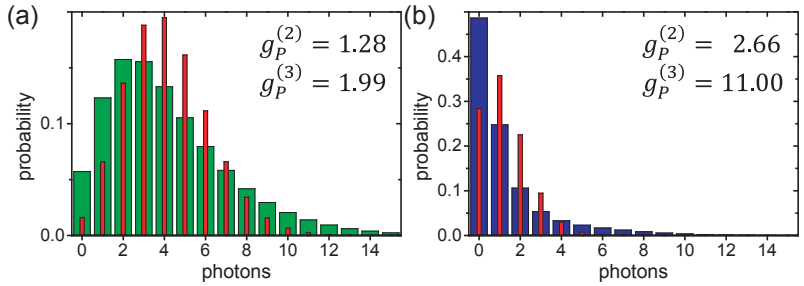

Figure 3.9.: Photon distributions of the probe intervals at two-photon resonance. The photon distribution $P(n)$ per probe interval is depicted for (a) atom and (b) cavity excitation. These distributions are used to calculate the expected values for a second- and third-order photon correlation of a given light field. The deviation in average photon number is partly caused by different driving strengths ($\eta_a/2\pi \approx 1.6\,\mathrm{MHz}$ and $\eta_c/2\pi \approx 1.1\,\mathrm{MHz}$) but mostly due to the different spectral intensities at the driving frequency. The red bars show a Poisson distribution of the same mean photon number.

coupling rate rather than the lifetime determines the probability for detection of a second photon. This is in stark contrast to the first-manifold dynamics described above. As $g^{(2)}(\tau) > g^{(2)}(0)$ for some τ, this behavior violates the Cauchy-Schwarz inequality and is thus quantum in nature [Man95, Mie98]. Again, we find good qualitative agreement with the simulations, but the values for uncorrelated photons at large delays, even after the motional dynamics, deviate from 1 significantly for both, atom driving with 1.26 and cavity driving with 2.58.

While Figure 3.8(a) and (c) indicate multi-photon emission and fulfill condition (3.11a), we now have to show that in addition higher photon numbers are suppressed via the third-order correlations. The time-dependent third-order photon correlation is given by $g^{(3)}(\tau_1, \tau_2) = \langle \hat{n} \cdot \hat{n}(\tau_1) \cdot \hat{n}(\tau_1 + \tau_2) \rangle / \langle \hat{n} \rangle^3$ (normal and time ordered). τ_1 is the delay between the first and second photon and τ_2 the delay between the second and third photon. In general, $g^{(3)}(\tau_1, \tau_2)$ gives a two-dimensional plane which grants insight into the dynamics of the system, especially the second manifold.

For now, we focus on $g^{(3)}(\tau, \tau)$ as depicted in Figure 3.8(b) and (d). In this case, the time separation between all three photons grows with τ. For time intervals exceeding the time scale of the internal coherence, $\tau \gg 2/(\kappa + \gamma)$, $g^{(3)}(\tau, \tau)$ is proportional to the probability of detecting three uncorrelated photons. As anticipated, we observe a strong bunching in case of cavity driving that originates in the enhancement of excitation to higher manifolds and inhibits a two-photon blockade. Atom excitation, however, shows antibunching as expected from simulations. In contrast to theory, $g^{(3)}(0, 0) = 1.43(12)$ is above 1, the value expected for a Poissonian light field. However, we do sig-

nificantly underpass the long-term averaged value of 1.98(1) that serves as a reference for uncorrelated photons. As described in Section 3.4.1, this value is above 1 due to technical fluctuations that shift $g^{(3)}(\tau,\tau)$ to higher values. Again, we confirm this by calculating our expected offset for the second- and third-order correlation via the photon number distribution per interval (Equations (3.16a) and (3.16b)). The distributions and comparison to a Poissonian field of the same mean photon number for atom and cavity driving are shown in Figure 3.9. In case of atom excitation, we find $g_P^{(2)}(0) = 1.28$ and $g_P^{(3)}(\mathbf{0}) = 1.99$ for uncorrelated photons. These values agree very well with the long-time averaged $g^{(2)}(\tau)$ and $g^{(3)}(\tau,\tau)$ and prove that the field exhibits an increased variance, likely due to residual atomic motion and a distribution of positions with respect to the cavity mode and atom drive for different atoms. We can therefore conclude that the $g^{(3)}(\tau,\tau)$ demonstrates a reduction of the probability of detecting more than two photons at the same time, while two-photon emission is enhanced compared to a Poissonian field of the same mean photon number, as shown by $g^{(2)}(0)$. In consequence, our atom-driven CQED system thus exhibits a two-photon blockade. In contrast, cavity driving displays photon bunching in $g^{(2)}(\tau)$ and $g^{(3)}(\tau,\tau)$. Both, the results from atom and cavity driving, agree qualitatively with the simulated results.

At the end of this section, we want to focus on additional features as described by the full $g^{(3)}(\tau_1,\tau_2)$ and understand more about the dynamics of the two-photon blockade. Figure 3.10(a) and (b) show the full two-dimensional plane of $g^{(3)}(\tau_1,\tau_2)$ for atom and cavity driving. The previous $g^{(3)}(\tau,\tau)$ for the description of three uncorrelated photons at large time delays corresponds to a diagonal cut through the origin. As we have already seen before, the two exhibit distinctly different behavior.

When the drive excites the cavity field, we find the highest probability for coincidences at zero time delay and a rapid decay to the steady state value for all delays. This indicates that the system tends to emit three and more photons in bunches. We are detuned to the first manifold and close to the second manifold which favors double excitation. The photon bunching described in Section 3.2.2 causes excitation to even higher manifolds. Once excited to the third manifold, the system rapidly returns to the steady state with the highest probability to detect all photons at zero time delay. The system can be qualitatively understood by considering the relevant decay paths when starting in a given excited state of the third manifold. Along the abscissa and ordinate, we find the dynamically interesting case of $(\tau_1,\tau_2) = (0,\tau)$ where the third-order correlation yields information on the conditional evolution of $\langle\hat{n}\rangle$ ($\langle\hat{n}^2\rangle$), i.e. the dynamics on the first (second) manifold for positive (negative) τ [Koc11b]. The experimental results for cavity driving are displayed in Figure 3.10(d). We find excellent agreement with a theory that has been scaled and shifted which can be understood as a correction up to first order to compensate for atomic motion and displacement. As the bunching falls off to steady state,

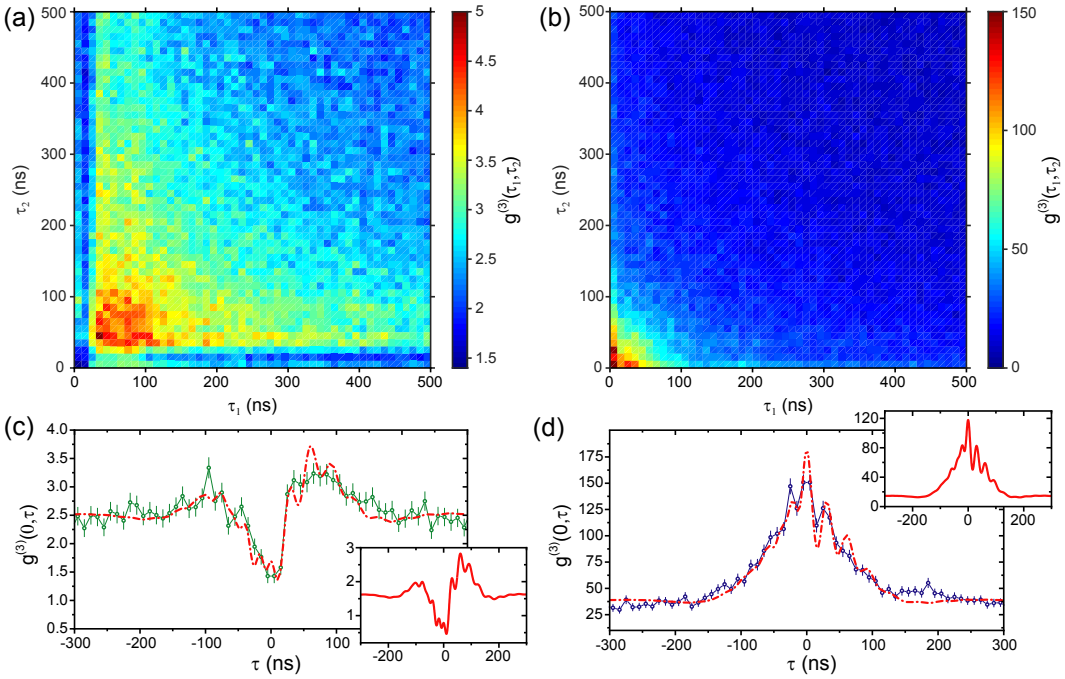

Figure 3.10.: 2D plane of third-order photon correlation. The two-dimensional plane of the third-order photon correlation $g^{(3)}(\tau_1, \tau_2)$ is displayed for (a) atom and (b) cavity excitation close to the second manifold with a binning of 10 ns. The corresponding cuts along the vertical and horizontal axis $g^{(3)}(0, \tau)$ are depicted in (c) and (d). For qualitative comparison, the theory for the same parameters (inset) has been scaled and shifted to fit experimental data (dash dotted red lines).

data and theory exhibit oscillations at different frequencies for positive and negative times that reflect the coherent evolution on the first and second manifold at frequency $2g$ and $2\sqrt{2}g$, respectively [Koc11b]. At large τ, we now observe an offset of 27.8(3). This is much larger than for three independent photons (Figure 3.8(d)). For $g^{(3)}(0, \tau)$, two of the photons are correlated for any τ and therefore we do not expect the correlation to approach 1 for large τ, but the value of $g^{(2)}(0) \cdot g^{(2)}(\tau)$ for $\tau \gg 2/(\kappa + \gamma)$ [Koc11a]. While this yields a good qualitative understanding, we do not find accurate quantitative agreement. This is considered to be a consequence of the deviation from the expectation for a coherent field at large delays.

Exciting the atom instead leads to drastically different behavior and requires to consider the excitation path in addition to the decay, as we already observed for the second-order photon correlations. In Figure 3.10(a), we find that $g^{(3)}(0, 0)$ marks the overall lowest point which complements our argumentation for a two-photon blockade from before. Several notable dynamical features are observed. Increasing the delay between all three photons leads to a bunched region between 20 ns to 100 ns as was also shown in Figure 3.8(b).

This is not as prominent along the horizontal or vertical axis, that are shown as a cut in Figure 3.10(c), which demonstrates an enhanced probability for the emission of independent photons while any correlated emission of three photons remains weak. Note that at the peak of $g^{(3)}(\tau,\tau)$ at $\tau \approx 60\,\mathrm{ns}$ (Figure 3.8(b)) the third photon has a delay to the first that exceeds the coherence time of the system. The fact that this maximum exceeds the value for uncorrelated photons and peaks on the second oscillation after the first detection may indicate a photon concatenation effect for three photons similar to the one for two excitations where now three photons can only be added stepwise to the system. At close observation of $g^{(3)}(0,\tau)$, we find a significant asymmetry in the larger bunching region around 75 ns at positive delays. In further theoretical investigations, its occurrence agrees with the inverse of the probe detuning to the first manifold. The detection of two photons very likely brings the system to the ground state upon which the probability for re-excitation is enhanced. If the single photon arrives first, however, the stepwise excitation via the atom hinders emission of two-photons and the third-order correlation function remains low for larger delays. Finally, the beating of the first and second manifold dressed states at frequencies $2g$ and $2\sqrt{2}g$ are again visible in theory and faintly in data.

3.5. Conclusion

In conclusion, we have given a definition of multi-photon blockade and derived some criteria that can be tested experimentally. We have shown in theory and experiment that driving the quantum emitter instead of the resonator improves the nonlinear response of the strongly coupled system. This allows us to demonstrate both single- and two-photon blockade. Future experiments could explore the extension of the blockade mechanism to even higher photon numbers. For example, simulations indicate that three-photon blockade seems feasible with our system. As blockade truncates the high end of the photon-number distribution, any additional reduction of the low end [Far08, Kub08] may enable carving of various non-classical photon states like those containing n photons. Excitation of the cavity at higher manifolds, as explored in this chapter, may appear as a natural candidate. Direct production of n-photon states has also been proposed for strong atom driving, $\eta_a \gg g$, with the cavity tuned as to selectively enhance a specific n-photon transition between dressed atom-laser states [Muñ14]. Selective population of higher-energetic atom-cavity states might be possible by stepwise excitation of the symmetry-changing transitions ($|n,\pm\rangle \rightarrow |n+1,\mp\rangle$). When exciting the atom instead of the cavity, these transitions exhibit larger and thus more favorable strengths [Fin08]. Finally, driving atom and cavity simultaneously might enable a quantum interference induced photon blockade where single-photon emission results

from destructive interference between different transition paths [Tan15].

4. Two Modes Coupled to an N-type Atom: Interacting Light Fields

4.1. Introduction: Coupling Photons of Two Light Fields

In the previous chapter, we have seen an example of quantum nonlinear optics between indistinguishable photons of the same continuous driving field. In contrast, linear quantum networking does not exploit such direct interactions between photons, since each photon populates a separate well-defined spatio-temporal mode and, e.g., its polarization encodes the qubit [Rei15]. Controlled interactions between these qubits are required to process the associated quantum information [Kok10]. A model platform is provided by cavity quantum electrodynamics [Kim08, Cha14]. As recently demonstrated, interaction with a photon leaves a trace in the atom that can be read out in a second step [Nog99, Dua04] enabling the realization of non-destructive photon detection [Gue07, Gle07, Rei13, Tie14a] and an atom-photon gate [Rau99, Rei14]. A gate between two photons is then performed sequentially by consecutive interaction of the photons with the CQED system [Hac16]. Engineering a system that catalyzes a direct nonlinear interaction between simultaneous photons in two distinct modes is still an outstanding challenge. For this purpose, its energy eigenstates must depend nonlinearly on the number of photons in each of the modes, a condition we refer to as strong coupling of light fields in analogy to CQED. Such a system holds potential for all-optical quantum nonlinear sensing. Hereby, photons measure photons while the system remains inactive in the actual sensing process.

Here, we will demonstrate strong nonlinear coupling between photons in two different cavity modes. Without a medium, two cavity modes do not interact which leads to a purely harmonic energy level structure as depicted in Figure 4.1. Only adding a four-level atom that forms an N-type system where two transitions (*probe* and *signal*) are strongly-coupled to the cavity modes and connected via a strong coherent field (*control*) allows us to mediate interactions between the fields. Probe and control form a lambda configuration with a common excited and two ground states featuring electromagnetically

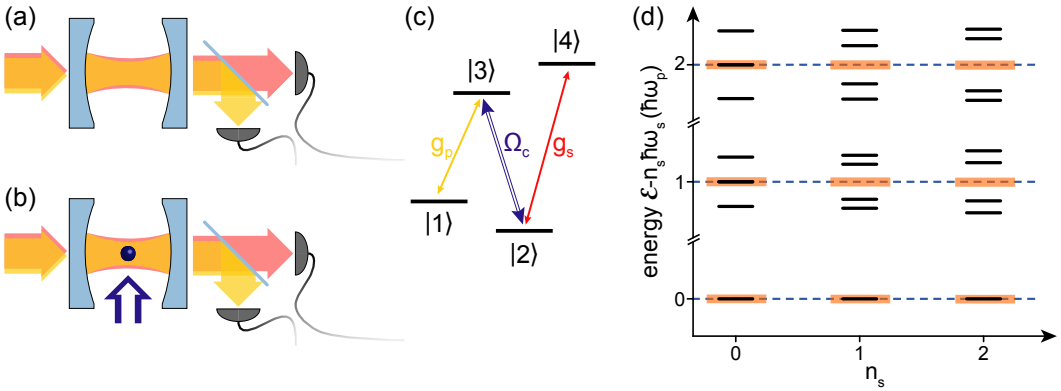

Figure 4.1.: Strongly coupled light fields. (a) Two light fields, probe (yellow) and signal (red), resonant to different modes of an optical cavity do typically not show any interaction and the harmonic energy ladders persist into the joint system (orange bars in (d)). (b) However, coupling these modes strongly to two transitions of a four-level atom (c) with coupling strengths g_p and g_s allows us to mediate an interaction between these modes via a coherent field of strength Ω_c that causes EIT. (d) The resulting energy level structure (black bars) is nonlinear in the number of photons in both modes, n_p (ordinate) and n_s (abscissa).

induced transparency [Har90, Fle05]. Here, quantum interference puts the system into a dark superposition between the two ground states, eliminating the excited state population, rendering the otherwise opaque medium transparent for the probe light. Signal light in turn couples the control ground state to a second excited state thus disturbing the fragile ground state coherence. The resulting energy level structure displays a landscape of quadruplets for each combination of probe and signal photon number (Figure 4.1(d)). The splittings within the quadruplets depend nonlinearly on the number of photons in each cavity mode [Wer99, Reb02, Ber06, Le 16]. We show that this enables realization of a photon-photon switch in a regime of mutual blocking (anticorrelation) between photons in different modes. Furthermore, the system can be tuned to correlated transmission where photons only transit the cavity conjunctly. Photons of the same mode, however, do not interact and travel undisturbed.

We have seen that strong coupling between a single emitter and a cavity requires a small cavity length to enhance the vacuum fluctuations [Vah03]. On the downside, this increases the optical mode spacing, making it difficult to reach resonance on two different atomic transitions. As a result, recent exemplary studies worked with substantial detunings [Alb11] or only one cavity-coupled and another free-space mode [Che13, Bec14] which made it necessary to use many atoms to observe significant effects. However, the prospect of strong nonlinear interactions between light fields has even motivated many free-space realizations, though the single-photon coupling remains

small. Thus, switches [Yan01, Bra03, Che05, Baj09], nonlinear phase shifts [Che06, Fei15, Li15], transistors [Che13], and even partially non-destructive detection [Hos16] have been shown. Recently, also systems exploiting Rydberg states in atomic ensembles with long-range dipole-dipole coupling embarked on the challenge to realize controlled interactions between two distinct light fields [Fir13, Bus17, Tho17].

In this chapter, we will first focus on the theoretical description of an N-type atom coupled strongly to two cavity modes in Section 4.2. After a brief introduction to the system, we build its Hamiltonian and derive the time-independent form. In Section 4.2.2, we discuss the resulting energy level structure that lies at the heart of the later observed quantum effects and possible future applications. We outline the ansatz for a full quantum simulation following the master equation approach in Section 4.2.3 and briefly introduce our implementation. The major experimental challenge of this work that hindered realization of this system ever since it was first proposed [Ima97] is caused by the condition of resonant coupling of two cavity modes to two atomic transitions. Our efforts for reaching resonance between cavity modes and transitions are described in Section 4.3. We demonstrate a rough adjustment via the cavity length (Section 4.3.1), fine tuning via differential Stark shifts (Section 4.3.2) and address the spatial mode overlap within the cavity in Section 4.3.3. In Section 4.4, we describe the atomic states used for the experiment as well as the experimental sequence employed to prepare these states and to acquire the data, which is shown and discussed in Section 4.5. For the latter, we start by investigating each transition separately, show that strong coupling is reached for both and the high-quality of EIT for the probe (Section 4.5.1). In Section 4.5.2, we spectroscopically probe the (n_p=1,n_s=1)-manifold to show direct evidence of the new energy level structure. Interaction between the fields is then demonstrated via photon-photon switching (Section 4.5.3) and cross-correlations that display mutual blocking and conjunct transit of photons in different modes (Section 4.5.4). We conclude with an outlook on future perspectives of the system (Section 4.6).

4.2. Theory

The system consists of a four-level atom and two cavity modes (Figure 4.2). The four atomic levels $i = 1, 2, 3, 4$ are denoted as $|i\rangle$ with eigenfrequency ω_i. The excited states $j = 3, 4$ are further described by the spontaneous polarization decay rate $\gamma_j = \sum_k \gamma_{jk}$ that is the sum of decays to ground states $k = 1, 2$ which themselves are (meta-) stable ($\gamma_k = 0$) except for a dephasing between the two states γ_d due to technical fluctuations. The transition from an initial state $|i\rangle$ to a final state $|f\rangle$ at frequency ω_{fi} is then represented by the operator $\hat{\sigma}_{fi} = |f\rangle\langle i|$.

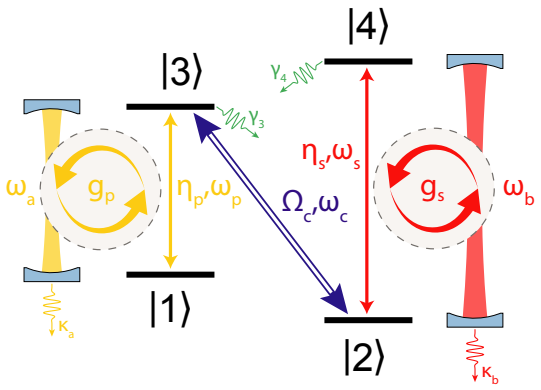

Figure 4.2.: Physical system. The level scheme with all central parameters consists of atomic states $|1\rangle$,$|2\rangle$, $|3\rangle$, and $|4\rangle$ coupled to cavity modes $|a\rangle$ and $|b\rangle$.

The cavity modes A and B are described by their resonance frequencies ω_a and ω_b as well as the field decay rates κ_a and κ_b. The photon creation (annihilation) operators are denoted as $\hat{a}^\dagger$ ($\hat{a}$) and $\hat{b}^\dagger$ ($\hat{b}$), respectively. The photon numbers of the corresponding drives, probe and signal, are then given by $\hat{n}_p = \hat{a}^\dagger\hat{a}$ and $\hat{n}_s = \hat{b}^\dagger\hat{b}$. The probe transition from ground state $|1\rangle$ to excited state $|3\rangle$ couples strongly to cavity mode A with a coupling strength g_p as described by standard CQED in Section 2.1. This cavity mode is excited by the probe field of frequency ω_p and driving strength η_p causing an average intracavity photon number $\langle\hat{n}_p\rangle = \eta_p^2/\kappa_a^2$ on resonance. Likewise, the signal field of frequency ω_s and strength η_s ($\langle\hat{n}_s\rangle = \eta_s^2/\kappa_b^2$) drives mode B which is strongly-coupled to the signal transition $|2\rangle \leftrightarrow |4\rangle$ with strength g_s. The control laser beam of frequency ω_c connects the separate probe and signal systems by driving the $|2\rangle \leftrightarrow |3\rangle$ transition at Rabi frequency Ω_c causing EIT. Since we work in a CQED environment, we refer to this as cavity EIT (CEIT) [Sou13].

To get an intuition, this system may be understood as consisting of either a lambda (probe) or vee (signal) EIT system where the control-coupled additional state, $|2\rangle$ or $|3\rangle$, respectively, is dressed by the respective other cavity drive [Fle05]. In analogy to the lambda and vee configuration, we refer to the system as N-type[1].

4.2.1. Hamiltonian

The derivation of the time independent Hamiltonian is very similar to Reference [Le 16]. For simplicity, we choose $\hbar = 1$. The full system Hamiltonian is

[1]Note that for lambda-, vee- and N-type systems the naming simply sketches the applied level scheme: $\Lambda, \vee, N$.

described by:

$$\hat{\mathcal{H}} = \hat{\mathcal{H}}_{atom} + \hat{\mathcal{H}}_{cavity} + \hat{\mathcal{H}}_{int} + \hat{\mathcal{H}}_{d} \tag{4.1}$$

Here, $\hat{\mathcal{H}}_{atom}$ and $\hat{\mathcal{H}}_{cavity}$ yield the relevant eigenenergies of the unperturbed atom and cavity, respectively. $\hat{\mathcal{H}}_{int}$ describes the interaction between atomic transitions and cavity modes and $\hat{\mathcal{H}}_{d}$ contains the external driving fields applied to the system. All terms are defined analogously to Section 2.1.1. For a four-level atom and a cavity with two different longitudinal modes, we find:

$$\hat{\mathcal{H}}_{atom} = \omega_1 \hat{\sigma}_{11}^{\dagger}\hat{\sigma}_{11} + \omega_3 \hat{\sigma}_{33}^{\dagger}\hat{\sigma}_{33} + \omega_4 \hat{\sigma}_{44}^{\dagger}\hat{\sigma}_{44} \tag{4.2a}$$

$$\hat{\mathcal{H}}_{cavity} = \omega_a \hat{a}^{\dagger}\hat{a} + \omega_b \hat{b}^{\dagger}\hat{b} \tag{4.2b}$$

We have chosen the zero point of energy at level $|2\rangle$ without loss of generality. The interaction of atomic transitions to their respective cavity mode in the dipole and rotating wave approximation is given by:

$$\hat{\mathcal{H}}_{int} = g_p \left(\hat{a}^{\dagger}\hat{\sigma}_{13} + \hat{\sigma}_{13}^{\dagger}\hat{a}\right) + g_s \left(\hat{b}^{\dagger}\hat{\sigma}_{24} + \hat{\sigma}_{24}^{\dagger}\hat{b}\right) \tag{4.3}$$

The driving term for the three light fields, the two cavity drives (probe and signal) as well as the control beam, can be written as:

$$\hat{\mathcal{H}}_{d} = \eta_p e^{-i\omega_p t}\hat{a}^{\dagger} + \eta_s e^{-i\omega_s t}\hat{b}^{\dagger} + \Omega_c e^{-i\omega_c t}\hat{\sigma}_{23}^{\dagger} + \text{h.c.} \tag{4.4}$$

Note that our definition of Ω_c corresponds to half of the standard definition of the Rabi frequency.

The full system Hamiltonian, $\hat{\mathcal{H}}$, can be transformed to a rotating frame of reference in which the Hamiltonian is time-independent. By defining the frequencies of the drives relative to the frequency of their respective cavity mode,

$$\Delta_p = \omega_p - \omega_a \tag{4.5a}$$

$$\Delta_s = \omega_s - \omega_b \tag{4.5b}$$

$$\Delta_c = \omega_c - \omega_{32}, \tag{4.5c}$$

and the detunings between the atomic transitions and the cavity frequencies,

$$\Delta_{31} = \omega_a - \omega_{31} \tag{4.6a}$$

$$\Delta_{42} = \omega_b - \omega_{42}, \tag{4.6b}$$

we find the final Hamiltonian to be:

$$\begin{aligned}\hat{\mathcal{H}} = {} & (\Delta_p - \Delta_c + \Delta_{31})\hat{\sigma}_{11}^{\dagger}\hat{\sigma}_{11} - \Delta_c \hat{\sigma}_{33}^{\dagger}\hat{\sigma}_{33} \\ & - (\Delta_s + \Delta_{42})\hat{\sigma}_{44}^{\dagger}\hat{\sigma}_{44} \\ & - \Delta_p \hat{a}^{\dagger}\hat{a} - \Delta_s \hat{b}^{\dagger}\hat{b} \\ & + g_p \left(\hat{a}^{\dagger}\hat{\sigma}_{13} + \hat{\sigma}_{13}^{\dagger}\hat{a}\right) + g_s \left(\hat{b}^{\dagger}\hat{\sigma}_{24} + \hat{\sigma}_{24}^{\dagger}\hat{b}\right) \\ & + (\eta_p \hat{a}^{\dagger} + \eta_s \hat{b}^{\dagger} + \Omega_c \hat{\sigma}_{23}^{\dagger} + \text{h.c.})\end{aligned} \tag{4.7}$$

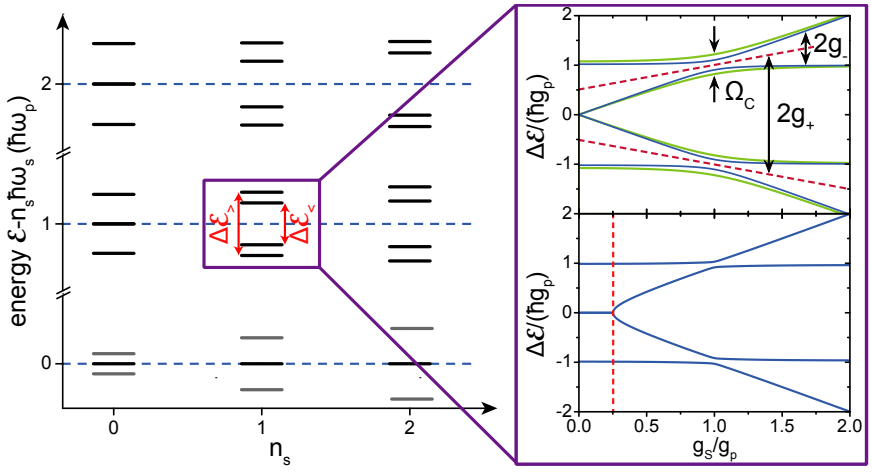

Figure 4.3.: Energy level structure and eigenstates. The new energy eigenstates form quadruplets that exhibit nonlinear splittings $\Delta\mathcal{E}_{\gtrless}$ in probe n_p (ordinate) and signal photon number n_s (abscissa). Blue lines in the zooms show the tuning of the quadruplet versus the signal coupling strength for the (n_p=1,n_s=1)-manifold without (top) and with (bottom) coupling to the environment via spontaneous atomic polarization and cavity field decay. The green line demonstrates the increased splitting at the avoided crossing between each upper or lower doublet due to a larger Ω_c.

Diagonalization of this Hamiltonian allows us to find the eigenstates and eigenenergies of the system displayed in Figure 4.3.

4.2.2. Energy Level Structure and Eigenstates

For simplicity, we choose the detunings to be zero, $\Delta_{31} = \Delta_{42} = \Delta_c = 0$. Furthermore, we assume that the coupling strengths g_p and g_s exceed their respective field decay rates κ_a and κ_b and polarization decay rates γ_3 and γ_4. The control Rabi frequency remains smaller or on the order of the couplings, $\Omega_c \lesssim (g_p, g_s)$.

Yet without dissipation, this yields the novel set of eigenstates arranged in quadruplets for each (n_p,n_s)-manifold, as depicted in Figure 4.3. The ground state exhibits a small dressing due to the control field. Along both axes lie the undisturbed eigenstates of the probe lambda- (vertical) and signal vee-type (horizontal) cavity EIT systems. Without probe excitations ($n_p = 0$), we find the harmonic ladder of the empty cavity resonance for the signal light. Above and below, lie the dressed states according to vee-type CEIT. As the population accumulates in state $|1\rangle$, these remain unpopulated unless the control is turned off and the atom is prepared in $|2\rangle$. For $n_s = 0$, we recover the known solution of cavity EIT for the probe: the dressed states are extended by a long-lived EIT state at zero detuning [Müc10, Sou13]. Adding just a single

signal excitation splits the formerly harmonic EIT resonance and leads to a new quadruplet of states with the energy splittings $\Delta\mathcal{E}_>$ and $\Delta\mathcal{E}_<$. A simple form for these splittings can be found in case of zero detunings. Then, the N-type Hamiltonian of Equation (4.7) in matrix form for the base vectors of the atomic states $\{|1\rangle, |2\rangle, |3\rangle, |4\rangle\}$ becomes:

$$\hat{\mathcal{H}} = \begin{pmatrix} 0 & 0 & i\tilde{g}_p & 0 \\ 0 & 0 & -\Omega_c & i\tilde{g}_s \\ -i\tilde{g}_p & -\Omega_c & 0 & 0 \\ 0 & -i\tilde{g}_s & 0 & 0 \end{pmatrix}, \tag{4.8}$$

where we have introduced $\tilde{g}_p = \sqrt{n_p} g_p$ and $\tilde{g}_s = \sqrt{n_s} g_s$ for brevity. To find the eigenenergies and eigenstates of $\hat{\mathcal{H}}$, we have to solve the eigenvalue problem: $|\hat{\mathcal{H}} - \mathcal{E}I| = 0$. Here, I is the identity matrix. The energies $\mathcal{E}_j^{(n_p,n_s)}$ of the new eigenstates $\left|\psi_j^{(n_p,n_s)}\right\rangle$ with $j = 1, 2, 3, 4$ are then given as the roots of the resulting quartic eigenvalue equation:

$$\mathcal{E}_1^{(n_p,n_s)} = \frac{1}{\sqrt{2}}\sqrt{\left(\tilde{g}_p^2 + \tilde{g}_s^2 + \Omega_c^2\right) + \sqrt{\left(\tilde{g}_p^2 + \tilde{g}_s^2 + \Omega_c^2\right)^2 - 4\tilde{g}_p^2\tilde{g}_s^2}} \tag{4.9a}$$

$$\mathcal{E}_2^{(n_p,n_s)} = \frac{1}{\sqrt{2}}\sqrt{\left(\tilde{g}_p^2 + \tilde{g}_s^2 + \Omega_c^2\right) - \sqrt{\left(\tilde{g}_p^2 + \tilde{g}_s^2 + \Omega_c^2\right)^2 - 4\tilde{g}_p^2\tilde{g}_s^2}} \tag{4.9b}$$

$$\mathcal{E}_3^{(n_p,n_s)} = -\frac{1}{\sqrt{2}}\sqrt{\left(\tilde{g}_p^2 + \tilde{g}_s^2 + \Omega_c^2\right) - \sqrt{\left(\tilde{g}_p^2 + \tilde{g}_s^2 + \Omega_c^2\right)^2 - 4\tilde{g}_p^2\tilde{g}_s^2}} \tag{4.9c}$$

$$\mathcal{E}_4^{(n_p,n_s)} = -\frac{1}{\sqrt{2}}\sqrt{\left(\tilde{g}_p^2 + \tilde{g}_s^2 + \Omega_c^2\right) + \sqrt{\left(\tilde{g}_p^2 + \tilde{g}_s^2 + \Omega_c^2\right)^2 - 4\tilde{g}_p^2\tilde{g}_s^2}} \tag{4.9d}$$

This nested radical can be denested according to the following equation [Wes99]:

$$\sqrt{X \pm Y} = \frac{1}{\sqrt{2}}\left(\sqrt{X + \sqrt{X^2 - Y^2}} \pm \sqrt{X - \sqrt{X^2 - Y^2}}\right) \tag{4.10}$$

Thus, we find a simple form of the splittings $\Delta\mathcal{E}_>$ and $\Delta\mathcal{E}_<$ in terms of the new coupling strengths of the joint system $g_\pm(n_p, n_s)$:

$$\begin{aligned} &\Delta\mathcal{E}_{\gtrless}(n_p, n_s) = 2\hbar\left(g_+(n_p, n_s) \pm g_-(n_p, n_s)\right) \\ &\text{with: } g_\pm(n_p, n_s) = \frac{1}{2}\sqrt{\left(\sqrt{n_p} g_p \pm \sqrt{n_s} g_s\right)^2 + \Omega_c^2} \end{aligned} \tag{4.11}$$

This is depicted graphically in the upper zoom of Figure 4.3 at the example of the (1,1)-manifold. The eigenenergies $\mathcal{E}_j^{(n_p,n_s)}$ in terms of $g_\pm(n_p, n_s)$ are

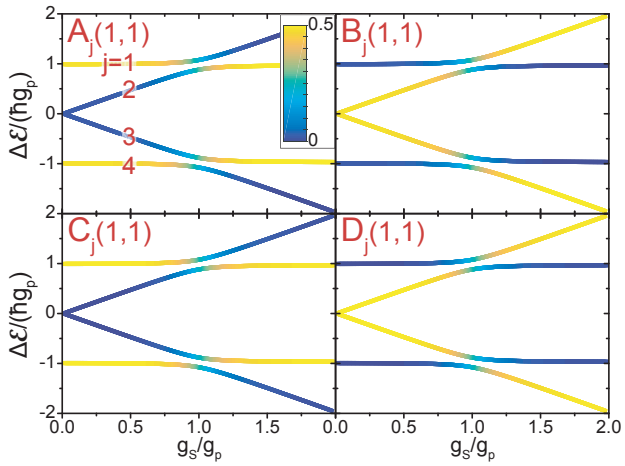

Figure 4.4.: Avoided crossing of the eigenstates. The eigenstates of the (1,1)-manifold display the the typical behavior for an avoided crossing. The contribution of amplitudes $A_j(1,1)$, $B_j(1,1)$, $C_j(1,1)$, and $D_j(1,1)$ of the uncoupled states to each new eigenstate inverts at the crossing point $g_p = g_s$.

described by:

$$\mathcal{E}_1^{(n_p,n_s)} = \quad (g_+(n_p,n_s) + g_-(n_p,n_s)) \tag{4.12a}$$

$$\mathcal{E}_2^{(n_p,n_s)} = \quad (g_+(n_p,n_s) - g_-(n_p,n_s)) \tag{4.12b}$$

$$\mathcal{E}_3^{(n_p,n_s)} = -(g_+(n_p,n_s) - g_-(n_p,n_s)) \tag{4.12c}$$

$$\mathcal{E}_4^{(n_p,n_s)} = -(g_+(n_p,n_s) + g_-(n_p,n_s)) \tag{4.12d}$$

Finally, the corresponding new eigenstates $|\psi_j^{(n_p,n_s)}\rangle$ are given in terms of the amplitudes $A_j(n_p,n_s)$, $B_j(n_p,n_s)$, $C_j(n_p,n_s)$, and $D_j(n_p,n_s)$ of the uncoupled states $|i\rangle \otimes |n_p\rangle \otimes |n_s\rangle$ of atom, probe and signal light field:

$$\begin{aligned}\left|\psi_j^{(n_p,n_s)}\right\rangle =& A_j(n_p,n_s)\ |1,n_p,n_s\rangle + B_j(n_p,n_s)\ |2,n_p-1,n_s\rangle \\ &+C_j(n_p,n_s)\ |3,n_p-1,n_s\rangle + D_j(n_p,n_s)\ |4,n_p-1,n_s-1\rangle\end{aligned} \tag{4.13}$$

The full analytical form of the amplitudes, including detunings, can be found in Reference [Le 16].

At the example of the (1,1)-manifold, we demonstrate how increasing the signal coupling strength dresses the control ground state which in turn splits the EIT peak into a doublet that exhibits an avoided crossing with the former Jaynes-Cummings states at $g_s = g_p$, with a splitting of Ω_c. This is consistently reflected in the eigenstate amplitudes depicted in Figure 4.4. As expected, states change in nature at the point of the crossing. As an example, we follow the upper $j = 1$ state that starts close to $\hbar g_p$ at $\hbar g_{p,eff}$:

$$g_{p,eff} = \Delta\mathcal{E}_>(n_p,0)/2\hbar = \sqrt{(\sqrt{n_p}g_p)^2 + \Omega_c^2} \tag{4.14}$$

At small g_s, the $j = 1$ remains unaffected by the new signal-dressed states that are far detuned. It is dominated by the probe transition with amplitudes A_1 and C_1 corresponding to state $|1\rangle$ and $|3\rangle$. The admixture of the signal transition via B_1 and D_1 gets stronger the more g_s approaches $g_{p,eff}$ and all atomic states contribute almost equally at the minimum splitting between $j = 1$ and $j = 2$. After this avoided crossing, $j = 1$ turns into a state defined by the signal states $|2\rangle$ and $|4\rangle$. Similar behaviors are also observed for states $j = 2, 3, 4$. However, many parameters such as g_p, g_s, n_p, n_s, Ω_c, and the detunings $\Delta_{31} = \Delta_{42} = \Delta_c$ contribute to the amplitudes.

Finally, if we add decoherence to the system in the form of spontaneous emission of excited states and loss of photons from the cavity modes by introducing complex detunings into the Hamiltonian [Le 16], we find that the splitting of the EIT resonance displays an onset at small g_s (lower zoom in Figure 4.3), analogous to the strong coupling condition of cavity quantum electrodynamics.

In summary, though each mode exhibits a harmonic energy ladder at resonance, coupling between the cavity modes mediated by the N-type atom leads to a significant splitting already for a single photon in each mode. Moreover, the splitting depends nonlinearly on the number of photons in mode A and B. We refer to this as strongly coupled light fields.

4.2.3. Quantum simulation

In order to simulate quantum dynamical effects, e.g. photon correlations, it is necessary to perform a full quantum simulation of the system including dissipative processes. To this end, we solve the master equation of the system as presented in Section 2.1.2. For the N-type system, the dissipation operators $\hat{C}_i$ include the atomic polarization decays,

$$\hat{C}_{13} = \sqrt{\gamma_{13}}\hat{\sigma}_{13} \tag{4.15a}$$
$$\hat{C}_{23} = \sqrt{\gamma_{23}}\hat{\sigma}_{23} \tag{4.15b}$$
$$\hat{C}_{14} = \sqrt{\gamma_{14}}\hat{\sigma}_{14} \tag{4.15c}$$
$$\hat{C}_{24} = \sqrt{\gamma_{24}}\hat{\sigma}_{24}, \tag{4.15d}$$

and cavity dissipation of both modes,

$$\hat{C}_a = \sqrt{\kappa_a}\hat{a} \tag{4.16a}$$
$$\hat{C}_b = \sqrt{\kappa_b}\hat{b}. \tag{4.16b}$$

A dephasing of rate γ_d between the ground states is modeled as a pure dephasing of $|2\rangle$ without relaxation [Tem11]:

$$\hat{C}_{22} = \sqrt{\gamma_d}\hat{\sigma}_{22} \tag{4.17}$$

Further possible polarization decays or dephasings are specific to the concrete implementation or level scheme and are not considered in the theory presented here. With the $\hat{C}_i$, we build the Lindblad superoperator according to Equation (2.29). Thus, we follow the formal solution to calculate steady state expectation values or the cross-correlation function $G^{(2)}_{sp}(\tau)$ between the two light fields:

$$\begin{aligned} G^{(2)}_{sp}(\tau) &= \langle \hat{n}_s(0)\hat{n}_p(\tau)\rangle \\ &= \langle \hat{b}^\dagger(0)\hat{a}^\dagger(\tau)\hat{a}(\tau)\hat{b}(0)\rangle \\ &= \mathrm{tr}(\hat{a}^\dagger\hat{a}e^{\mathcal{L}\tau}(\hat{b}\rho_{ss}\hat{b}^\dagger)) \end{aligned} \tag{4.18}$$

Analogously to Equation (2.34), a first signal photon from cavity mode B projects the system into the state $\hat{b}\rho_{ss}\hat{b}^\dagger$. The term $\hat{a}^\dagger\hat{a}$ then gives time dependent probability to detect a probe photon from cavity mode A during the subsequent equilibration process. The normalized cross-correlation function is defined as $g^{(2)}_{sp}(\tau) = G^{(2)}_{sp}(\tau)/(\langle\hat{n}_s\rangle\langle\hat{n}_p\rangle)$. As for the normal $g^{(2)}(\tau)$, $g^{(2)}_{sp}(\tau) = 1$ for independent photons, $g^{(2)}_{sp}(\tau) < 1$ for anticorrelated and $g^{(2)}_{sp}(\tau) > 1$ for correlated fields. However, the Cauchy-Schwarz inequalities [Mie98] and thus the test for quantum behavior in emission via classical bounds do not apply for a cross-correlation.

Using the theory described in this and previous sections, we have written a software framework in the programming language Python that allows to easily perform simulations of our system. As a basis, we use the *Quantum Toolbox in Python* (QuTiP) [Joh13] that allows creating a Hilbert space, the definition of quantum objects therein and numerically solves the system dynamics via, e.g., the master equation or quantum Monte-Carlo method. We have programmed a convenience layer based on QuTiP that implements the system's Hamiltonian as well as the operators. It provides the functionality to perform correlation and spectroscopic simulations. This leads to a very rapid workflow and parameter tuning during theoretical investigation of the system.

Via this framework, we produce the simulations shown in Figures 4.11, 4.12, 4.13 and 4.14 in the following sections. However, since numerical simulations with four atomic levels and two cavity modes with each ≥ 3 Fock states are computationally intensive, we use a semiclassical theory (Appendix B), for fits of the spectra in Figure 4.9.

4.3. The Challenge: A Cavity Resonant on Two Atomic Transitions

The desired experiment imposes 4 nontrivial conditions onto the system:

- two atomic transitions have to be resonant to two distinct longitudinal modes of the optical cavity

- the transitions should posses different (meta-) stable ground states
- one of the transitions should form a lambda configuration with the other ground state and the additional control beam
- the atom should be strongly-coupled to the cavity light field on both transitions

The $F = 1$ and $F = 2$ states of ^{87}Rb, separated by 6.8 GHz, are well suited as ground states. They couple to the D_1 and D_2 excited state manifolds at 795 nm and 780 nm, respectively. The hyperfine splitting within these manifolds varies between 70 MHz to 800 MHz (Appendix A, Figure A.1). For our system, strong coupling may be reached on any transition for cavity lengths from 150 µm to 500 µm. This leads to a frequency spacing of neighboring TEM_{00} modes, as described by the free spectral range ν_{FSR}, between 1 THz to 0.3 THz, respectively. Since this far exceeds the separation of the hyperfine states, the four-level system has to be implemented on the fine structure split D_1 and D_2 line the difference of which amounts to 7.1 THz, about 7 to 24 FSRs.

4.3.1. Cavity Length Tuning

Several possible combinations of hyperfine states of the $5P_{1/2}$ and $5P_{3/2}$ manifold exist and the final choice of $F = 2$ to $F' = 1$ as probe transition and $F = 1$ to $F'' = 1$ as signal transition is solely based on the possibility to reach resonance for both at the same time. For that, the cavity length has to be an integer multiple of both half wavelengths:

$$l = n_a \cdot \frac{\lambda_{31}}{2} \tag{4.19a}$$

$$l = n_b \cdot \frac{\lambda_{42}}{2} \tag{4.19b}$$

where $(n_a, n_b) \in \mathbb{N}$ denote these longitudinal modes. In fact, the cavity is built out of dielectric mirrors that rely on destructive interference in the forward direction due to partial reflection at $\lambda/4$ stacks of different refractive index materials. For these so-called Bragg mirrors, the physical length l_0 has to be extended by the leakage of the optical mode into the dielectric coating δl. For wavelengths close to the center wavelength of the mirror, a first simple estimate is given by $\delta l = f \cdot \lambda$ where the penetration factor is $f = (4\Delta n)^{-1}$ with the refractive index difference Δn of the stacked materials [Bro95, Hoo01]. However, the interference of the Bragg mirrors is obviously wavelength dependent or, in other words, can only be optimized for a single wavelength, the center wavelength. As a consequence, the finesse and also the penetration depth δl vary for the eigenfrequencies of the D_1 and D_2 line. Then, the cavity length

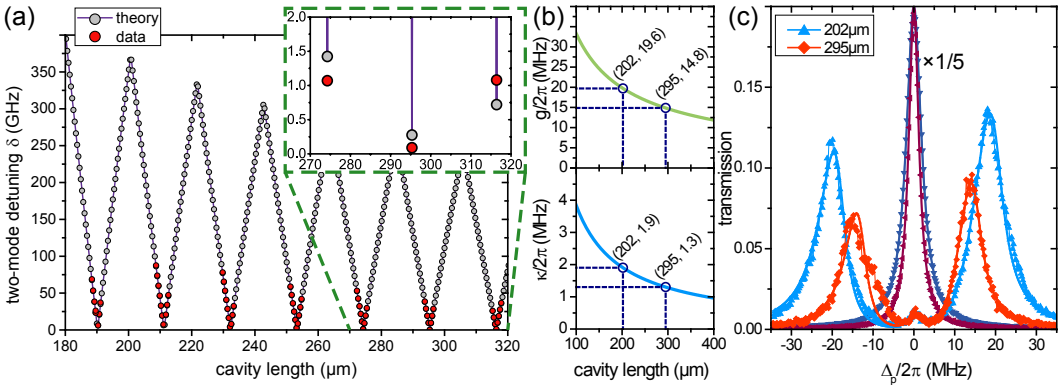

Figure 4.5.: Tuning the cavity length. (a) The two-mode detuning as a function of cavity length shows a triangle-waveform. We find a fitted penetration factor $f = 0.646(2)$. The corresponding change of the CQED parameters is shown exemplary for the cycling transition: (b) Coupling strength g and cavity field decay rate κ decrease as a function of cavity length. (c) Spectra at the old (blue) and newly found position (red) for an empty cavity (scaled by 1/5, dark) and coupled system (light) display a change in coupling strength from 19.0 MHz to 14.0 MHz and 2.0 MHz to 1.5 MHz in cavity field decay rate derived from fits of Lorentzians and a semiclassical theory (Appendix B) shown as solid lines. Both are in good agreement with theory. The relative height difference between empty cavity and coupled system results from a five-fold higher driving strength at the shorter cavity length.

$l(\nu) = l_0 + 2\delta l(\nu)$ is frequency dependent, as is the FSR $\nu_{\mathrm{FSR}}(\nu)$. This hinders a purely analytical solution and will cause deviations from the simple estimate above.

For the chosen transitions, we measure the two-mode detuning $\delta = |\Delta_{31}| + |\Delta_{42}|$ as a function of length. To this end, we increase the cavity length in steps of $\lambda_{42}/2$ to go from one to the next longitudinal mode, $n_b \to (n_b + 1)$. When resonant to the signal transition, i.e. $|\Delta_{42}| = 0$, measuring the detuning of the probe transition to the closest longitudinal mode yields $\delta = |\Delta_{31}|$. For this purpose, we monitor the transmission of two lasers at frequencies ω_{31} and ω_{42} on a single detector while scanning the cavity length around the current position. A transmission peak is observed whenever a cavity mode becomes resonant with either of the two lasers. In order to measure the two-mode detuning, the probe laser frequency is shifted to match the transmission window of the signal laser, whereby the frequency difference is tracked by a wavemeter. Figure 4.5(a) shows the two-mode detuning as a function of length. We find that the minimum detunings form a triangle-wave with a decaying amplitude $\delta_0/2\pi = \frac{\nu_{\mathrm{FSR}}}{2} = \frac{c}{4l}$ and a period given by $L = \frac{c}{2\Delta\nu_{D_1 D_2}} \approx 21\,\mu\mathrm{m}$. The former simply states that the maximum possible distance is given by the center between two longitudinal modes. The latter derives from the condition

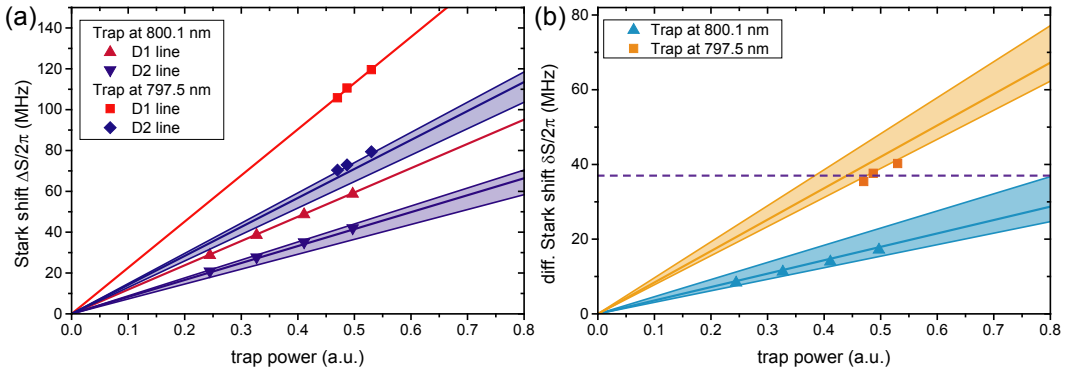

Figure 4.6.: Differential Stark shifts. (a) Dynamic Stark Shift of the probe and signal transition is depicted for trap wavelengths of 797.5 nm and 800.1 nm. Solid lines correspond to a theoretical calculation via the polarizabilities as derived by second-order perturbation theory [Neu15b]. For both wavelengths, we scale the trap power of the D_1 and D_2 theory by the same amount to match the D_1 data. The shaded area for the D_2 theory spans the shifts for different Zeeman substates due to the nonzero tensor polarizability of the $5P_{3/2}$ excited states. The center line is the weighted mean. (b) The differential Stark shift as calculated from the data and theory depicted in (a) shows that two-mode resonance (dashed line) can be reached for a trap wavelength of 797.5 nm.

that the detuning becomes minimal every time an integer multiple of the FSR is similar to the frequency difference between the lines. The two-mode detuning remains greater 1 GHz throughout the whole tuning range except for a single point at 295 µm (inset) where the splitting approaches a few 10 's of MHz and is thus just within experimental reach.

For this cavity length, the $F = 2$ to $F' = 1$ transition is only about 37 MHz red-detuned to mode A, when transition $F = 1$ to $F'' = 1$ is resonant to mode B. However, tuning the cavity length also affects the field decay rate κ and coupling strength g. In Figure 4.5(b), we show the corresponding theory curves. Finally, Figure 4.5(c) depicts the spectra for a cavity that is either empty or strongly coupled to the cycling transition of the atom at our previous length of 202 µm and the new mirror distance of 295 µm . The change is in good agreement with our theoretical expectation and shows that we still recover about 3/4th of the previous coupling strength.

4.3.2. Differential Stark shift

The residual detuning can be compensated by applying a differential light shift. As described in Section 2.2.1, the dynamic Stark effect of optical dipole traps causes energy shifts ΔS of the electronic transitions of atoms that are proportional to $\frac{\gamma}{\Delta} I$ (Equation (2.38)). Setting the red-detuned dipole trap

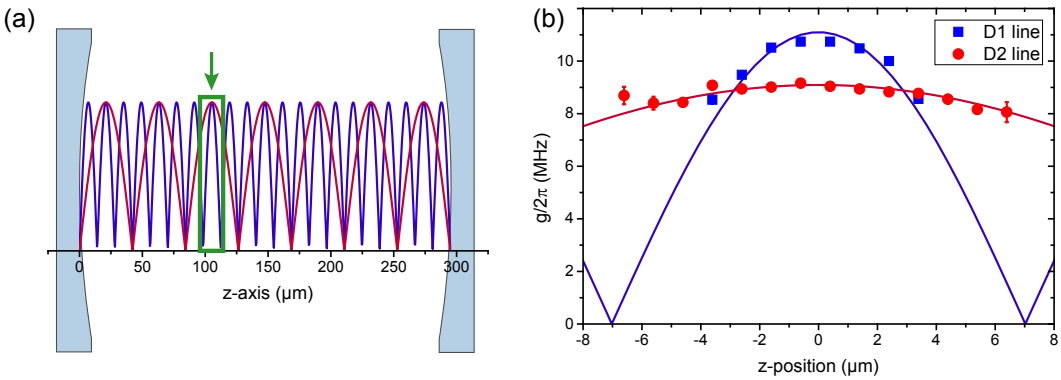

Figure 4.7.: Overlap of two cavity modes and the trap. (a) The overlap of the D_1 (blue) and D_2 (red) cavity modes with the nodes of the intracavity dipole trap is described by the detuning in number of FSRs, Δl, that amounts to 21 and 7, respectively. The green rectangle marks the presumed working region in the experiment shown as a zoom in (b). Data corresponds to the experimental coupling strengths as derived from fits of a finite temperature semiclassical model to normal mode spectra. Vertical scaling was the only free parameter for the matching theory.

closer in frequency to the D_1 than to the D_2 line, we impose a stronger shift to the former than to the latter transition, i.e. a differential light shift $\delta S = \Delta S_{31} - \Delta S_{42}$, which can be used to compensate the residual two-mode detuning. Here, ΔS_{31} (ΔS_{42}) is the dynamical Stark shift of the $|1\rangle \leftrightarrow |3\rangle$ ($|2\rangle \leftrightarrow |4\rangle$) transition due to the transverse, red-detuned dipole trap. In case Δ is chosen small compared to the fine structure splitting between D_1 and D_2, a dipole trap of reasonable power may induce substantial differential light shifts.

We perform spectroscopy of both transitions (Section 2.3.2) and record the induced Stark shift as a function of trap power [Neu15b]. Figure 4.6(a) shows the result for trapping wavelengths of 797.5 nm and 800.1 nm, thus detunings of 2.5 nm (17.3 nm) and 5.1 nm (19.9 nm) with respect to the D_1 (D_2) line. By reducing the detuning, we increase the atomic polarizability and cause much larger light shifts. Moreover, the boost of the differential shift between probe and signal transition enables us to tune both transitions resonant to their respective mode at the same time when using the transverse standing-wave dipole trap at 797.5 nm (Figure 4.6(b)).

4.3.3. Cavity Mode Overlap

The spatial overlap of different longitudinal modes has been addressed schematically in Section 2.2.1. The blue-detuned intracavity trap localizes the atoms at its nodes and these shift in overlap with respect to the resonant mode as a function of the axial position. The number of perfect in-phase and out-of-phase regions is directly described by the detuning in FSRs Δl, as depicted in

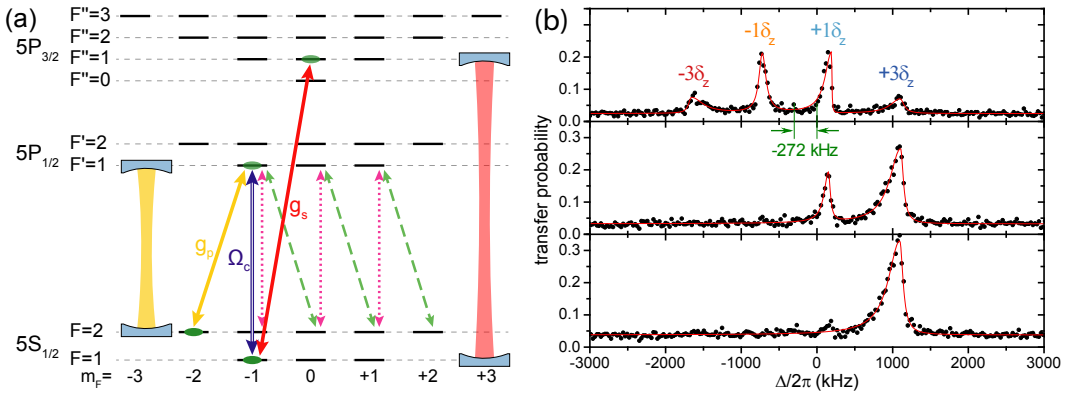

Figure 4.8.: Level scheme and state preparation. (a) The four-level system is implemented between the D_1 and D_2 line of ^{87}Rb on the Zeeman substates as indicated by the probe (yellow arrow), the signal (red arrow) and control light field (blue arrow). The green dashed and pink dotted lines indicate the important repumpers used to populate the $|2,-2\rangle$ during state preparation. (b) Raman spectroscopy drives transitions between distinct Zeeman substates (Section 2.3.3) and can be used to demonstrate the preparation of $|2,-2\rangle$ that only couples to $|1,-1\rangle$ via the transition at $+3\delta_Z$. Consequently, we observe an increasing probability of this transition and reduction of all others from unprepared (top) to only the σ^- repumper (middle) and finally σ^- and π beams. Red solid lines correspond to asymmetric Lorentz fits with different linewidths in each direction. Note the larger center shift of $-272(10)$ kHz due to the higher power of the red-detuned trap and the smaller detuning to the D_1 line compared to Figure 2.16(a).

Figure 4.7(a). The detuning between the D_1 mode and trap of $\Delta l = 21$ is particularly large. This yields a complete shift of 2π in relative phase within only 14 µm, thus imposing an axial atom position resolution around 1 µm, which is recognized as a final testbed for our 3D atom microscope (Section 2.2). In Figure 4.7(b), we show a zoom into an overlap region between probe and signal mode. Coupling strengths determined from experimental normal mode scans for both chosen transitions are plotted versus axial position. We find good agreement to a scaled theory. This clearly demonstrates our ability to localize the atoms. Comparisons to theoretical expectations in the next sections will confirm the high degree of control. Furthermore, this constitutes a tuning knob to vary the relative coupling strength of the two fields that may be useful for future experiments with degenerate couplings.

4.4. Experimental Implementation

As depicted in Figure 4.8(a), the four-level system is implemented on the Zeeman substates $|2,-2\rangle \leftrightarrow |1',-1\rangle$ for the probe and $|1,-1\rangle \leftrightarrow |1'',0\rangle$ for

the signal in order to maximize the transition matrix elements and thus the coupling strengths (Appendix A, Figure A.1). This leads to theoretical parameters of $(g_p, \kappa_a, \gamma_3)/2\pi = (10.3, 2.0, 2.9)$MHz on the probe transition and $(g_s, \kappa_b, \gamma_4)/2\pi = (9.5, 1.5, 3.0)$MHz on the signal transition, which in both cases puts us well into the strong-coupling regime of cavity QED, $g \gg (\kappa, \gamma)$.

While an atom is trapped, the measurement sequence as depicted in Figure 2.4(c) is repeated at a rate of 2 kHz. We start with a cooling interval of 460 µs followed by 20 µs of state preparation after which we probe for 5 µs to 20 µs in order to reduce depumping effects and maximize data rate. To prepare the $|2, -2\rangle$ ground state, we apply a strong left-circular and a faint linear polarized pump on $|2\rangle \leftrightarrow |1'\rangle$ that drive σ^-− and π−transitions (dashed and dotted arrows in Figure 4.8(a)). Additional beams repump atoms that end up in the $F = 1$ ground states. As a consequence, $|2, -2\rangle$ becomes the only dark ground state of the system. This is supported by investigations of the ground state population without and with different types of state preparation, as depicted in Figure 4.8(b). Only applying both, the σ^- and π, prepares the population predominantly in the $|2, -2\rangle$.

This state preparation is, however, very sensitive to the polarizations of its drives which is believed to cause a central experimental imperfection. Furthermore, the right-circularly polarized probe and signal beam during the measurement interval will inevitably pump the system out of the desired substates over time. Therefore, we keep the probing time short. However, even in short intervals the left-circularly polarized cavity mode may induce a coherent coupling via vacuum induced transparency (VIT) [TS11] to the ground states $|2, 0\rangle$ and $|1, +1\rangle$ for probe and signal, respectively. This could only be suppressed by applying strong fields to lift the two-photon resonance when differentially shifting both ground states.

The cavity drives are separated behind the cavity via interference filters. The probe passes another stage of polarization filtering that blocks any non-right-circular components. Both are then detected on two separate Hanbury Brown and Twiss detection setups consisting of two single-photon counters each with a timing resolution of 1 ns. It is ensured that this timing resolution also holds between the detection setups which allows us to perform time dependent photon cross-correlations and two-photon coincidence spectroscopy.

4.5. Results

4.5.1. Individual Subsystems

In Figure 4.9(a), we show spectra on the probe transition in absence of signal light versus $\Delta_p = \omega_p - \omega_a$. When the atom is coupled, the empty cavity Lorentzian splits into the well-known normal modes of the Jaynes-Cummings model. The residual peak at zero detuning results from the imperfections

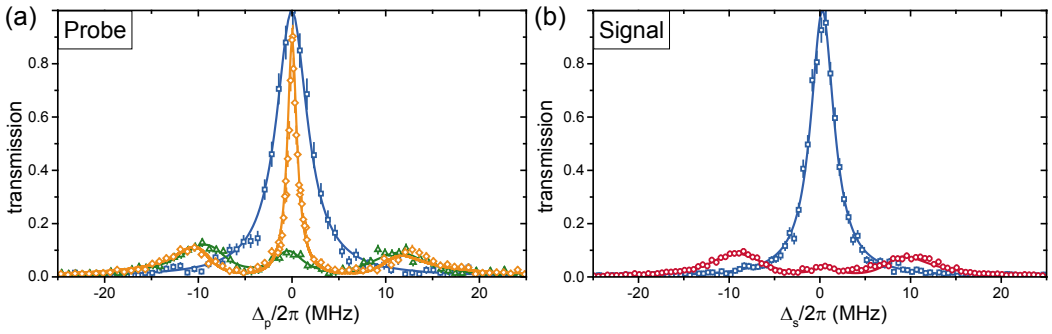

Figure 4.9.: Probe and signal spectra. (a) Experimental spectra for the probe in absence of signal light are depicted for the empty cavity (blue), normal modes of the two-level case (green) and under CEIT conditions (orange). (b) Empty cavity (blue) and normal mode splitting (red) can also be observed on the signal transition without probe and control field which proves simultaneous resonant strong coupling on two transitions. Solid lines correspond to fits of Lorentzians for bare cavities and finite-temperature, semiclassical models for CQED and cavity EIT spectra (Appendix B).

described in Section 4.4. We find $(g_p, \kappa_a, \gamma_3)/2\pi = (10.1, 2.0, 2.9)\,\mathrm{MHz}$ which puts the experiment well into the regime of strong coupling. When adding the control field at strength $\Omega_c/2\pi = 5.6\,\mathrm{MHz}$, we observe the emergence of a narrow EIT peak that amounts to almost 90 % transmission. The control field dresses the excited state and thus increases the normal mode splitting, as described by Equation (4.14). Preparing the system in state $|2\rangle$ and only driving the signal transition at $\Delta_s = \omega_s - \omega_b$, we demonstrate strong coupling with parameters $(g_s, \kappa_b, \gamma_4)/2\pi = (9.3, 1.5, 3.0)\,\mathrm{MHz}$ (Figure 4.9(b)). Again, we observe empty cavity remnants at zero detuning.

We further investigate the CEIT on the probe transition. We take several spectra for varying control Rabi frequency Ω_c and fit the two normal modes and the narrow EIT feature with three Lorentzians. As a reference for each CEIT spectrum, we also take a spectrum without control beam which yields the normal mode splitting. The center frequency of the normal modes in CEIT allows us to determine the splitting. The dressing of the normal modes, as described by Equation (4.14), is used to gauge our control field power P_c to Rabi frequency, depicted in Figure 4.10(a). It follows a clear square root behavior as expected from theory, $\Omega_c \sim \sqrt{P_c}$. The corresponding shift of the CEIT versus the CQED splitting is shown in Figure 4.10(b). The coupling strength for $\Omega_c = 0$ deviates slightly from the actual value deduced in the previous paragraph since this evaluation is influenced by small detunings between the cavity mode and atomic transition which affect the magnitude and symmetry of the splitting.

Next, we investigate the EIT transmission and contrast in Figure 4.10(c). The transmission increases for small control Rabi frequencies and settles to

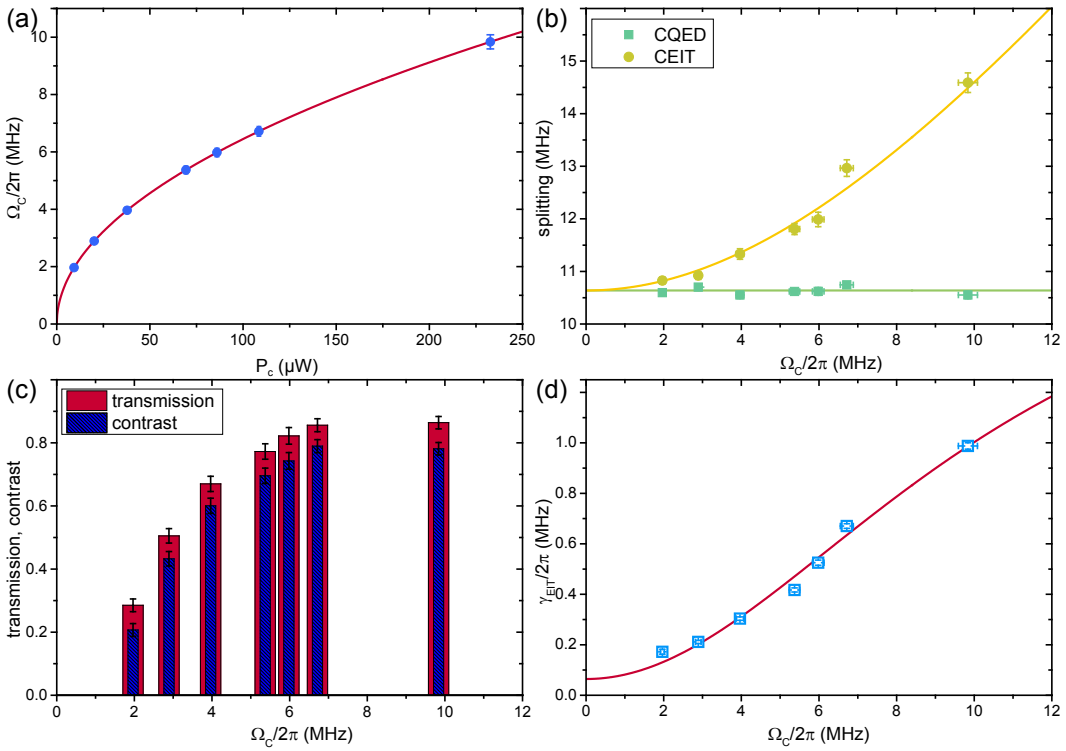

Figure 4.10.: Characterization of cavity EIT. (a) From the change of the CEIT splitting, we gauge the set control power to Rabi frequency by fitting a square root (red line) to the data. To do so, the splitting (b) is fit by Equation (4.20) in order to derive Ω_c (yellow solid line). The green data and solid line reflect the average splitting for the CQED case. We further investigate CEIT transmission and contrast, defined as the EIT transmission subtracted by the normal mode offset, (c) and linewidth (d). The red solid curve shows a fit of Equation (4.20) with only γ_d as a free parameter.

values of above 85 % with a contrast of about 80 % for $\Omega_c/2\pi > 6\,\mathrm{MHz}$. Two effects, diminish the transmission: ground state dephasing and EIT bandwidth. The EIT linewidth, thus also the bandwidth, decreases for decreasing Ω_c which, in turn, causes an increase of the time it takes to build up coherence in the system [Chi16a]:

$$\gamma_{EIT} = \frac{\kappa_a \Omega_c^2}{\Omega_c^2 + g_p^2} + \gamma_d \tag{4.20}$$

In the experiment, we keep the probing interval short to avoid depumping which means that for small control powers the system may not be able to reach full transmission. Similarly, the dephasing will limit the transmission as it becomes comparable to the EIT linewidth such that the system decoheres faster than it can build up coherence.

For a better understanding of these limitations, we investigate the EIT

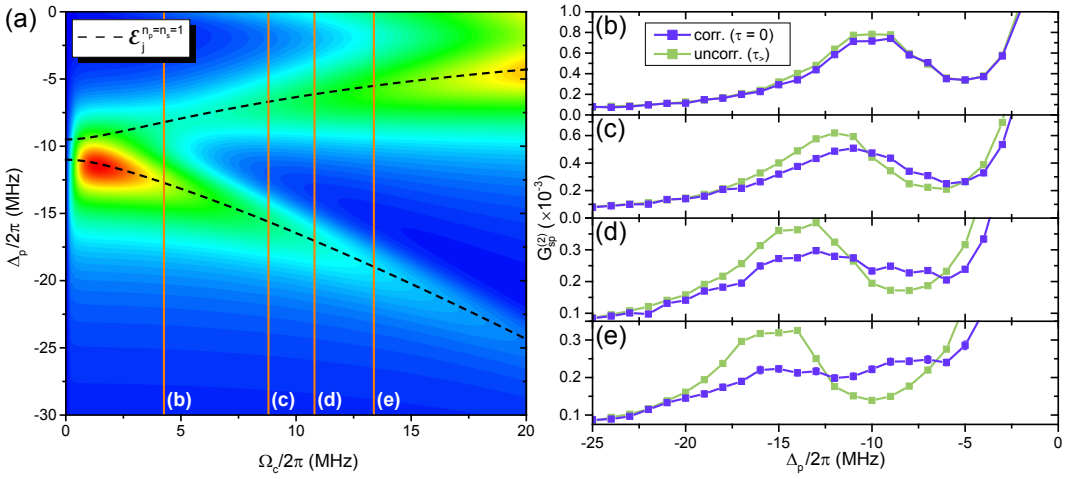

Figure 4.11.: Coincidence spectroscopy of the (1,1)-manifold. (a) Simulation of the two-photon coincidence spectrum $G^{(2)}_{sp}(0)$ versus probe detuning and control Rabi frequency based on a full quantum model. Dashed lines show the corresponding tuning of the eigenenergies of the (1,1)-manifold calculated from the analytical formula. (b)-(e) Experimental coincidence spectra at $\Omega_c = (4.3(1), 8.8(2), 10.8(3), 13.4(3))$ MHz for correlated and uncorrelated photons. For correlated data (blue) both photons are detected at the same time. Uncorrelated spectra (green) result from photons with a delay beyond the coherence times of the system.

linewidth as a function of control Rabi frequency in Figure 4.10(d). The fit of Equation (4.20) to the data using the previously determined coupling strength and known field decay rate shows good agreement and yields $\gamma_d = 64(1)$ kHz. This constitutes a significant improvement over previous results for single atom CEIT [Chi16a].

4.5.2. Resolving the (1,1)-manifold

With two cavity modes strongly coupled to the atom, we meet the criteria for strong coupling between the light fields and operate the system close to the avoided crossing ($g_p \approx g_s$). For direct demonstration of the N-type system, measurement of the interacting states with both modes populated, i.e. $n_p > 0 \wedge n_s > 0$, is required. However, spectroscopic observation of the (1,1)-manifold via $\langle \hat{n}_p \rangle$ or $\langle \hat{n}_s \rangle$ is obscured by the strong contribution of the lower rungs. In addition, excitation of multi-photon resonances is an intrinsically hard task in anharmonic systems and requires more involved techniques [Kub08, Sch08b, Fin08]. Here, we perform two-photon coincidence spectroscopy. We fix the signal detuning at $\Delta_s = 0$ and record the coincidences $G^{(2)}_{sp}(\tau = 0)$ versus probe detuning. Detecting a signal and probe photon at the same time means the system must have started at least in the (1,1)-manifold.

We expect contributions from higher rungs to be negligible since the population of both modes is kept low ($\langle \hat{n}_p \rangle , \langle \hat{n}_s \rangle) \ll 1$. In Figure 4.11(a), we show the result of a full quantum simulation for the lower two eigenstates when tuning the control field strength. As described above, the control field corresponds to the splitting between the states. Their corresponding center frequencies calculated from the analytical expression for $(n_p, n_s) = (1, 1)$ in Equation (4.11) are in good agreement with the maxima of the simulated $G^{(2)}_{sp}(0)$.

In Figure 4.11(b)-(e), we show experimental results of the $G^{(2)}_{sp}(0)$ and $G^{(2)}_{sp}(\tau_>)$ versus Δ_p for different Ω_c. Here, $\tau_>$ is large compared to the coherences of the system such that $G^{(2)}_{sp}(\tau_>)$ yields coincidences for uncorrelated photons. At weak driving, $G^{(2)}_{sp}(\tau_>)$ is sensitive to the undisturbed probe ladder. The spectra display a CEIT normal mode that shifts to larger detunings for increasing control Rabi frequency, as expected from Equation (4.14). In comparison, correlated detection shows the emergence of a shoulder at low detunings that turns into a separate maximum in Figure 4.11(e). At the same time the overall height decreases which also agrees with the simulation. A major disagreement to theory is a strong peak towards zero detuning. It originates from the residual transmission observed for the spectra at this frequency in the previous section. This residual transmission of photons not coupled to the system in conjunction with the high intensity of the EIT resonance causes a large number of false coincidences. However, the measurement constitutes the first direct observation of the tunable splitting of the (1,1)-manifold.

4.5.3. Photon-Photon Switching

Due to the strong coupling between the photons of the two light fields, displacing the average signal photon number from 0 switches the probe EIT off, as the CEIT resonance is split for $n_s \geq 1$. In Figure 4.12(a), we show a zoom into the narrow EIT peak. Increasing the signal strength indeed reduces the peak height. At the same time, we observe a small shift of its center frequency that stems from the dynamic Stark effect of the signal drive onto the ground states via neighboring transitions.

Figure 4.12(b) demonstrates that only 1.24(1) average signal photons per cavity lifetime reduce the contrast from 0.62(3) to 0.10(1) which corresponds to a switching of 84(2) %. The somewhat small starting contrast is caused by a low control power of only $\Omega_c/2\pi \approx 4\,\mathrm{MHz}$ that keeps the EIT dark state fragile. The data is in good agreement with a quantum simulation. A small deviation may be caused by the empty cavity residual already observed for the spectra and is expected to limit the switching contrast. Still, almost full switching on the level of a single photon is achieved which we expect to improve greatly when using a pulsed scheme and postselecting on the presence of a single signal photon [Che13, Bau14]. Furthermore, systematic investigations of the control Rabi frequency versus switching contrast may allow additional refinement.

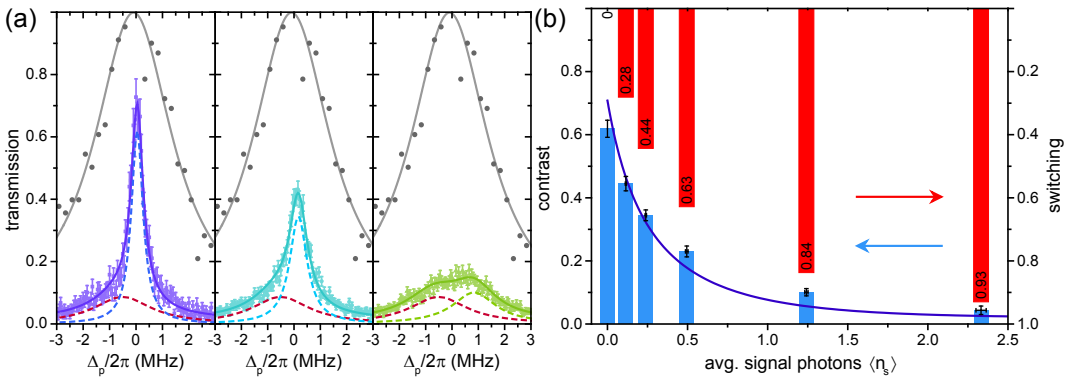

Figure 4.12.: Photon-photon switch. (a) Spectra of the narrow central EIT resonance are plotted for average signal photon numbers per cavity lifetime of $\langle \hat{n}_s \rangle = 0.0$, 0.24 and 1.24 in purple, cyan, and green, respectively. The red dashed line displays a fit to the separately measured normal mode offset which is subtracted to derive the EIT contrast (corresponding dashed lines). The sum of these yields the solid curves. The gray data and line in the back show the empty cavity and fit. As a fit function, we use Lorentzians for both, empty cavity (remnants) and EIT resonances. (b) The probe EIT contrast (blue) is plotted versus $\langle \hat{n}_s \rangle$. A switching (red), i.e. the relative decrease of the contrast, of 84(2) % for $\langle \hat{n}_s \rangle = 1.24(1)$ is achieved. The solid curve results from a quantum simulation according to Section 4.2.3 only using the independently determined parameters from Section 4.5.1.

4.5.4. Mutual Blocking and Conjunct Transit

In the previous section, signal photons switch off the probe. Conversely, the probe, however, also blocks the signal light, since the (1,1)-manifold describes a splitting for both fields. This causes anticorrelation between the fields. We keep both driving strengths low, i.e. $\langle \hat{n}_p \rangle = \langle \hat{n}_s \rangle = 0.02$, and perform a second order cross-correlation $g^{(2)}_{sp}(\tau)$ of the two fields at $\Delta_p = \Delta_s = 0$. As anticipated, we observe pronounced antibunching with $g^{(2)}_{sp}(0) = 0.29(2)$ demonstrating that the probability to detect a signal and probe photon at the same time is strongly suppressed (Figure 4.13). For negative delays, the $g^{(2)}_{sp}(\tau)$ is proportional to the probability of measuring a signal photon with time delay τ upon detection of a probe photon. The correlation increases to 1, i.e. the value for uncorrelated photons, on the time scale required to build up a field in the empty cavity: $(\kappa_b)^{-1}$. For $\tau > 0$, the signal photon triggers the correlation and the slope to equilibration is dominated by the EIT bandwidth of the probe [Bec14]. As a consequence, increasing Ω_c steepens the slope. The behavior is in good agreement with our quantum simulation.

The small average photon number for both beams leads to a negligible coincidence probability of about 0.04 % and consequently the self-correlations $g^{(2)}_{ss}(\tau)$ and $g^{(2)}_{pp}(\tau)$ are barely affected by the presence of the other field. We find

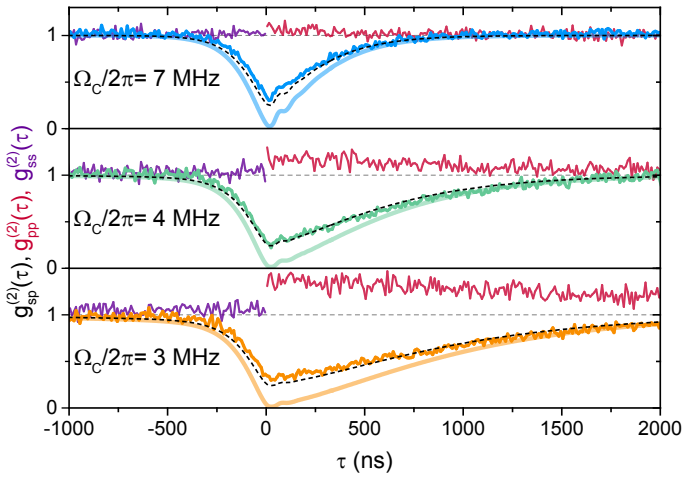

Figure 4.13.: Mutual photon blocking. The second order time dependent cross-correlation at zero cavity detunings $\Delta_p = \Delta_s = 0$ for varying control field strengths displays strong anticorrelation and thus mutual blocking between the fields. Red (purple) data shows the corresponding probe (signal) self-correlations. Bright solid curves correspond to results of a full quantum simulation. Black dashed lines show the same theory scaled by a factor of 0.77 around 1 which yields good quantitative agreement for all three values of the control Rabi frequency.

that even though interactions between photons of different fields are strong, photons of the same field show hardly any correlation. This is in perfect agreement with the expectation for an empty cavity field (signal) or a coherent dark state (probe). The latter displays a slightly bunched behavior that is stronger for lower control Rabi frequency and results from finite ground state coherence. This reduces the EIT transmission and admixes features of the two-level CQED system that exhibits bunching at this frequency. In addition, the probe photon is slowed considerably at small control strengths and its transit time diverges for vanishing Ω_c, ultimately causing the interaction probability with signal photons to become significant.

The observed anticorrelation stems from the splitting of the (1,1)-manifold. When tuning either of the two fields to the new resonances, we expect to find correlated transmission. In Figure 4.14, we show cross-correlations for different detunings of the signal light while keeping the probe at $\Delta_p = 0$ and $\langle \hat{n}_p \rangle = 0.02$, and increasing $\langle \hat{n}_s \rangle$ to 0.2 in order to compensate for the lower incoupling. With increasing detuning, we observe the emergence of oscillations. Their frequency is given by the signal detuning $(\Delta_s)^{-1}$ for negative and the effective probe coupling $(g_{p,eff})^{-1}$ for positive times which results from interference between each drive and the decay paths via either the signal EIT resonance or the dressed states of the probe, respectively. At zero time delay, the fields change from anti- to correlated transmission where signal and

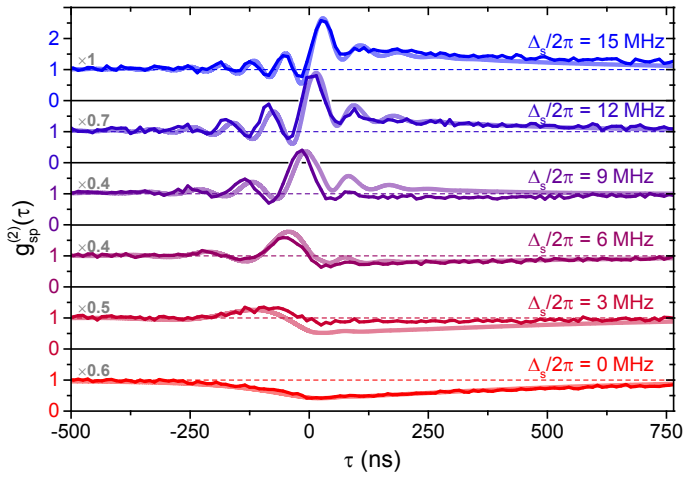

Figure 4.14.: Conjunct photon transit. Varying Δ_s while keeping $\Delta_p = 0$ allows tuning of the second order time dependent cross-correlation from mutual blocking to conjunct transit of photons indicated by high correlation. Ω_c is set to 4 MHz. The theory (light curves) is scaled by the factor to the left (gray) around 1.

probe photons only transit the system conjunctly. The strongest bunching occurs at $\Delta_s/2\pi \approx 10$ MHz in good agreement with the new eigenenergies of the (1,1)-manifold.

In summary, photons of the same color display no interaction while they couple strongly to photons of the other field causing either mutual blocking or conjunct transit. Overall good agreement between data and a theory without accounting for imperfections demonstrates good control over the system.

4.6. Conclusion

In summary, we have theoretically described and experimentally demonstrated strong coupling between two light fields via interaction with a four-level atom. First direct evidence of the energy structure arranged in quadruplets is observed via coincidence spectroscopy. We show photon-photon switching and strong correlations between the two light fields without self-correlation. Outstanding challenges are the observation of the avoided crossing and demonstration of the nonlinear behavior for $(n_p, n_s) > (1, 1)$. Future applications of the system include a switch or transistor [Che13] or a quantum phase gate [Li15].

Furthermore, in case of conjunct transit, the detection of a signal photon heralds the presence of probe photons in the other mode and vice-versa. Exploiting the system's inherent nonlinearity due to strong coupling between the photons could in future experiments enable selective excitation of a specific manifold, e.g., the (n,1). This realizes a heralded n-photon source where de-

tection of a signal photon announces n photons in the probe mode.

Another potential application of the system is non-destructive photon counting that requires undisturbed propagation of the photons to be sensed. This condition is met for dispersive coupling of the signal where the respective cavity mode is detuned from the atomic transition [Sch07, Gue07]. In such a scenario, photons in that signal mode induce a linear photon-number dependent light shift on ground state $|2\rangle$, leading to a distinct shift in the two-photon detuning of the narrow EIT resonance between probe and control beam. Detecting this shift of the dark state via the probe amounts to non-destructive counting of signal photons, another example of all-optical quantum-nonlinear sensing. For best performance, a matching of photon transit times through the system catalyzing the interaction seems inevitable.

Moreover, instead of using two modes of one cavity, crossed single-mode cavities could be employed. These allow individually tuning modes into resonance with emitter transitions at widely separated wavelengths, thus providing a pathway to all-optical sensing for example of quantum communication photons at telecom wavelengths for which good counters are not available [Uph16].

Finally, using linear probe and signal pulses, a double N-type system can be realized: The probe lambda EIT is implemented on the D_2 line with $|1,0\rangle$ as $|1\rangle$ coupled via the excited states $|1'',\pm1\rangle$ to both ground states $|2,-2\rangle$ and $|2,+2\rangle$ that serve as $|2\rangle$. Here, choosing a proper linear polarization of the control with respect to the probe suppresses coupling to $|2,0\rangle$ via destructive interference. The signal then couples the ground states $|2,\pm2\rangle$ to excited states $|1',\pm1\rangle$. This leads to the two N-type arms of (i) σ^+ probe with σ^- signal and (ii) σ^- probe with σ^+ signal. In the regime of mutual blocking, only probe and signal photons that each couple to a different arm are simultaneously transmitted which creates polarization-entangled photons useful for quantum communication.

5. Summary and Outlook

In the course of this thesis, full control over the internal and external degrees of freedom of the atom was achieved. Many steps were required to reaching this goal: An imaging system was constructed [Eck13] and implemented to detect the fluorescence of atoms. The real-time imaging allows monitoring the presence of atoms independent of their coupling to the cavity, which is an indispensable tool when going beyond Jaynes-Cummings physics with two-level atoms [Chi16a]. In addition, it enables direct detection of the number of trapped atoms and their position. Moreover, the extension of the system by two additional transverse dipole traps [Tie14b] and the transition from an active feedback-based cooling to a passive Sisyphus-type scheme have lead to three-dimensional confinement of atoms close to the motional ground state. In addition, this extended the atom's trapping time to about 8 s, a more than sevenfold improvement over previous results [Koc10]. Particularly, the results on 3D microscopy of atoms and subsequent control of their exact position in space are of central importance for realizing an almost ideal CQED system. The reliable and efficient preparation of atoms with an average coupling strength of 97 % of the theory value in unison with a more performant experimental control system [BS15] has drastically reduced the measurement time of, for example, spectra from hours to minutes. With this positioning at hand, precise measurement of dipole trap-induced Stark shifts of the electronic transitions, Zeeman shifts of the ground states due to magnetic fields and the preparation of magnetic substates have been performed at this apparatus for the first time.

The new level of control enabled recording of high-quality, second- and third-order photon correlations with trapped atoms in the regime of low driving. Using those correlations, two-photon blockade, i.e. truncation of the Hilbert space at $n = 2$ quanta, was demonstrated [Ham17]. This constitutes the first example of a blockade at $n > 1$ photons and, thus, goes beyond simple single-photon nonlinearities that are already observable with a single atom in free space. It shows the unique capabilities of a CQED system for n-photon quantum-nonlinear optics. Central to its success was the realization that unwanted excitation to higher manifolds can be suppressed by driving the atom instead of the cavity that suffers from bosonic enhancement. While a natural extension is attempting a blockade at $n = 3$ or more photons, a reduction of the contribution from single photon events could turn the two-photon blockade into a two-photon source. For example, a two-photon gateway [Kub08] and

photon-induced tunneling [Far08] in case of cavity driving have been demonstrated to enhance population of higher manifolds, in accordance with our own results.

Finally, strong coupling between photons of two light fields was demonstrated in an N-type CQED system. Here, two transitions of a four-level atom are simultaneously strongly coupled to two distinct cavity modes that are driven by initially uncorrelated fields, probe and signal. An additional control laser induces a tunable interaction between the modes. It is shown that the resulting energy level structure is arranged in quadruplets that can be expressed in terms of new coupling strengths of the joint system. Their splittings depend nonlinearly on the number of photons in each of the modes, n_p and n_s, which causes the strong coupling between the fields.

The general system has been initially envisioned 20 years ago [Ima97], but remained experimentally challenging due to the requirement of resonance of two modes to two transitions. Here, two-mode resonance is reached for the first time by tuning the cavity length and applying a differential Stark shift to the two transitions. It is demonstrated that the system catalyzes interactions between photons of different fields in two regimes by either mutual blocking or conjunct transit, while photons in the same mode do not interact. Furthermore, a photon-photon switch between the fields is realized.

The strong coupling of fields opens the route to quantum nonlinear all-optical sensing. Here, correlations between, for instance, the photon numbers in the two fields are used to directly measure photons with photons. Among other applications, a potential first step is exploiting the doubly nonlinear energy ladder to selectively excite a state with $n_p = n$ and $n_s = 1$, such that detection of one signal photon heralds n probe photons. This potentially requires the previously developed atom driving for both fields to avoid unwanted excitation to higher-lying states. Furthermore, moderate detuning could facilitate selective addressing of one specific state, as has been demonstrated for the CQED system [Sch08b, Fin08]. The resulting heralded n-photon source may be demonstrated via correlations up to $(n+1)$th order of the probe triggered by a signal photon.

A. Numbers and Equations

name	symbol	unit	value	formula	comment
mirror 1: high reflection, incoupling mirror					
curvature	R_1	cm	20	–	
transmittance	T_1	ppm	2.5(5)	–	at 780 nm
		ppm	5.0(5)	–	at 772 nm
losses	L_1	ppm	5.5(5)	–	
coned diameter	D_1	mm	2	–	
mirror 2: outcoupling mirror					
curvature	R_2	cm	1	–	
transmittance	T_2	ppm	17.8(5)	–	at 780 nm
		ppm	21.0(5)	–	at 772 nm
losses	L_2	ppm	5.5(5)	–	
coned diameter	D_2	mm	1.5	–	
finesse	$\mathcal{F}$	10^3	195(2)	$\frac{2\pi}{T_1+T_2+L_1+L_2}$	at 780 nm
		10^3	170(5)		at 772 nm
cavity length	L	mm	0.1 to 1	–	variable
penetration depth	δL	nm		$\frac{\lambda}{4\Delta n}$	
cavity field decay	κ	2π MHz	–	$\frac{c\pi}{2L\mathcal{F}}$	variable
free spectral range	ν_{FSR}	THz	0.15 to 1.50	$\frac{c}{2L}$	variable
mode waist	w_0	µm	15 to 28	$\sqrt[4]{\frac{\lambda^2}{\pi^2}\frac{LR_1R_2}{R_1+R_2}}$	variable[1]
Rayleigh range	z_R	mm	0.9 to 3.2	$\frac{\pi\omega_0^2}{\lambda}$	variable
mode volume	V	µm^3	–	$\frac{\pi L w_0^2}{4}$	variable
optical power	P_0	W	–	–	
electric field amp.	E_0	V m^{-1}	–	$\sqrt{\frac{2I}{c\epsilon_0}}$	

[1] only true for $L \ll (R_1, R_2)$

name	symbol	unit	value	formula	comment
intensity	I	$\mathrm{W\,cm^{-2}}$	–	$\frac{2P_0}{\pi\omega_0^2}$	running[2]
				$\frac{8P_0}{\pi\omega_0^2}$	standing[2]
				$\frac{8P_0}{T_2\pi\omega_0^2}$	intracavity[3]
efficiencies					
outcoupling	η_o	–	0.57(3)	$\frac{T_2}{T_1+T_2+L_1+L_2}$	at 780 nm
detector	η_{det}	–	0.65(5)	–	specified
fiber coupling	η_{fc}	–	0.8(1)	–	
optical elem.	η_i	–	0.95 to 0.99	–	filters, ...
detection	η_d	–	≈ 0.5	$\eta_{det}\eta_{fc}\prod_i \eta_i$	
count rate	Γ_d	MHz	–	$\frac{I}{\hbar\omega}$	
				$2\kappa\eta_o\eta_d \langle\hat{n}\rangle$	
^{87}Rb					
mass	m	10^{-25} kg	1.443	–	
trans. dipole mom.	d	$10^{-29}\,\mathrm{C\,m}$	2.534(3)	–	cycl. trans.[4]
D_1 line frequency	ω_{D_1}	2π THz	377.107	–	
D_2 line frequency	ω_{D_2}	2π THz	384.230	–	
Rabi frequency	Ω	2π MHz	–	$\frac{d\cdot E_0}{\hbar}$	
spatial mode func.	$f_m(\mathbf{r})$	–	–	$\cos(kz)e^{-\frac{x^2+y^2}{w_0^2}}$	
coupling constant	g	2π MHz	–	$\sqrt{\frac{\omega_f d^2}{2\hbar V\epsilon_0}}$	variable
spat. coupl. const.	$g(\mathbf{r})$	2π MHz	–	$g\cdot f_m(\mathbf{r})$	variable
cooperativity	$\mathcal{C}$	–	–	$\frac{g^2}{2\kappa\gamma}$	variable
critical atom num.	N_0	–	–	$\mathcal{C}^{-1}$	variable
critical photon num.	n_0	–	–	$\frac{\gamma^2}{2g^2}$	variable
trapping potential	U_t	k_B·mK	–	$-\frac{1}{2}\alpha\lvert\mathbf{E}\rvert^2$	–
polarizability	α	$\mathrm{Cm^2/V}$	–	$\frac{3\pi c^3\epsilon_0}{\omega_a^3}\frac{\gamma}{\Delta}$	simple TLS[5]

[2] wave for a Gaussian beam.

[3] relates the power behind the cavity to the intracavity intensity.

[4] For other transitions obtained by multiplication with the Clebsch-Gordan coefficients.

[5] Quantitative results should be calculated by a multi-level theory taking the large atomic energy structure into account as elaborated in great detail by [Neu15a].

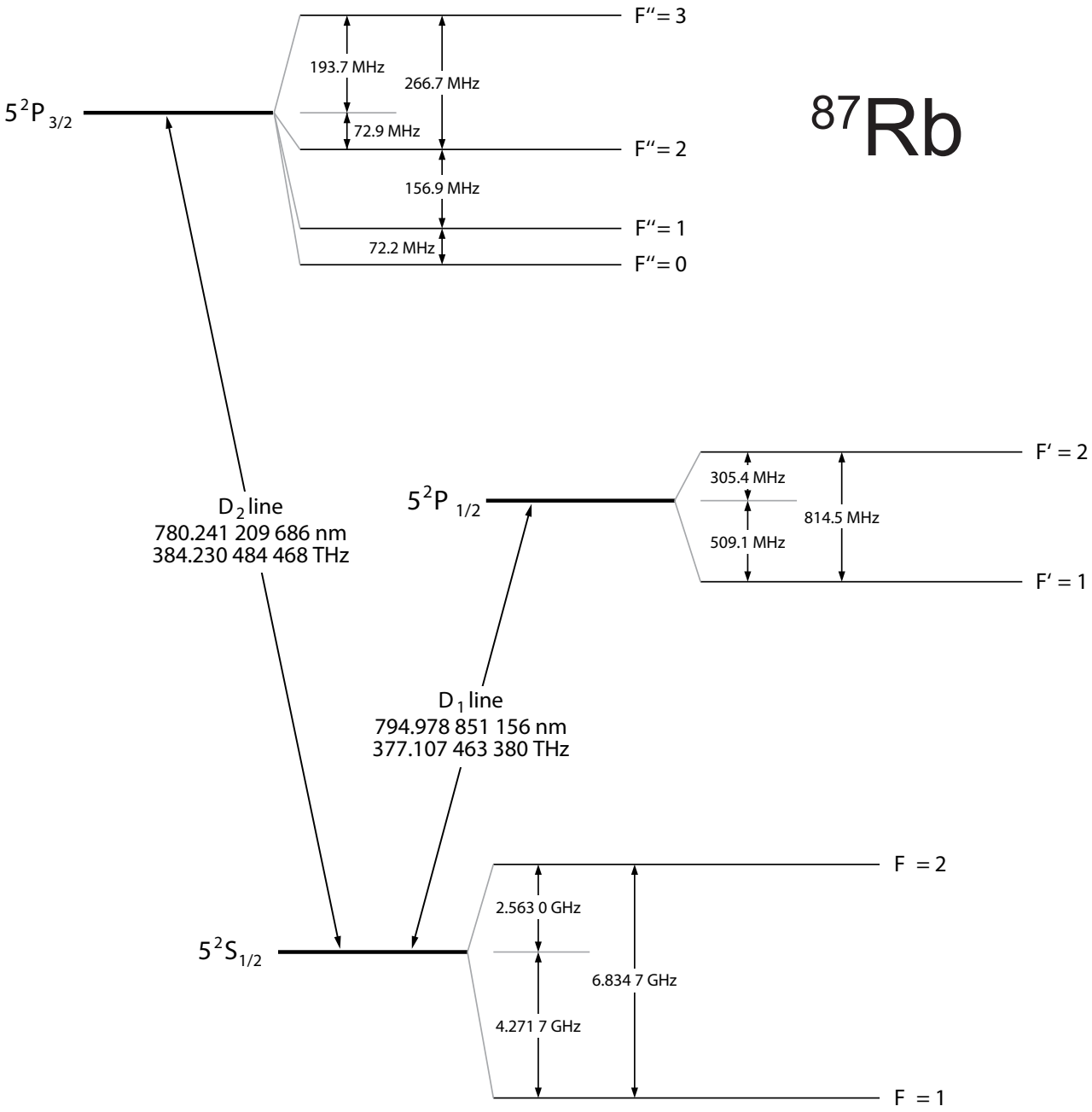

Figure A.1.: Hyperfine transitions of ^{87}Rb . Full ^{87}Rb *D* line data taken from [Ste03]. Illustration modified from [Eck13].

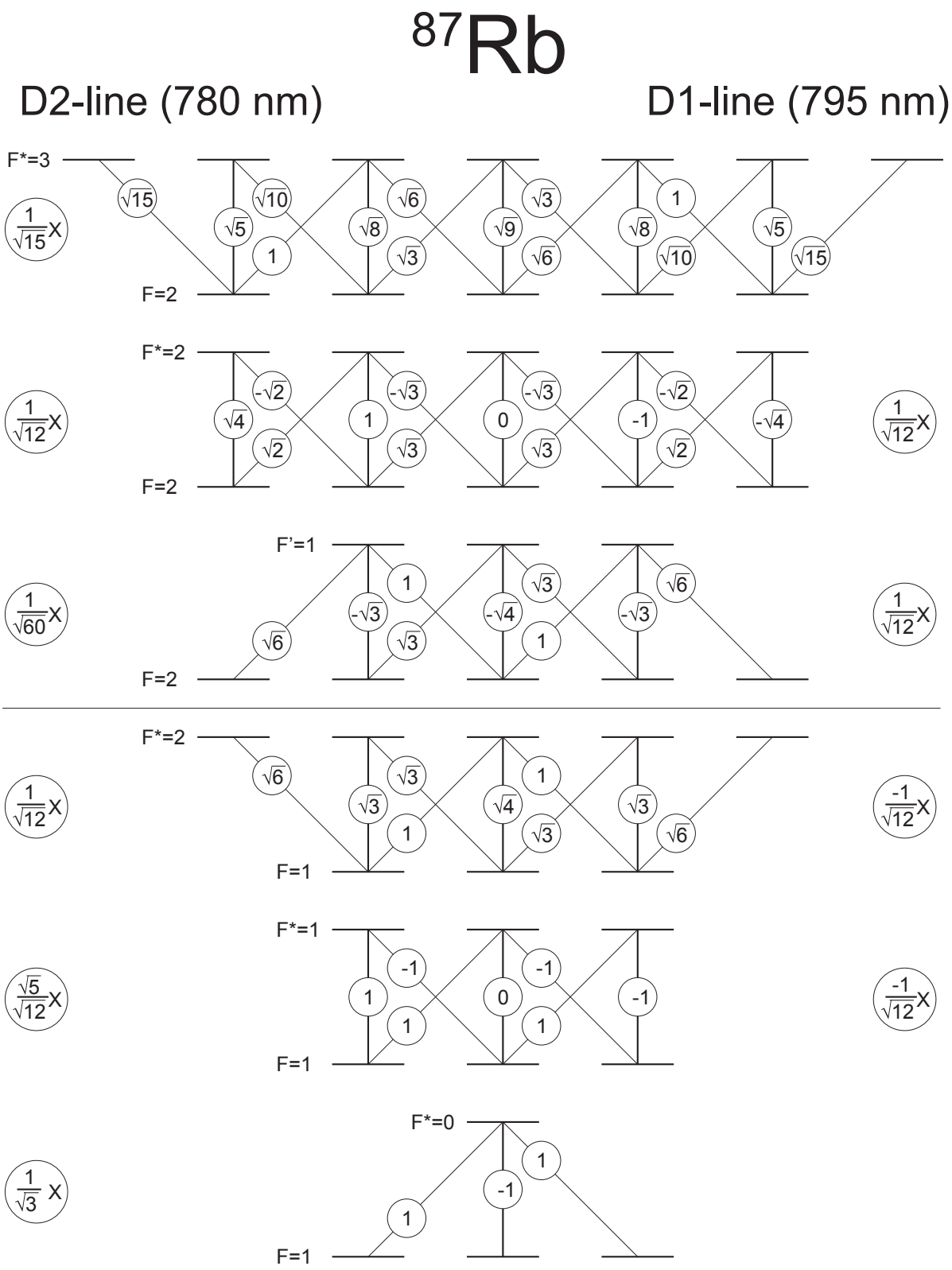

Figure A.2.: Clebsch-Gordan coefficients of ^{87}Rb . Clebsch-Gordan coefficients for the D lines of ^{87}Rb are taken and modified from Dr. Stephan Dürr. The general sign conventions follow [Edm60].

B. Semiclassical Spectral Functions

In Section 2.1, we developed a theory to calculate the outcomes for the observables of a quantum system including dissipation. From the Lindblad master equation (Equation (2.29)), one can find the equation of motion of an operator $\hat{O}$ defined as $\partial_t \langle \hat{O} \rangle = \mathrm{tr}(\hat{O}\dot{\rho})$ [Sch08a, Müc11]. This leads to a set of coupled differential equations for the operators describing the atomic excitation and population of the cavity field, which can in general not be solved analytically. Numerical solutions of the full quantum system are, however, often computationally intensive and consequently unsuitable for efficient fitting of experimental spectra.

On the other hand, in most of these spectra for the CQED and CEIT system, we keep the driving strength low. Under the assumption of a resulting low atomic excitation, one can then attempt a semiclassical solution. Following the ideas of References [Luk03] and [Müc10], it is possible to calculate the mean photon number for CEIT using the definitions of Section 4.2:

$$\langle n_p \rangle = \frac{|\eta_p|^2}{|(\Delta_p + i\kappa_a) - \chi|^2} \tag{B.1}$$

Here, χ is the complex linear susceptibility of an EIT medium. In the limit of a single atom, it takes the form:

$$\chi = \frac{g_p^2 \left(\Delta_p + \Delta_{31} - \Delta_c + i\gamma_d\right)}{(\Delta_p + \Delta_{31} + i\gamma_3)(\Delta_p + \Delta_{31} - \Delta_c + i\gamma_d) - \Omega_c^2} \tag{B.2}$$

Using this formula, for example the fit to the CEIT spectrum in Figure 4.9(a) was performed.

When $\Omega_c = 0$, one recovers the solution for the CQED system from Equation (B.1) as given in Reference [Mur03]. For the probe CQED system, it yields:

$$\langle n_p \rangle = \frac{\eta_p^2 \left|(\Delta_p + \Delta_{31} + i\gamma_{31})\right|^2}{\left|(\Delta_p + i\kappa_a)\left(\Delta_p + \Delta_{31} + i\gamma_{31}\right) - g_p^2\right|^2} \tag{B.3}$$

Likewise, we we can find a similar solution for the case when the drive η_p is

applied to the atom which was used in Chapter 3 [Sch08a, Ham17]:

$$\langle n_p \rangle = \frac{\eta_p^2 g^2}{\left| (\Delta_p + i\kappa_a)(\Delta_p + \Delta_{31} + i\gamma_{31}) - g_p^2 \right|^2} \tag{B.4}$$

Finally, we may also take the effects of atomic motion into account. Due to the light shifts of the optical dipole traps, finite temperature T of the atom causes an inhomogeneous broadening of the atomic resonance which in turn affects the spectrum. This can be modeled by averaging over Boltzmann-distributed atomic detunings as described in the supplementary material of Reference [Neu15a]. The model, however, assumes one steady state temperature for the whole spectrum, while in our system the drive is the main source of heating which in turn depends strongly on the driving strength and detuning [Mau05].

To incorporate the effects of imperfect state preparation or probe polarization, we add an additional term to the analytical normal mode formula. We use a Lorentzian of amplitude A and width $2\kappa_a$ centered at zero detuning.

In summary, this model is for example applied to fit the CQED spectra in Figures 2.9, 3.5 and 4.9 using the driving and coupling strengths, atom-cavity detunings, temperatures, and amplitudes as free parameters.

Bibliography

[Alb11] Albert, M., Dantan, A., and Drewsen, M. Cavity electromagnetically induced transparency and all-optical switching using ion Coulomb crystals. *Nature Photonics* **5**, 633 (2011).

[Als91] Alsing, P. and Carmichael, H. J. Spontaneous dressed-state polarization of a coupled atom and cavity mode. *Quantum Optics: Journal of the European Optical Society Part B* **3**, 13 (1991).

[Als92] Alsing, P., Guo, D.-S., and Carmichael, H. J. Dynamic Stark effect for the Jaynes-Cummings system. *Physical Review A* **45**, 5135 (1992).

[Baj09] Bajcsy, M., Hofferberth, S., Balić, V., Peyronel, T., Hafezi, M., Zibrov, A. S., Vuletić, V., and Lukin, M. D. Efficient All-Optical Switching Using Slow Light within a Hollow Fiber. *Physical Review Letters* **102**, 203902 (2009).

[Bar73] Barger, R. L., Sorem, M., and Hall, J. Frequency stabilization of a cw dye laser. *Applied Physics Letters* **22**, 573 (1973).

[Bau14] Baur, S., Tiarks, D., Rempe, G., and Dürr, S. Single-Photon Switch Based on Rydberg Blockade. *Physical Review Letters* **112**, 073901 (2014).

[Bec14] Beck, K. M., Chen, W., Lin, Q., Gullans, M., Lukin, M. D., and Vuletić, V. Cross Modulation of Two Laser Beams at the Individual-Photon Level. *Physical Review Letters* **113**, 113603 (2014).

[Ber86] Bergquist, J. C., Hulet, R. G., Itano, W. M., and Wineland, D. J. Observation of Quantum Jumps in a Single Atom. *Physical Review Letters* **57**, 1699 (1986).

[Ber98] Bergmann, K., Theuer, H., and Shore, B. W. Coherent population transfer among quantum states of atoms and molecules. *Reviews of Modern Physics* **70**, 1003 (1998).

[Ber06] Bermel, P., Rodriguez, A., Johnson, S. G., Joannopoulos, J. D., and Soljačić, M. Single-photon all-optical switching using waveguide-cavity quantum electrodynamics. *Physical Review A* **74**, 043818 (2006).

[Bir05a] Birnbaum, K. M., Boca, A., Miller, R., Boozer, A. D., Northup, T. E., and Kimble, H. J. Photon blockade in an optical cavity with one trapped atom. *Nature* **436**, 87 (2005).

[Bir05b] Birnbaum, K. M., Boca, A., Miller, R., Boozer, A. D., Northup, T. E., and Kimble, H. J. Theory of Photon Blockade by an Optical Cavity with One Trapped Atom. *arXiv:0507065 [quant-ph]* (2005).

[Bis09] Bishop, L. S., Chow, J. M., Koch, J., Houck, A. A., Devoret, M. H., Thuneberg, E., Girvin, S. M., and Schoelkopf, R. J. Nonlinear response of the vacuum Rabi resonance. *Nature Physics* **5**, 105 (2009).

[Blu17] Blums, V., Piotrowski, M., Hussain, M. I., Norton, B. G., Connell, S. C., Gensemer, S., Lobino, M., and Streed, E. W. A single-atom 3D sub-attonewton force sensor. *arXiv:1703.06561 [quant-ph]* (2017).

[Boc04] Boca, A., Miller, R., Birnbaum, K. M., Boozer, A. D., McKeever, J., and Kimble, H. J. Observation of the Vacuum Rabi Spectrum for One Trapped Atom. *Physical Review Letters* **93**, 233603 (2004).

[Boc10] Bochmann, J., Mücke, M., Guhl, C., Ritter, S., Rempe, G., and Moehring, D. L. Lossless State Detection of Single Neutral Atoms. *Physical Review Letters* **104**, 203601 (2010).

[Boh13] Bohr, N. On the constitution of atoms and molecules. *Philosophical Magazine Series 6* **26**, 857 (1913).

[Boo08] Boozer, A. D. Theory of Raman transitions in cavity QED. *Physical Review A* **78**, 033406 (2008).

[Bra03] Braje, D., Balić, V., Yin, G., and Harris, S. Low-light-level nonlinear optics with slow light. *Physical Review A* **68**, 041801 (2003).

[Bra11] Braak, D. Integrability of the Rabi Model. *Physical Review Letters* **107**, 100401 (2011).

[Bro95] Brovelli, L. and Keller, U. Simple analytical expressions for the reflectivity and the penetration depth of a Bragg mirror between arbitrary media. *Optics Communications* **116**, 343 (1995).

[BS15] Bernard-Schwarz, M., Field Programmable Gate Arrays as control tools in quantum optics experiments, Dissertation, Technische Universität Wien (2015).

[Bul11] Buluta, I., Ashhab, S., and Nori, F. Natural and artificial atoms for quantum computation. *Reports on Progress in Physics* **74**, 104401 (2011).

[Bus17] Busche, H., Huillery, P., Ball, S. W., Ilieva, T., Jones, M. P. A., and Adams, C. S. Contactless nonlinear optics mediated by long-range Rydberg interactions. *Nature Physics* **13**, 655 (2017).

[Car76] Carmichael, H. J. and Walls, D. F. A quantum-mechanical master equation treatment of the dynamical Stark effect. *Journal of Physics B: Atomic and Molecular Physics* **9**, 1199 (1976).

[Car93] Carmichael, H. J. An Open Systems Approach to Quantum Optics, *Lecture Notes in Physics Monographs*, volume 18. Springer, Berlin, Heidelberg (1993).

[Car96] Carmichael, H. J., Kochan, P., and Sanders, B. C. Photon Correlation Spectroscopy. *Physical Review Letters* **77**, 631 (1996).

[Car08] Carmichael, H. J. Cavity QED: Signs of anharmonicity. *Nature Physics* **4**, 346 (2008).

[Car09] Carmichael, H. J. Statistical Methods in Quantum Optics 2: Non-Classical Fields. Springer, Berlin, Heidelberg (2009).

[Car15] Carmichael, H. J. Breakdown of Photon Blockade: A Dissipative Quantum Phase Transition in Zero Dimensions. *Physical Review X* **5**, 031028 (2015).

[Cha14] Chang, D. E., Vuletić, V., and Lukin, M. D. Quantum nonlinear optics - photon by photon. *Nature Photonics* **8**, 685 (2014).

[Che05] Chen, Y.-F., Tsai, Z.-H., Liu, Y.-C., and Yu, I. A. Low-light-level photon switching by quantum interference. *Optics Letters* **30**, 3207 (2005).

[Che06] Chen, Y.-F., Wang, C.-Y., Wang, S.-H., and Yu, I. A. Low-Light-Level Cross-Phase-Modulation Based on Stored Light Pulses. *Physical Review Letters* **96**, 043603 (2006).

[Che13] Chen, W., Beck, K. M., Bucker, R., Gullans, M., Lukin, M. D., Tanji-Suzuki, H., and Vuletić, V. All-Optical Switch and Transistor Gated by One Stored Photon. *Science* **341**, 768 (2013).

[Chi16a] Chibani, H., Photon Blockade with Memory and Slow Light using a Single Atom in an Optical Cavity, Dissertation, Technische Universität München (2016).

[Chi16b] Chikkaraddy, R., de Nijs, B., Benz, F., Barrow, S. J., Scherman, O. A., Rosta, E., Demetriadou, A., Fox, P., Hess, O., and Baumberg, J. J. Single-molecule strong coupling at room temperature in plasmonic nanocavities. *Nature* **535**, 127 (2016).

[Col07] Colombe, Y., Steinmetz, T., Dubois, G., Linke, F., Hunger, D., and Reichel, J. Strong atom-field coupling for Bose-Einstein condensates in an optical cavity on a chip. *Nature* **450**, 272 (2007).

[Dal89] Dalibard, J. and Cohen-Tannoudji, C. Laser cooling below the Doppler limit by polarization gradients: simple theoretical models. *Journal of the Optical Society of America B* **6**, 2023 (1989).

[Day08] Dayan, B., Parkins, A. S., Aoki, T., Ostby, E. P., Vahala, K. J., and Kimble, H. J. A Photon Turnstile Dynamically Regulated by One Atom. *Science* **319**, 1062 (2008).

[Dep08] Deppe, F., Mariantoni, M., Menzel, E. P., Marx, A., Saito, S., Kakuyanagi, K., Tanaka, H., Meno, T., Semba, K., Takayanagi, H., Solano, E., and Gross, R. Two-photon probe of the Jaynes-Cummings model and controlled symmetry breaking in circuit QED. *Nature Physics* **4**, 686 (2008).

[Dev07] Devoret, M., Girvin, S., and Schoelkopf, R. Circuit-QED: How strong can the coupling between a Josephson junction atom and a transmission line resonator be? *Annalen der Physik* **16**, 767 (2007).

[Die87] Diedrich, F. and Walther, H. Nonclassical radiation of a single stored ion. *Physical Review Letters* **58**, 203 (1987).

[Dre83] Drever, R. W. P., Hall, J. L., Kowalski, F. V., Hough, J., Ford, G. M., Munley, a. J., and Ward, H. Laser phase and frequency stabilization using an optical resonator. *Applied Physics B Photophysics and Laser Chemistry* **31**, 97 (1983).

[Dua04] Duan, L.-M. and Kimble, H. J. Scalable Photonic Quantum Computation through Cavity-Assisted Interactions. *Physical Review Letters* **92**, 127902 (2004).

[Eck13] Eckl, A. C., High-Resolution Imaging of a Single Atom Strongly Coupled to a Cavity, Master thesis, Ludwig-Maximilians Universität (2013).

[Edm60] Edmonds, A. R. Angular Momentum in Quantum Mechanics. Princeton University Press, Princeton, 2nd edition (1960).

[Ein05] Einstein, A. Über einen die Erzeugung und Verwandlung des Lichtes betreffenden heuristischen Gesichtspunkt. *Annalen der Physik* **322**, 132 (1905).

[Ein35] Einstein, A., Podolsky, B., and Rosen, N. Can Quantum-Mechanical Description of Physical Reality Be Considered Complete? *Physical Review* **47**, 777 (1935).

[Far08] Faraon, A., Fushman, I., Englund, D., Stoltz, N., Petroff, P., and Vučković, J. Coherent generation of non-classical light on a chip via photon-induced tunnelling and blockade. *Nature Physics* **4**, 859 (2008).

[Fei15] Feizpour, A., Hallaji, M., Dmochowski, G., and Steinberg, A. M. Observation of the nonlinear phase shift due to single post-selected photons. *Nature Physics* **11**, 905 (2015).

[Fey85] Feynman, R. P. QED: The Strange Theory of Light and Matter. Alix G. Mautner memorial lectures., Princeton University Press, Princeton (1985).

[Fin08] Fink, J. M., Göppl, M., Baur, M., Bianchetti, R., Leek, P. J., Blais, A., and Wallraff, A. Climbing the Jaynes-Cummings ladder and observing its nonlinearity in a cavity QED system. *Nature* **454**, 315 (2008).

[Fin10] Finlay, C. C., et al. International Geomagnetic Reference Field: the eleventh generation. *Geophysical Journal International* **183**, 1216 (2010).

[Fir13] Firstenberg, O., Peyronel, T., Liang, Q.-Y., Gorshkov, A. V., Lukin, M. D., and Vuletić, V. Attractive photons in a quantum nonlinear medium. *Nature* **502**, 71 (2013).

[Fle05] Fleischhauer, M., İmamoğlu, A., and Marangos, J. P. Electromagnetically induced transparency: Optics in coherent media. *Reviews of Modern Physics* **77**, 633 (2005).

[Foo05] Foot, C. J. Atomic Physics. Oxford University Press, Oxford (2005).

[Fuh11] Fuhrmanek, A., Bourgain, R., Sortais, Y. R. P., and Browaeys, A. Free-Space Lossless State Detection of a Single Trapped Atom. *Physical Review Letters* **106**, 133003 (2011).

[Geh10] Gehr, R., Volz, J., Dubois, G., Steinmetz, T., Colombe, Y., Lev, B. L., Long, R., Estève, J., and Reichel, J. Cavity-Based Single Atom Preparation and High-Fidelity Hyperfine State Readout. *Physical Review Letters* **104**, 203602 (2010).

[Gle07] Gleyzes, S., Kuhr, S., Guerlin, C., Bernu, J., Deléglise, S., Busk Hoff, U., Brune, M., Raimond, J.-M., and Haroche, S. Quantum jumps of light recording the birth and death of a photon in a cavity. *Nature* **446**, 297 (2007).

[Gri00] Grimm, R., Weidemüller, M., and Ovchinnikov, Y. B., Optical Dipole Traps for Neutral Atoms, in Advances In Atomic, Molecular, and Optical Physics, pp. 95–170 (2000).

[Gue07] Guerlin, C., Bernu, J., Deléglise, S., Sayrin, C., Gleyzes, S., Kuhr, S., Brune, M., Raimond, J.-M., and Haroche, S. Progressive field-state collapse and quantum non-demolition photon counting. *Nature* **448**, 889 (2007).

[Gut01] Guthöhrlein, G. R., Keller, M., Hayasaka, K., Lange, W., and Walther, H. A single ion as a nanoscopic probe of an optical field. *Nature* **414**, 49 (2001).

[Hac16] Hacker, B., Welte, S., Rempe, G., and Ritter, S. A photon-photon quantum gate based on a single atom in an optical resonator. *Nature* **536**, 193 (2016).

[Ham17] Hamsen, C., Tolazzi, K. N., Wilk, T., and Rempe, G. Two-Photon Blockade in an Atom-Driven Cavity QED System. *Physical Review Letters* **118**, 133604 (2017).

[Han13] Han, R., Khoon Ng, H., and Englert, B.-G. Raman transitions without adiabatic elimination: a simple and accurate treatment. *Journal of Modern Optics* **60**, 255 (2013).

[Har89] Haroche, S. and Kleppner, D. Cavity Quantum Electrodynamics. *Physics Today* **42**, 24 (1989).

[Har90] Harris, S. E., Field, J. E., and İmamoğlu, A. Nonlinear optical processes using electromagnetically induced transparency. *Physical Review Letters* **64**, 1107 (1990).

[Har06] Haroche, S. and Raimond, J. Exploring the Quantum: atoms, cavities and photons. Oxford University Press (2006).

[Har10] Harlander, M., Brownnutt, M., Hänsel, W., and Blatt, R. Trapped-ion probing of light-induced charging effects on dielectrics. *New Journal of Physics* **12**, 093035 (2010).

[Hei27] Heisenberg, W. Über den anschaulichen Inhalt der quantentheoretischen Kinematik und Mechanik. *Zeitschrift für Physik* **43**, 172 (1927).

[Hei90] Heinzen, D. J. and Wineland, D. J. Quantum-limited cooling and detection of radio-frequency oscillations by laser-cooled ions. *Physical Review A* **42**, 2977 (1990).

[Hen00] Hennrich, M., Legero, T., Kuhn, A., and Rempe, G. Vacuum-Stimulated Raman Scattering Based on Adiabatic Passage in a High-Finesse Optical Cavity. *Physical Review Letters* **85**, 4872 (2000).

[Hof11] Hoffman, A. J., Srinivasan, S. J., Schmidt, S., Spietz, L., Aumentado, J., Türeci, H. E., and Houck, A. A. Dispersive Photon Blockade in a Superconducting Circuit. *Physical Review Letters* **107**, 053602 (2011).

[Hoo98] Hood, C. J., Chapman, M. S., Lynn, T. W., and Kimble, H. J. Real-Time Cavity QED with Single Atoms. *Physical Review Letters* **80**, 4157 (1998).

[Hoo00] Hood, C. J., Lynn, T. W., Doherty, A. C., Parkins, A. S., and Kimble, H. J. The Atom-Cavity Microscope: Single Atoms Bound in Orbit by Single Photons. *Science* **287**, 1447 (2000).

[Hoo01] Hood, C. J., Kimble, H. J., and Ye, J. Characterization of high-finesse mirrors: Loss, phase shifts, and mode structure in an optical cavity. *Physical Review A* **64**, 033804 (2001).

[Hos16] Hosseini, M., Beck, K. M., Duan, Y., Chen, W., and Vuletić, V. Partially Nondestructive Continuous Detection of Individual Traveling Optical Photons. *Physical Review Letters* **116**, 033602 (2016).

[Ima97] Imamoglu, A., Schmidt, H., Woods, G., and Deutsch, M. Strongly Interacting Photons in a Nonlinear Cavity. *Physical Review Letters* **79**, 1467 (1997).

[Imo85] Imoto, N., Haus, H. A., and Yamamoto, Y. Quantum nondemolition measurement of the photon number via the optical Kerr effect. *Physical Review A* **32**, 2287 (1985).

[Ita90] Itano, W. M., Heinzen, D. J., Bollinger, J. J., and Wineland, D. J. Quantum Zeno effect. *Physical Review A* **41**, 2295 (1990).

[Jay63] Jaynes, E. and Cummings, F. Comparison of quantum and semiclassical radiation theories with application to the beam maser. *Proceedings of the IEEE* **51**, 89 (1963).

[Joh13] Johansson, J., Nation, P., and Nori, F. QuTiP 2: A Python framework for the dynamics of open quantum systems. *Computer Physics Communications* **184**, 1234 (2013).

[Kas91] Kasevich, M. and Chu, S. Atomic interferometry using stimulated Raman transitions. *Physical Review Letters* **67**, 181 (1991).

[Kat15] Kato, S. and Aoki, T. Strong Coupling between a Trapped Single Atom and an All-Fiber Cavity. *Physical Review Letters* **115**, 093603 (2015).

[Kau12] Kaufman, A. M., Lester, B. J., and Regal, C. A. Cooling a Single Atom in an Optical Tweezer to Its Quantum Ground State. *Physical Review X* **2**, 041014 (2012).

[Ker00] Kerman, A. J., Vuletić, V., Chin, C., and Chu, S. Beyond Optical Molasses: 3D Raman Sideband Cooling of Atomic Cesium to High Phase-Space Density. *Physical Review Letters* **84**, 439 (2000).

[Kim77] Kimble, H. J., Dagenais, M., and Mandel, L. Photon Antibunching in Resonance Fluorescence. *Physical Review Letters* **39**, 691 (1977).

[Kim08] Kimble, H. J. The quantum internet. *Nature* **453**, 1023 (2008).

[Koc10] Koch, M., Sames, C., Kubanek, A., Apel, M., Balbach, M., Ourjoumtsev, A., Pinkse, P. W. H., and Rempe, G. Feedback Cooling of a Single Neutral Atom. *Physical Review Letters* **105**, 173003 (2010).

[Koc11a] Koch, M., Classical and Quantum Dynamics of a Strongly Coupled Atom-Cavity System, Dissertation, Technische Universität München (2011).

[Koc11b] Koch, M., Sames, C., Balbach, M., Chibani, H., Kubanek, A., Murr, K., Wilk, T., and Rempe, G. Three-Photon Correlations in a Strongly Driven Atom-Cavity System. *Physical Review Letters* **107**, 023601 (2011).

[Kok10] Kok, P. and Lovett, B. W. Introduction to Optical Quantum Processing. Cambridge University Press, Cambridge (2010).

[Kub08] Kubanek, A., Ourjoumtsev, A., Schuster, I., Koch, M., Pinkse, P. W. H., Murr, K., and Rempe, G. Two-Photon Gateway in One-Atom Cavity Quantum Electrodynamics. *Physical Review Letters* **101**, 203602 (2008).

[Kub09] Kubanek, A., Koch, M., Sames, C., Ourjoumtsev, A., Pinkse, P. W. H., Murr, K., and Rempe, G. Photon-by-photon feedback control of a single-atom trajectory. *Nature* **462**, 898 (2009).

[Kub10] Kubanek, A., Two-photon gateway and feedback control of a single atom in a cavity, Dissertation, Technische Universität München (2010).

[Lan11] Lang, C., Bozyigit, D., Eichler, C., Steffen, L., Fink, J. M., Abdumalikov, A. A., Baur, M., Filipp, S., da Silva, M. P., Blais, A., and Wallraff, A. Observation of Resonant Photon Blockade at Microwave Frequencies Using Correlation Function Measurements. *Physical Review Letters* **106**, 243601 (2011).

[Lax63] Lax, M. Formal Theory of Quantum Fluctuations from a Driven State. *Physical Review* **129**, 2342 (1963).

[Le 16] Le Kien, F. and Rauschenbeutel, A. Nanofiber-based all-optical switches. *Physical Review A* **93**, 013849 (2016).

[Lee14] Lee, M., Kim, J., Seo, W., Hong, H.-G., Song, Y., Dasari, R. R., and An, K. Three-dimensional imaging of cavity vacuum with single atoms localized by a nanohole array. *Nature Communications* **5**, 3441 (2014).

[Lei03] Leibfried, D., Blatt, R., Monroe, C., and Wineland, D. Quantum dynamics of single trapped ions. *Reviews of Modern Physics* **75**, 281 (2003).

[Les14] Lester, B. J., Kaufman, A. M., and Regal, C. A. Raman cooling imaging: Detecting single atoms near their ground state of motion. *Physical Review A* **90**, 011804 (2014).

[Li15] Li, R. B., Zhu, C. J., Deng, L., and Hagley, E. W. Zero to π continuously controllable cross-phase modulation in a Doppler-broadened N-type electromagnetically-induced-transparency medium. *Physical Review A* **92**, 043838 (2015).

[Luk03] Lukin, M. D. Colloquium : Trapping and manipulating photon states in atomic ensembles. *Reviews of Modern Physics* **75**, 457 (2003).

[Mai60] Maiman, T. H. Stimulated Optical Radiation in Ruby. *Nature* **187**, 493 (1960).

[Man95] Mandel, L. and Wolf, E. Optical coherence and quantum optics. Cambridge University Press, Cambridge (1995).

[Mau05] Maunz, P., Puppe, T., Schuster, I., Syassen, N., Pinkse, P. W. H., and Rempe, G. Normal-Mode Spectroscopy of a Single-Bound-Atom-Cavity System. *Physical Review Letters* **94**, 033002 (2005).

[Max65] Maxwell, J. C. A Dynamical Theory of the Electromagnetic Field. *Philosophical Transactions of the Royal Society of London* **155**, 459 (1865).

[Mey07] Meystre, P. and Sargent, M. Elements of Quantum Optics. Springer, Berlin, Heidelberg (2007).

[Mie98] Mielke, S. L., Foster, G. T., and Orozco, L. A. Nonclassical Intensity Correlations in Cavity QED. *Physical Review Letters* **80**, 3948 (1998).

[Mir13] Miranowicz, A., Paprzycka, M., Liu, Y.-X., Bajer, J., and Nori, F. Two-photon and three-photon blockades in driven nonlinear systems. *Physical Review A* **87**, 023809 (2013).

[Mis77] Misra, B. and Sudarshan, E. C. G. The Zeno's paradox in quantum theory. *Journal of Mathematical Physics* **18**, 756 (1977).

[Mon95] Monroe, C., Meekhof, D. M., King, B. E., Itano, W. M., and Wineland, D. J. Demonstration of a Fundamental Quantum Logic Gate. *Physical Review Letters* **75**, 4714 (1995).

[Müc10] Mücke, M., Figueroa, E., Bochmann, J., Hahn, C., Murr, K., Ritter, S., Villas-Boas, C. J., and Rempe, G. Electromagnetically induced transparency with single atoms in a cavity. *Nature* **465**, 755 (2010).

[Müc11] Mücke, M., Elektromagnetisch induzierte Transparenz mit einem einzelnen Atom, Dissertation, Technische Universität München (2011).

[Mul10] Muller, A., Flagg, E. B., Lawall, J. R., and Solomon, G. S. Ultrahigh-finesse, low-mode-volume Fabry-Perot microcavity. *Optics Letters* **35**, 2293 (2010).

[Muñ14] Muñoz, C. S., del Valle, E., Tudela, A. G., Müller, K., Lichtmannecker, S., Kaniber, M., Tejedor, C., Finley, J. J., and Laussy, F. P. Emitters of N-photon bundles. *Nature Photonics* **8**, 550 (2014).

[Mur03] Murr, K. On the suppression of the diffusion and the quantum nature of a cavity mode. Optical bistability: forces and friction in driven cavities. *Journal of Physics B: Atomic, Molecular and Optical Physics* **36**, 2515 (2003).

[Mur06] Murr, K., Nußmann, S., Puppe, T., Hijlkema, M., Weber, B., Webster, S. C., Kuhn, A., and Rempe, G. Three-dimensional cavity cooling and trapping in an optical lattice. *Physical Review A* **73**, 063415 (2006).

[Nag86] Nagourney, W., Sandberg, J., and Dehmelt, H. Shelved optical electron amplifier: Observation of quantum jumps. *Physical Review Letters* **56**, 2797 (1986).

[Neu80] Neuhauser, W., Hohenstatt, M., Toschek, P. E., and Dehmelt, H. Localized visible Ba^+ mono-ion oscillator. *Physical Review A* **22**, 1137 (1980).

[Neu15a] Neuzner, A., Resoance Fluorescence of an Atom Pair in an Optical Resonator, Dissertation, Technische Universität München (2015).

[Neu15b] Neuzner, A., Körber, M., Dürr, S., Rempe, G., and Ritter, S. Breakdown of atomic hyperfine coupling in a deep optical-dipole trap. *Physical Review A* **92**, 053842 (2015).

[Neu16] Neuzner, A., Körber, M., Morin, O., Ritter, S., and Rempe, G. Interference and dynamics of light from a distance-controlled atom pair in an optical cavity. *Nature Photonics* **10**, 303 (2016).

[Nod07] Noda, S., Fujita, M., and Asano, T. Spontaneous-emission control by photonic crystals and nanocavities. *Nature Photonics* **1**, 449 (2007).

[Nog99] Nogues, G., Rauschenbeutel, A., Osnaghi, S., Brune, M., Raimond, J. M., and Haroche, S. Seeing a single photon without destroying it. *Nature* **400**, 239 (1999).

[Nuß05a] Nußmann, S., Hijlkema, M., Weber, B., Rohde, F., Rempe, G., and Kuhn, A. Submicron Positioning of Single Atoms in a Microcavity. *Physical Review Letters* **95**, 173602 (2005).

[Nuß05b] Nußmann, S., Murr, K., Hijlkema, M., Weber, B., Kuhn, A., and Rempe, G. Vacuum-stimulated cooling of single atoms in three dimensions. *Nature Physics* **1**, 122 (2005).

[Our11] Ourjoumtsev, A., Kubanek, A., Koch, M., Sames, C., Pinkse, P. W. H., Rempe, G., and Murr, K. Observation of squeezed light from one atom excited with two photons. *Nature* **474**, 623 (2011).

[Phi98] Phillips, W. D. Nobel Lecture: Laser cooling and trapping of neutral atoms. *Reviews of Modern Physics* **70**, 721 (1998).

[Pin00] Pinkse, P. W. H., Fischer, T., Maunz, P., and Rempe, G. Trapping an atom with single photons. *Nature* **404**, 365 (2000).

[Pla00] Planck, M. K. E. L. Zur Theorie des Gesetzes der Energieverteilung im Normalspectrum. *Verhandl. Dtsc. Phys. Ges.* **2**, 237 (1900).

[Pur46] Purcell, E. M. Spontaneous Emission Probabilities at Radio Frequencies. *Physical Review* **69**, 674 (1946).

[Raa87] Raab, E. L., Prentiss, M., Cable, A., Chu, S., and Pritchard, D. E. Trapping of Neutral Sodium Atoms with Radiation Pressure. *Physical Review Letters* **59**, 2631 (1987).

[Ram28] Raman, C. V. A new radiation. *Indian Journal of Physics* **2**, 387 (1928).

[Rau99] Rauschenbeutel, A., Nogues, G., Osnaghi, S., Bertet, P., Brune, M., Raimond, J. M., and Haroche, S. Coherent Operation of a Tunable Quantum Phase Gate in Cavity QED. *Physical Review Letters* **83**, 5166 (1999).

[Reb99] Rebić, S., Tan, S. M., Parkins, A. S., and Walls, D. F. Large Kerr nonlinearity with a single atom. *Journal of Optics B* **1**, 490 (1999).

[Reb02] Rebić, S., Parkins, A. S., and Tan, S. M. Polariton analysis of a four-level atom strongly coupled to a cavity mode. *Physical Review A* **65**, 043806 (2002).

[Rei04] Reithmaier, J. P., Sek, G., Löffler, A., Hofmann, C., Kuhn, S., Reitzenstein, S., Keldysh, L. V., Kulakovskii, V. D., Reinecke, T. L., and Forchel, A. Strong coupling in a single quantum dot-semiconductor microcavity system. *Nature* **432**, 197 (2004).

[Rei12] Reinhard, A., Volz, T., Winger, M., Badolato, A., Hennessy, K. J., Hu, E. L., and İmamoğlu, A. Strongly correlated photons on a chip. *Nature Photonics* **6**, 93 (2012).

[Rei13] Reiserer, A., Ritter, S., and Rempe, G. Nondestructive Detection of an Optical Photon. *Science* **342**, 1349 (2013).

[Rei14] Reiserer, A., Kalb, N., Rempe, G., and Ritter, S. A quantum gate between a flying optical photon and a single trapped atom. *Nature* **508**, 237 (2014).

[Rei15] Reiserer, A. and Rempe, G. Cavity-based quantum networks with single atoms and optical photons. *Reviews of Modern Physics* **87**, 1379 (2015).

[Rem87] Rempe, G., Walther, H., and Klein, N. Observation of quantum collapse and revival in a one-atom maser. *Physical Review Letters* **58**, 353 (1987).

[Rem91] Rempe, G., Thompson, R. J., Brecha, R. J., Lee, W. D., and Kimble, H. J. Optical bistability and photon statistics in cavity quantum electrodynamics. *Physical Review Letters* **67**, 1727 (1991).

[Rit12] Ritter, S., Nölleke, C., Hahn, C., Reiserer, A., Neuzner, A., Uphoff, M., Mücke, M., Figueroa, E., Bochmann, J., and Rempe, G. An elementary quantum network of single atoms in optical cavities. *Nature* **484**, 195 (2012).

[Ros11] Rosenblum, S., Parkins, A. S., and Dayan, B. Photon routing in cavity QED: Beyond the fundamental limit of photon blockade. *Physical Review A* **84**, 033854 (2011).

[Ros15] Rosenblum, S., Bechler, O., Shomroni, I., Lovsky, Y., Guendelman, G., and Dayan, B. Extraction of a single photon from an optical pulse. *Nature Photonics* **10**, 19 (2015).

[Rot08] Rotter, D., Mukherjee, M., Dubin, F., and Blatt, R. Monitoring a single ion's motion by second-order photon correlations. *New Journal of Physics* **10**, 043011 (2008).

[Run14] Rundquist, A., Bajcsy, M., Majumdar, A., Sarmiento, T., Fischer, K., Lagoudakis, K. G., Buckley, S., Piggott, A. Y., and Vučković, J. Nonclassical higher-order photon correlations with a quantum dot strongly coupled to a photonic-crystal nanocavity. *Physical Review A* **90**, 023846 (2014).

[Sam14] Sames, C., Chibani, H., Hamsen, C., Altin, P. A., Wilk, T., and Rempe, G. Antiresonance Phase Shift in Strongly Coupled Cavity QED. *Physical Review Letters* **112**, 043601 (2014).

[Sau86] Sauter, T., Neuhauser, W., Blatt, R., and Toschek, P. E. Observation of Quantum Jumps. *Physical Review Letters* **57**, 1696 (1986).

[Sch26] Schrödinger, E. An Undulatory Theory of the Mechanics of Atoms and Molecules. *Physical Review* **28**, 1049 (1926).

[Sch35a] Schrödinger, E. Die gegenwärtige Situation in der Quantenmechanik. *Die Naturwissenschaften* **23**, 807 (1935).

[Sch35b] Schrödinger, E. and Born, M. Discussion of Probability Relations between Separated Systems. *Mathematical Proceedings of the Cambridge Philosophical Society* **31**, 555 (1935).

[Sch52] Schrödinger, E. Are there quantum jumps? *The British Journal for the Philosophy of Science* **III**, 233 (1952).

[Sch07] Schuster, D. I., Houck, A. A., Schreier, J. A., Wallraff, A., Gambetta, J. M., Blais, A., Frunzio, L., Majer, J., Johnson, B., Devoret, M. H., Girvin, S. M., and Schoelkopf, R. J. Resolving photon number states in a superconducting circuit. *Nature* **445**, 515 (2007).

[Sch08a] Schuster, I., Nonlinear spectroscopy of a single-atom-cavity system, Dissertation, Technische Universität München (2008).

[Sch08b] Schuster, I., Kubanek, A., Fuhrmanek, A., Puppe, T., Pinkse, P. W. H., Murr, K., and Rempe, G. Nonlinear spectroscopy of photons bound to one atom. *Nature Physics* **4**, 382 (2008).

[Sha10] Shamailov, S. S., Parkins, A. S., Collett, M. J., and Carmichael, H. J. Multi-photon blockade and dressing of the dressed states. *Optics Communications* **283**, 766 (2010).

[Sou13] Souza, J. A., Figueroa, E., Chibani, H., Villas-Boas, C. J., and Rempe, G. Coherent Control of Quantum Fluctuations Using Cavity Electromagnetically Induced Transparency. *Physical Review Letters* **111**, 113602 (2013).

[Ste03] Steck, D. A., Rubidium 87 D Line Data, Reference data, Los Alamos National Laboratory (2003).

[Ste16] Steil, M., The Ultimate Game Boy Talk, in 33c3: works for me, Chaos Computer Club, Hamburg (2016).

[Tan99] Tan, S. M. A computational toolbox for quantum and atomic optics. *Journal of Optics B: Quantum and Semiclassical Optics* **1**, 424 (1999).

[Tan15] Tang, J., Geng, W., and Xu, X. Quantum Interference Induced Photon Blockade in a Coupled Single Quantum Dot-Cavity System. *Scientific Reports* **5**, 9252 (2015).

[Tem11] Tempel, D. G. and Aspuru-Guzik, A. Relaxation and dephasing in open quantum systems time-dependent density functional theory: Properties of exact functionals from an exactly-solvable model system. *Chemical Physics* **391**, 130 (2011).

[Tho98] Thompson, R. J., Turchette, Q. A., Carnal, O., and Kimble, H. J. Nonlinear spectroscopy in the strong-coupling regime of cavity QED. *Physical Review A* **57**, 3084 (1998).

[Tho17] Thompson, J. D., Nicholson, T. L., Liang, Q.-Y., Cantu, S. H., Venkatramani, A. V., Choi, S., Fedorov, I. A., Viscor, D., Pohl, T., Lukin, M. D., and Vuletić, V. Symmetry-protected collisions between strongly interacting photons. *Nature* **542**, 206 (2017).

[Tie14a] Tiecke, T. G., Thompson, J. D., de Leon, N. P., Liu, L. R., Vuletić, V., and Lukin, M. D. Nanophotonic quantum phase switch with a single atom. *Nature* **508**, 241 (2014).

[Tie14b] Tietje, I. C., Localisation of a single atom inside an optical cavity, Master thesis, Technische Universität Berlin (2014).

[TS11] Tanji-Suzuki, H., Chen, W., Landig, R., Simon, J., and Vuletić, V. Vacuum-induced transparency. *Science* **333**, 1266 (2011).

[Uph16] Uphoff, M., Brekenfeld, M., Rempe, G., and Ritter, S. An integrated quantum repeater at telecom wavelength with single atoms in optical fiber cavities. *Applied Physics B* **122**, 46 (2016).

[Vah03] Vahala, K. J. Optical microcavities. *Nature* **424**, 839 (2003).

[Wal92] Walther, H. Experiments on cavity quantum electrodynamics. *Physics Reports* **219**, 263 (1992).

[Wal04] Wallraff, A., Schuster, D. I., Blais, A., Frunzio, L., Huang, R.-S., Majer, J., Kumar, S., Girvin, S. M., and Schoelkopf, R. J. Strong coupling of a single photon to a superconducting qubit using circuit quantum electrodynamics. *Nature* **431**, 162 (2004).

[Wal06] Walther, H., Varcoe, B. T. H., Englert, B.-G., and Becker, T. Cavity quantum electrodynamics. *Reports on Progress in Physics* **69**, 1325 (2006).

[Wer99] Werner, M. J. and İmamoğlu, A. Photon-photon interactions in cavity electromagnetically induced transparency. *Physical Review A* **61**, 011801 (1999).

[Wes99] Wester, M. J. Computer Algebra Systems: A Practical Guide. John Wiley and Sons, Chichester (1999).

[Yan01] Yan, M., Rickey, E. G., and Zhu, Y. Observation of absorptive photon switching by quantum interference. *Physical Review A* **64**, 041801 (2001).

List of Publications

- **Strong Coupling between Photons of Two Light Fields mediated by One Atom**
  C. Hamsen, K.N. Tolazzi, T. Wilk, and G. Rempe
  Submitted

- **Quantum Nonlinear Four-Wave Mixing with a Single Atom in an Optical Cavity**
  In preparation

- **Continuous Parametric Feedback Cooling of a Single Atom in an Optical Cavity**
  In preparation

- **Two-Photon Blockade in an Atom-Driven Cavity QED System**
  C. Hamsen, K.N. Tolazzi, T. Wilk, and G. Rempe
  Physical Review Letters **118**, 133604 (2017)

- **Antiresonance Phase Shift in Strongly Coupled Cavity QED**
  C. Sames, H. Chibani, C. Hamsen, P.A. Altin, T. Wilk, and G. Rempe
  Physical Review Letters **112**, 043601 (2014)

Acknowledgments

My years in the Quantum Dynamics division of the Max Planck Institute of Quantum Optics were paved with many precious moments. I want to express my gratitude to the unique people who made these moments possible. Whether it was taming the daily madness of a complex experiment or moving the whole system through the institute on hovercraft boards, building our own air conditioning or making window-color portraits of ourselves, attending international conferences or winning the TUM dragon boat race, working day and night shifts to acquire paper data or celebrating grill parties, ski days and my soccer world cup betting profit, discussing the odds of physics or fiercely arguing over politics, talking trash during foosball games or chatting about the current progress and the ups and downs of a PhD, improving the apparatus and repairing yet another broken laser or taking the final data after years of preparation, all of these things were only possible with the participation, countless contributions and continuous support of numerous people who created a wonderful atmosphere to work and prosper.

I am deeply grateful to my advisor, Gerhard Rempe. His combination of guidance and freedom to follow my own ideas gave me the perfect environment to grow with novel challenges of a developing PhD. Moreover, his genuine enthusiasm for physics in all its forms was a constant source of inspiration, while his particular and strict way of thinking challenged any loose argumentation and was a huge influence in both, my work and personal development.

Tatjana Wilk was my group leader from day one. Her way of close and critical supervision made her a great sparring partner for new ideas and always pushed me to improve. Her confident and resolute nature greatly eased the troubled times. It was a pleasure to work with her all the way to the last day of my PhD.

I am thankful for the collaboration with many great colleagues in the lab. Without them, operating such a complex experiment would not only have been hopeless but also much less enjoyable. Christian Sames introduced me to the experiment and sparked my passion for FPGAs, Munich blade nights and lunch times by the lake. From Haytham Chibani, I learned to sometimes stop searching in small steps and make a large leap, as well as the sweetness of Moroccan mint tea. In many long nights of fierce pair programming, Maria Bernard-Schwarz contributed insights into performance computing, an awesome experimental control system and her wonderful and weird Austrian accent. I appreciated the many discussions with Paul Altin; I learned a lot

from his physical understanding and shared plenty of hard yakka with him. Nicolas Tolazzi brought Python, Linux, podcasts and (green) tea into my life. We shared a fun, intense and fruitful time inside and outside the lab. Students Anna Caroline Eckl, Ingmari Tietje and Matthias Redies each contributed essential pieces which together formed the backbone for the 3D atom microscopy. In supervising and working with them, I myself learned some very important lessons. Towards the end of my time, Gang Li, Bo Wang and Jonas Neumeier joined the team and while I did not get the chance to really work with them, it is great to see the new influences and ideas at the experiment.

The team of technicians formed by Josef Bayerl, Franz Denk, Florian Furchtsam, Johannes Siegl, Helmuth Stehbeck, Thomas Wiesmeier and Tobias Urban was more than a helping hand but an important ingredient to the success of this work. From moving the experiment as a whole to micrometer-precise mechanics, there is nothing they cannot do.

I want to thank all members of the Max Planck Institute of Quantum Optics, and especially the Quantum Dynamics group, who make up an interesting and resourceful working environment with a great atmosphere.

Finally, I am very grateful to Katharina and my family for their unwavering support and wonderful distraction outside of the lab.

Thank you!